

University of Windsor

Scholarship at UWindor

Electronic Theses and Dissertations

Theses, Dissertations, and Major Papers

3-2-2021

Flow Characteristics of Self-Oscillating Round and Square Jets in a Confined Cavity

Maziar Mosavati
University of Windsor

Follow this and additional works at: <https://scholar.uwindsor.ca/etd>

Recommended Citation

Mosavati, Maziar, "Flow Characteristics of Self-Oscillating Round and Square Jets in a Confined Cavity" (2021). *Electronic Theses and Dissertations*. 8527.
<https://scholar.uwindsor.ca/etd/8527>

This online database contains the full-text of PhD dissertations and Masters' theses of University of Windsor students from 1954 forward. These documents are made available for personal study and research purposes only, in accordance with the Canadian Copyright Act and the Creative Commons license—CC BY-NC-ND (Attribution, Non-Commercial, No Derivative Works). Under this license, works must always be attributed to the copyright holder (original author), cannot be used for any commercial purposes, and may not be altered. Any other use would require the permission of the copyright holder. Students may inquire about withdrawing their dissertation and/or thesis from this database. For additional inquiries, please contact the repository administrator via email (scholarship@uwindsor.ca) or by telephone at 519-253-3000ext. 3208.

Flow Characteristics of Self-Oscillating Round and Square Jets in a Confined Cavity

By

Maziar Mosavati

A Dissertation

Submitted to the Faculty of Graduate Studies
through the Department of Mechanical, Automotive & Materials Engineering
in Partial Fulfillment of the Requirements for
the Degree of Doctor of Philosophy
at the University of Windsor

Windsor, Ontario, Canada

2020

Maziar Mosavati

Flow Characteristics of Self-Oscillating Round and Square Jets in a Confined Cavity

by

Maziar Mosavati

APPROVED BY:

C. Zhang, External Examiner
Western University

T. Bolisetti
Department of Civil & Environmental Engineering

G.W. Rankin
Department of Mechanical, Automotive & Materials Engineering

V.T. Roussinova
Department of Mechanical, Automotive & Materials Engineering

R.M. Barron, Co-Advisor
Department of Mechanical, Automotive & Materials Engineering

R. Balachandar, Co-Advisor
Department of Civil & Environmental Engineering

December 17, 2020

Declaration of Co-Authorship / Previous publication

I. Co-Authorship

I hereby declare that this thesis incorporates the outcome of joint research undertaken in collaboration with my co-supervisors, Dr. Barron and Dr. Balachandar. The collaboration is covered in Chapter 3, 4 and 5 of the thesis. In all cases, the key ideas, primary contributions, numerical simulations, data analysis and interpretation were performed by the author, and the contributions of the co-authors in the associated journal and conference publications were primarily through the provision of guidance and discussions on technical issues and editing of the manuscripts.

I am aware of the University of Windsor Senate Policy on Authorship and I certify that I have properly acknowledged the contributions of other researchers to my thesis and have obtained written permission from each of the co-authors to include the above materials in my thesis.

I certify that, with the above qualification, this thesis, and the research to which it refers, is the product of my own work.

II. Previous publication

This thesis includes original papers that have been published or submitted for publication in peer reviewed journals, as follows:

Thesis chapter	Publication title	Publication status
3	M. Mosavati, R.M. Barron and R. Balachandar, "Characteristics of self-oscillating jets in a confined cavity," Phys. Fluids, 32, 115103-1- 115103-17 (2020).	Published
3	M. Mosavati, R.M. Barron and R. Balachandar, "CFD analysis of the near-field vortex dynamics in a confined square jet", 5 th Thermal and Fluids Engineering Conference (TFEC), April 5 – 8, 2020, New Orleans, LA, USA.	Accepted

4	M. Mosavati, R. Balachandar and R.M. Barron, “Characteristics of self-oscillating twin jets,” Phys. Fluids.	Revision submitted
---	--	-----------------------

I certify that I have obtained a written permission from the copyright owner(s) to include the above published material(s) in my thesis. I certify that the above material describes work completed during my registration as a graduate student at the University of Windsor.

I declare that, to the best of my knowledge, my thesis does not infringe upon anyone’s copyright nor violate any proprietary rights and that any ideas, techniques, quotations, or any other material from the work of other people included in my thesis, published or otherwise, are fully acknowledged in accordance with the standard referencing practices. Furthermore, to the extent that I have included copyrighted material that surpasses the bounds of fair dealing within the meaning of the Canada Copyright Act, I certify that I have obtained a written permission from the copyright owner(s) to include such material(s) in my thesis.

I declare that this is a true copy of my thesis, including any final revisions, as approved by my thesis committee and the Graduate Studies office, and that this thesis has not been submitted for a higher degree to any other University or Institution.

Abstract

Oscillating jets have many practical applications in industry. The self-oscillating behavior of a jet can be observed when the jet emanates into a confined cavity. In this thesis, a step-by-step approach has been followed to investigate important aspects of self-oscillating turbulent jets. The first step focuses on evaluating the characteristics of self-oscillating square and round jets. The jet exits from a submerged round nozzle or a square nozzle with the same hydraulic diameter into a narrow rectangular cross-section cavity at a Reynolds number of 54,000 based on nozzle hydraulic diameter and average jet exit velocity. A numerical investigation of the three-dimensional self-oscillatory fluid structures in the cavity is conducted by solving the unsteady Reynolds-Averaged Navier-Stokes (URANS) equations using a Reynolds stress turbulence model (RSM). Vortex identification using the λ_2 -criterion method is used to investigate the flow dynamics. The simulations show that the vortex rings initially have the nozzle shape near the nozzle exit and, for a square nozzle, axis-switching occurs at about 0.7 hydraulic diameters downstream. Furthermore, after impact on the walls, the vortex rings are converted into two tornado-like vortices. The decay rates of both types of self-oscillating jets initially show the same trend as free round and square jets but change significantly as the effects of oscillation and confinement begin to dominate. The results show that the spread and decay rates of the self-oscillating square jet are higher, while the self-oscillating round jet has higher turbulence intensities near the jet center. Moreover, the Reynolds stress profiles of both round and square self-oscillating jets are qualitatively similar and show two peaks on either side of the centerline, which convert to mild peaks at distances farther downstream.

The second step focuses on the numerical study of self-oscillating twin jets emanating from round and square cross-section nozzles into a narrow rectangular cavity. The flow characteristics are evaluated at nozzle spacing-to-diameter ratios of 2, 3, 4 and 5 at a jet Reynolds number of 27,000. The effects of nozzle spacing on the frequency of oscillation, mean velocity and turbulence features are examined. The results indicate that increasing the spacing does not have much effect on the frequency of oscillations. For a spacing-to-diameter ratio up to four, the two jets merge in the downstream and oscillate as one. At the largest nozzle spacing, the two jets do not merge but oscillate separately across half of the cavity width. Furthermore, as the nozzle spacing is increased, the profiles of Reynolds shear stress demonstrates that the mixing increases in the inner shear layer region.

The last part of the thesis focuses on potential cooling applications of self-oscillating jets. The jet exits from a square cross-section nozzle at a Reynolds number of 54,000. The heated devices are attached externally on the front surface of the cavity. A three-dimensional numerical simulation of the flow is conducted by solving the URANS and energy equations with RSM to assess the thermal features of the flow field. The cooling performance of the self-oscillating jet is compared with the channel flow and the wall jet. The results show that the channel flow has the lowest heat transfer. The heat transfer of wall jets increases around the central region, while the heat transfer of self-oscillating jets is higher farther from the central region. Self-oscillating jets can improve heat transfer over a larger area when the heated elements are in a horizontal arrangement, while the wall jet shows a higher performance for a vertical arrangement of elements.

Dedication

To all my family

Acknowledgments

I would like to express my sincere gratitude to my supervisors Dr. Ron Barron and Dr. Ram Balachandar for their endless support and guidance throughout my Ph.D. studies. I appreciate their encouragement and support which assisted me with my work and gave me self-confidence. I would also like to thank my graduate committee members for their ideas and comments during my research. I am thankful to Dr. Vesselina Roussinova for providing me valuable information. I would like to thank Dr. Gary Rankin and Dr. Tirupati Bolisetti for their valuable time going through my work and for their support along the way, and Dr. Chao Zhang for serving as my external examiner.

I would like to thank all my fellow colleagues throughout my studies in graduate school: Kohei Fukuda, Abishek Sridhar, Subhadip Das and Nimesh Virani have helped me in discussions in subjects of thermo-fluids, numerical modeling and post processing.

I would like to extend my thanks to all faculty and staff members of the Department of Mechanical, Automotive and Materials Engineering and Faculty of Graduate Studies, and not to forget all my friends for their help.

Table of Contents

Declaration of Co-Authorship / Previous publication	iii
Abstract	v
Dedication	vii
Acknowledgments	viii
List of Figures	xi
List of Tables	xiv
Chapter 1. Introduction	1
1.1 Flow characteristics	1
1.2 Objectives and outline of the dissertation	2
References	3
Chapter 2. Brief literature review and numerical modeling	4
2.1 Literature review	4
2.1.1 Round and square free jets	4
2.1.2 Confined jets	6
2.2 Numerical modeling	7
2.2.1 Geometry set up and flow conditions	7
2.2.2 Jet simulation	8
2.2.3 Boundary conditions	12
2.2.4 Visualization methods	12
References	14
Chapter 3. Characteristics of self-oscillating jets in a confined cavity	16
3.1 Summary	16
3.2 Introduction	16
3.3. Methodology	20
3.3.1 Geometry set up	20
3.3.2 Jet simulation	21
3.3.3. Boundary conditions	22
3.3.4 Three-dimensional flow visualization	24
3.4. Validation	24
3.5 Results and discussion	27
3.5.1 Instantaneous near-field vortex deformation	27
3.5.2 Effects of confinement on vortex deformation	30

3.5.3 Oscillation mechanism.....	32
3.5.4 Mean vorticity.....	34
3.5.5 Mean centerline velocity decay and jet width.....	35
3.5.6 Turbulence intensity and Reynolds shear stress	39
3.6 Conclusions.....	42
References.....	44
Chapter 4. Characteristics of self-oscillating twin jets	48
4.1 Summary.....	48
4.2 Introduction.....	48
4.3 Numerical modelling and methodology.....	53
4.4 Results and discussion	57
4.4.1. Oscillation mechanism of single and twin jets	57
4.4.2 Effects of jet spacing on jet frequency.....	62
4.4.3 Mean velocity decay	63
4.4.4. Turbulence characteristics and Reynolds shear stress	67
4.5 Conclusions.....	69
References.....	71
Chapter 5. Use of self-oscillating jets in cooling applications.....	74
5.1 Summary.....	74
5.2 Introduction.....	74
5.3 Geometry and numerical procedure.....	78
5.4 Validation.....	81
5.5 Results.....	83
5.6 Conclusions.....	86
References.....	87
Chapter 6. Conclusions and recommendations.....	90
6.1 Conclusions.....	90
6.2 Recommendations.....	92
Vita Auctoris.....	93

List of Figures

Fig. 1.1 Schematic of different types of jets: (a) free jet, (b) wall jet, (c) offset jet, (d) oscillating jet.....	1
Fig. 2.1 Cavity configuration (not to scale): (a) single round jet, (b) single square jet	8
Fig. 2.2 Cavity configuration (not to scale): (a) twin round jets, (b) twin square jets.....	8
Fig. 2.3 Cross-sections of the mesh generated in a single square jet domain: (a) XZ plane, (b) XY plane.....	9
Fig. 2.4 Cross-sections of the mesh generated in the twin square jets domain: (a) XZ plane, (b) XY plane	9
Fig. 3.1 Cavity configuration: (a) square jet, (b) round jet.....	21
Fig. 3.2 Comparison of fully developed streamwise velocity for a round pipe, with (a) experimental results ³⁴ , (b) law-of-the-wall	23
Fig. 3.3 Comparison of fully developed streamwise velocity for a square duct, with (a) experimental results ³⁵ , (b) law-of-the-wall	23
Fig. 3.4 Time series of cross-flow velocity in a round jet at point (3.2d, 0, -0.9d)	25
Fig. 3.5 Round jet streamwise velocity profile: (a) along centreline, (b) at $X = 1.35d$	25
Fig. 3.6 Perpendicular Reynolds stresses at point (13d, 2.9d, 0): (a) $\rho u'u'$, (b) $\rho v'v'$	26
Fig. 3.7 Mean streamwise velocity on $Z = 0$ for a square jet at (a) $X = 8d$, (b) $X = 18d$	27
Fig. 3.8 Instantaneous vortex deformation of a round jet: (a) front and side views of $\lambda_2 = -1$ isosurface colored by streamwise velocity, (b) vorticity contours on the plane $Y = 0$	28
Fig. 3.9 Instantaneous vortex deformation of a square jet: (a) isosurface of λ_2 colored by streamwise velocity, (b) vorticity contours at plane $Y=0$	29
Fig. 3.10 Vortex interaction of the round jet with confinement wall at selected dimensionless times: (a,d) $t^* = 40$, (b,e) $t^* = 45$, (c,f) $t^* = 50$	31
Fig. 3.11 Vortex interaction of square jet with confinement wall at selected dimensionless times: (a,d) $t^* = 26$, (b,e) $t^* = 32$, (c,f) $t^* = 40$	32
Fig. 3.12 Instantaneous velocity vectors of the oscillating square jet, superimposed on the vorticity contours on the plane $Z = 0$, during a half period ($T/2$)	33

Fig. 3.13 Instantaneous streamtraces of the oscillating square jet, superimposed with static pressure (Pa) contours on the plane $Z = 0$, during a half period ($T/2$).....	34
Fig. 3.14 Mean streamwise vorticity field at the YZ plane: (a, c, e, g) round jet, (b, d, f, h) square jet, (i) zoomed view near the square nozzle exit.....	35
Fig. 3.15 The decay of centerline velocity (Jet types: OS - oscillating square, OR - oscillating round, FS - free square, FR - free round).....	36
Fig. 3.16 Jet thickness of round and square oscillating jets and free square jet	37
Fig. 3.17 Development of mean streamwise velocities profiles: (a) oscillating and free jets, (b) oscillating square jet near the wall.....	38
Fig. 3.18 Development of the profiles of the spanwise mean velocities: (a) oscillating round jet, (b) oscillating square jet.....	38
Fig. 3.19 Streamwise turbulence intensity profiles, u_{rms}/U_e : (a) round jet in XY plane, (b) square jet in XY plane, (c) round jet in XZ plane, (d) square jet in XZ plane	40
Fig. 3.20 Comparison of streamwise centerline turbulence intensities with experimental and other CFD data for free jets	40
Fig. 3.21 Reynolds shear stress on $Z = 0$ plane: (a) round jet, (b) square jet; Reynolds shear stress on $Y = 0$ plane, (c) round jet, (d) square jet.....	42
Fig. 4.1 Schematic of twin free jets configuration (adapted from Laban et al. ¹¹)	49
Fig. 4.2 Cavity configurations (not to scale): (a) twin round jets, (b) twin square jets	53
Fig. 4.3 Cross-sections of the mesh in the twin square jets domain: (a) XZ plane, (b) XY plane	56
Fig. 4.4(a) Time series of streamwise velocity in a square jet at point (14.0d, 0.0, 0.0).....	56
Fig. 4.4(b) Nondimensional streamwise velocity along the symmetry line	56
Fig. 4.5 Non-dimensional streamwise turbulence intensity at $X = 5d$	56
Fig. 4.6 Instantaneous streamwise velocity contours at times t_0 (left column) and $t_0 + T/2$ (half-period; right column): (a,b) single OS jet, (c,d) twin OS jets at $S/d = 2$, (e,f) twin OS jets at $S/d = 5$	60
Fig. 4.7 Instantaneous velocity vectors of the OS twin jet ($S/d = 2$), superimposed on the vorticity contours on the plane $Z = 0$, during a half period ($T/2$)	60
Fig. 4.8 Instantaneous velocity vectors of the OS twin jet ($S/d = 5$), superimposed on the vorticity contours on the plane $Z = 0$, during a period (T); (a – i) correspond to time increments of $T/8$..	62

Fig. 4.9 Streamwise velocity profiles of twin jets at the symmetry line: Mean velocity (a) round twin jets, (b) square twin jets; (c) Instantaneous velocity for round twin jets at $S/d = 4$	65
Fig. 4.10 Mean streamwise velocity of twin oscillating round jets: (a) $S/d = 2$ (b) $S/d = 5$	66
Fig. 4.11 Mean centerline velocity of single and twin oscillating jets: (a) round jets, (b) square jets.....	66
Fig. 4.12 Mean streamwise turbulence intensity of oscillating twin round jets: (a) $S/d = 2$, (b) $S/d = 5$	68
Fig. 4.13 Mean Reynolds shear stress of oscillating twin round jets: (a) $S/d = 2$, (b) $S/d = 5$	69
Fig. 5.1 Schematic of the cavity with hot blocks: (a, d) channel flow, (b, e) self-oscillating jet, (c, f) wall jet. Hot block arrangements: (a, b, c) vertical, (d, e, f) horizontal. (Not to scale)	80
Fig. 5.2 Schematic of four in-line hot blocks (adapted from Xu et al. ²) (Not to scale).....	81
Fig. 5.3 Effect of grid size on the wall temperature distribution ($Re_L = 10^4$).....	82
Fig. 5.4 Wall temperature distributions for four in-line heat sources: (a) water at $Re_L = 10^4$, b) FC-72 at $Re_L = 10^5$	82
Fig. 5.5 Comparison of simulation and experimental heat transfer of the hot blocks	83
Fig. 5.6 Temperature distribution of hot blocks: (a) self-oscillating jet, (b) wall jet, (c) channel flow	84
Fig. 5.7 Temperature field of hot blocks: (a) self-oscillating jet, (b) wall jet, (c) channel flow ..	85
Fig. 5.8 The surface-averaged Nusselt number variation of hot blocks in horizontal arrangement of heaters: (a) self-oscillating jet, (b) wall jet, (c) channel flow	85
Fig. 5.9 Double-averaged Nusselt number of hot blocks: (a) vertical arrangement, (b) horizontal arrangement.....	86

List of Tables

Table 3.1. Jet decay and spread rates of round and square oscillating jets.....	36
Table 4.1 Summary of literature on twin jets	49
Table 4.2. Effect of nozzle spacing on the frequency of oscillating round and square twin jets..	63
Table 5.1. Summary of literature review	75
Table 5.2. Flow parameters of channel flow, wall jet and self-oscillating jet	81

Chapter 1. Introduction

1.1 Flow characteristics

Turbulent jets have many applications in areas such as pumps, heat exchangers, combustion, fuel injection, flow control, drag reduction, mixing, steel casting and cooling systems. Jets can be categorized in several ways, such as free or confined jets. Confined jets can be further categorized according to the type of confinement. A brief overview of different jet types is provided in this section and simple schematics are shown in Fig. 1.1.

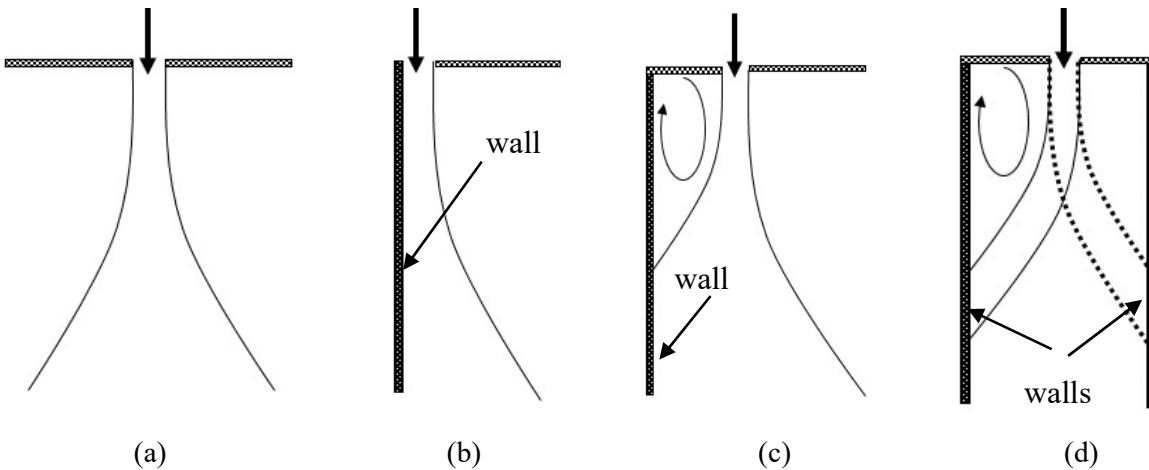


Fig. 1.1 Schematic of different types of jets: (a) free jet, (b) wall jet, (c) offset jet, (d) oscillating jet

In a free jet, the jet flows into a large environment and the jet shear layers grow gradually as illustrated in Fig. 1.1(a). Shear layer growth is due to fluid entrainment and Kelvin-Helmholtz instabilities which creates vortex rings. The mean velocity remains constant up to the end of the free jet core (potential core) and the turbulence intensity is low. At maximum jet penetration, turbulence intensity increases and the jet centreline velocity decays. The jet maintains a fully developed behavior in the downstream¹⁻³. There are some fundamental differences between free round and square jets. One of the most complex flow features of a square jet is axis-switching which is observed near the nozzle exit in non-circular jets. Vortex rings develop and rotate during the axis-switching process. Axis-switching tends to enhance the entrainment which increases shear layer expansion and spread rates¹. Unlike free jets which develop in an infinite environment, confined jets flow into a restricted region in which the wall(s) affect the jet characteristics (see Fig. 1.1(b,c,d)). Compared to the free jet, less fluid is entrained into the confined jet due to the restrictions of the confinement wall(s). Also, there are recirculation regions that occur near the

confinement wall(s)⁴. A wall jet is confined by a wall on one side. The offset jet is a type of confined jet in which the nozzle is located off the wall and the jet emerges into the surrounding fluid in the direction parallel to the wall. The Coanda effect causes the offset jet to deflect towards the wall and attach to it. In the self-oscillating jet, the jet oscillates without any external devices. This type is attractive because it does not have any control port or feedback loop and only relies on the Coanda effect. The mechanism details of self-sustaining oscillating jets are investigated in Chapter 3. One of important applications of self-oscillating jets is in cooling systems for hot devices such as electronic chips. The high temperature of hot devices decreases the devices' performance, and the generated heat must be convected from the hot devices to the environment. For example, PC processors produce a huge amount of heat and heat removal is very important for these electronic devices to extend their life and improve their efficiency.

1.2 Objectives and outline of the dissertation

The present thesis is divided to the following chapters.

Chapter 2 contains a general review of the literature relevant to the problems which are addressed in the thesis. A more detailed discussion of the literature is included in subsequent chapters, which comprises published or submitted journal papers. Chapter 2 also deals with the numerical simulation of oscillating jets. The geometry set up for round and square single and twin self-oscillating jets are explained in detail. Also, jet simulations, boundary conditions and visual methods for identification of vortex structures are explained.

Chapter 3 investigates the characteristics of self-oscillating square and round jets in a confinement cavity. The literature review shows the lack of a comprehensive study of the oscillatory field which can potentially contribute to mixing and entrainment. The motivation of this section is to focus on the physics of the flow and thereby provide a better understanding as to how the oscillatory flow field may be used to control heat transfer and surface temperature uniformity in future studies. To this end, the self-oscillation mechanism of confined jets is studied in detail. Furthermore, the effects of oscillation on the behavior of flow properties such as the mean velocity, turbulent intensities and Reynolds shear stresses are compared with corresponding quantities in free jets.

Chapter 4 investigates twin self-oscillating jets in a confined cavity, where the oscillations are due to the Coanda effect mechanism. This study focuses on the self-oscillatory flow field characteristics of twin oscillating jets, and the effects of nozzle spacing on the frequency and jet

properties. Like the single jet study in Chapter 3, the motivation of this study is to better understand how the flow field may be used to control heat transfer. Understanding of flow characteristics of twin jets provides more information to identify potential regions with higher heat transfer rates. To this end, twin round and square oscillating jets at various nozzle spacing are compared in terms of mean velocity, turbulent intensities and Reynolds shear stresses.

Chapter 5 investigates cooling of hot devices using self-oscillating jets. An array of impingement jets may provide higher heat transfer compared to jets aligned parallel to a hot surface. However, in applications with geometry limitations, impingement jets may not be a viable solution. In this case, since one oscillation of the self-oscillating jet covers a wider area on the hot surface, a single self-oscillating jet may be a practical replacement alternative. In Chapter 5, the cooling performance in terms of temperature and Nusselt number are compared for self-oscillating jets, wall jets and channel flow.

Chapter 6 summarizes the results and provide recommendations for future studies.

References

1. A. Ghasemi, "Near-field vortex dynamics of flows emerging from a rectangular duct," PhD Thesis, University of Waterloo (2019).
2. A.J. Yule, "Large scale structure in the mixing layer of a round jet," *J. Fluid Mech.* 89, 413-432 (1978).
3. M. Shademan, "CFD simulation of impinging jet flows and boiling heat transfer," PhD Thesis, University of Windsor (2015).
4. J. Zhu and T.-H. Shih, "A numerical study of confined turbulent jets," NASA Technical Memorandum, New Orleans, Louisiana, November (1993).

Chapter 2. Brief literature review and numerical modeling

2.1 Literature review

Since this dissertation is organized as a collection of research papers in Chapters 3, 4 and 5, literature that is specifically relevant to those chapters is reviewed therein. Some related literature on free and confined jets is discussed in this chapter.

2.1.1 Round and square free jets

The simple geometry of an axisymmetric round jet has made it very attractive for a wide variety of industrial applications, resulting in a large body of literature on the round jet. Comprehensive jet studies were conducted by Wygnanski and Fiedler¹, List² and Hussein et al.³ Wygnanski and Fiedler¹ used a hot wire to measure mean velocity and turbulence intensity in an axisymmetric turbulent jet. They found that self-similarity of the longitudinal, radial and tangential fluctuations of a round jet occur at 40, 70 and 70 diameters downstream of the nozzle, respectively. They showed that the Taylor's hypothesis is not appropriate, while convection velocity is an appropriate scale for temporal to spatial quantities transformation. Furthermore, using energy balance they demonstrated that the flow becomes self-preserving at almost three times the distance calculated by Sami⁴, which suggests that the flow in Sami's study had not reached the self-preserving state. List² reviewed previous studies to understand the mechanism of jets and plumes, especially interaction with environmental factors such as uniform motion of ambient fluid. Hussein et al.³ found that the mean velocity profiles, turbulence intensities and shear stress at different axial locations collapse to single profiles when they are normalized by appropriate length and velocity scales. They showed that the far-field centerline velocity decay rate does not approach a constant value as observed in the far-field data of Wygnanski and Fiedler¹, but attributed the difference to the experimental facilities and not the method of analysis. Furthermore, to explain the nature of turbulence in jets, such as randomness of turbulence, Hussein et al.³ used large scale structures to analyze the flow. These large scale structures, referred to as coherent structures, play an important role in heat and mass transfer and mixing processes. Dimotakis et al.⁵ used flow visualization to study the dynamic of turbulent jets. They investigated shear layer roll-up which creates vortex ring structures and explained the vortex ring growth. They demonstrated that the jets are dominated by helical or axisymmetric structures in the transition region and the far-field, and that the entrainment and mixing of jets are related to these kinematic structures.

Although based on flow quantitative data from Laser Doppler Anemometry (LDA) and hotwire measurements, the visualization of coherent structures by Hussein et al.³ and others were largely qualitative in nature. Higher resolution is obtained by Particle Image Velocimetry (PIV) images which provide an opportunity for quantitative analysis of jet dynamics. Adrian et al.⁶ discussed the different decomposition methods, such as Reynolds, Galilean and Large-Eddy Simulation (LES), to identify vortical structures and Agrawal and Prasad⁷ used high-pass filtering for vortex structures. Their results showed that for statistical analysis the Reynolds decomposition is better than Galilean and LES and that LES decomposition is the best method for small scale vortices visualization. Shinneeb et al.⁸ investigated the near-exit region of a free jet using proper orthogonal decomposition (POD) and showed the formation of vortices with alternating direction of rotation near the nozzle exit. The results showed that the coherent structures originate in the near-field region of the jet shear layer and control the jet growth rate. Also, they investigated coherent structures in the far-field of a free round jet and showed that the size of vortices and the circulation increases with distance downstream.

Non-circular jets have a lot of advantages such as mixing enhancement, heat and mass transfer improvement. The near-field structures are complicated in three-dimensional developing jets due to the axis-switching process, which is the result of rotation of the vortex ring. Gutmark and Grinstein⁹ studied the axis-switching phenomenon and non-circular jet vortex shedding. Their results illustrated different flow dynamics of the jet for different nozzle shapes, which can be exploited to control the jet flow. They showed that axis-switching is influenced by the inlet flow conditions such as the momentum thickness, turbulence level and Reynolds number. They also demonstrated that, compared to a round jet, a non-circular jet has a larger spread rate due to higher entrainment which increases the mixing process. Quinn and Militzer¹⁰ investigated the near-field of a square jet and observed the off-center peak streamwise velocity due to axis-switching. Furthermore, they showed that the square jet spreads faster compared to the round jet in the near-field with the same inlet conditions. Chua et al.¹¹ investigated the effects on axis-switching of inlet boundary conditions, turbulence intensity and momentum thickness in the diagonal and spanwise directions. They illustrated that a high ratio of momentum thickness along the diagonal to spanwise direction has an adverse effect on the axis-switching process. However, a decrease in turbulence intensity and an increase in the ratio of nozzle hydraulic diameter to spanwise momentum thickness tends to produce axis-switching. Yu et al.¹² investigated starting jets using Planar Laser-

Induced Fluorescence (PLIF) and PIV. They observed the axis-switching and leapfrog processes at all Reynolds numbers and a leading vortex pinch-off at higher Reynolds numbers. During the leapfrog process, the radius of the front rings increases and the rear rings with higher velocity pass the front rings. Ghasemi et al.¹³ studied the flow, turbulence characteristics and vorticity distribution in the developing zone of a square jet using PIV. They demonstrated that the jet decay rate and spread rate of the jet are almost independent of the initial conditions such as nozzle geometry, turbulence intensity levels and momentum thickness at the nozzle. The spread rate of the square jet is about 5% lower than the round jet, and a square jet produces a thicker shear layer compared to the round jet. Sforza et al.¹⁴ studied turbulence properties of nine air jets with different nozzle shapes using PIV. Their results indicate that non-circular jets have a shorter core length than circular jets and a higher entrainment rate in the near-field. In the far-field, the asymptotic decay rate of the centreline velocity is not significantly affected by the different nozzle shapes.

The influence of inlet flow conditions on the flow characteristics of round and square jets has been a topic of considerable interest. Xu et al.¹⁵ studied the effect of different inlet conditions on a turbulent round free jet for a smooth contraction nozzle and for a long pipe nozzle. They showed that velocity decay rates of pipe jets in the far-field are smaller than for contraction jets and that pipe jets develop into a self-preservation state more rapidly than contraction jets. Also, the results showed that the distance between the ring vortices in the contraction jet is larger than for the pipe jet in the near-field. In the near-field, the pipe jet has a thicker shear layer and higher turbulence intensity compared to the contraction jet. Mi et al.¹⁶ also studied the effect of inlet flow conditions on a turbulent free jet issuing from smooth contraction and long pipe nozzles. They observed that the velocity decay rate and spread rate at the centerline of the smooth contraction nozzle in both the near-field and far-field is larger than for the long pipe nozzle. Also, the asymptotic spreading rate of the contraction nozzle is larger than that of the pipe jet. Ferdman et al.¹⁷ experimentally studied the effects of inlet conditions on the round jet for a smooth contraction nozzle, a pipe nozzle and uniform flow. Uniform flow produced larger initial growth rate of turbulent intensity and velocity decay rate of the far-field.

2.1.2 Confined jets

Hussein et al.³ studied the reduction of entrainment due to confinement. They used flying and stationary hot-wire anemometer methods and LDA to study confined jet flow at a distance of 50 –

122 diameters downstream of the nozzle. They showed that the increase in confinement ratio hinders the turbulent flow by increasing the turbulence dissipation, decreasing the turbulence kinetic energy due to lower values of the eddy diffusivity, and causing a reduction in the entrainment of the surrounding fluid compared to a free jet. They proposed a model to determine the dimensions at which the confined jet acts like a free jet.

Chua and Lua¹⁸ studied characteristics of a confined air jet from a circular nozzle and a rectangular nozzle with an aspect ratio of 6. They showed that the decay rate of the confined jet is almost three times less than that of free square and circular jets. Also, the spread rate of the confined jet is quite similar to that of the plane free jet but higher than the circular and square free jets. Kandakure et al.¹⁹ studied the effects of confinement of a jet on hydrodynamic characteristics such as entrainment rate, turbulent kinetic energy, turbulent viscosity, pressure profile, jet spread rate, the effect of enclosure diameter and effect of the presence of the draft tube. They showed that a decrease in the enclosure size causes an increase in the turbulent dissipation and reductions in turbulent viscosity values, entrainment rates and jet spread angle. Their study indicated that the jet decays faster when the size of the surrounding enclosure is smaller and, for a smaller draft tube, lower entrainment rates occur.

2.2 Numerical modeling

In this study, a finite volume formulation is used to solve the unsteady incompressible Navier-Stokes equations. Unsteady Reynolds-Averaged Navier-Stokes (URANS) simulations have been carried out to predict the turbulent flow of self-oscillating jets issuing from round and square nozzles. In this section, the turbulence model and the visualization method used to analyze the flow are discussed in detail. The STAR-CCM+ software is used to conduct the computational fluid dynamics simulations.

2.2.1 Geometry set up and flow conditions

This thesis investigates the flow characteristics of single and twin water jets issuing from submerged round and square nozzles into a rectangular confinement cavity with dimensions of 250 mm x 585 mm x 40 mm, as illustrated in Figs. 2.1 and 2.2. The submerged entry nozzle hydraulic diameter (d) and length are 14 mm and 95 mm, respectively, and the nozzles have a wall thickness of 3 mm. The fluid is assumed to be incompressible with constant properties at ambient temperature and the Reynolds number of the single and twin oscillating jets are 54000 and 27000,

respectively. The dimensions of the cavity conform to the requirements for stable oscillations²⁰: that the nozzle diameter to cavity width ratio must be in the range of 0.05-0.3 and the cavity thickness to width ratio must be in the range of 0.1-0.5.

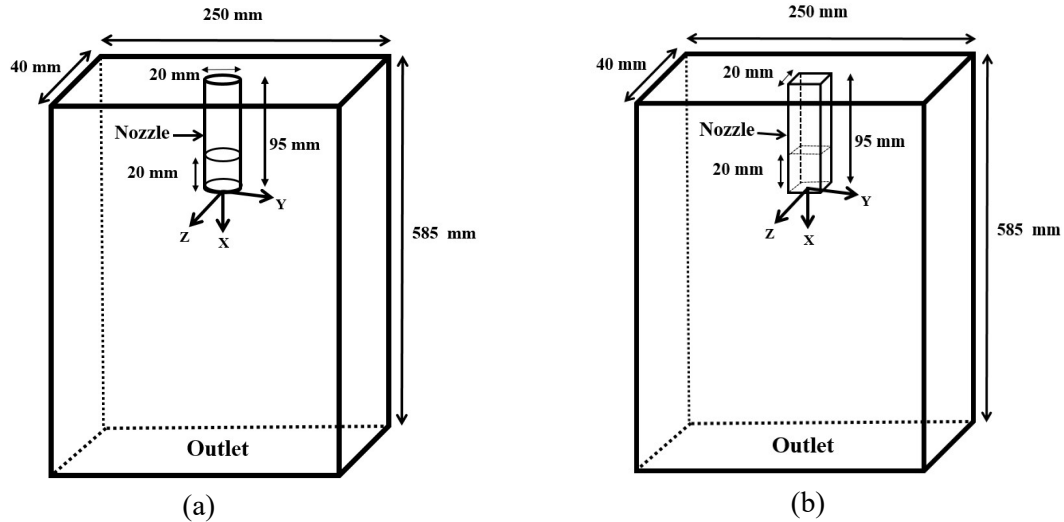


Fig. 2.1 Cavity configuration (not to scale): (a) single round jet, (b) single square jet

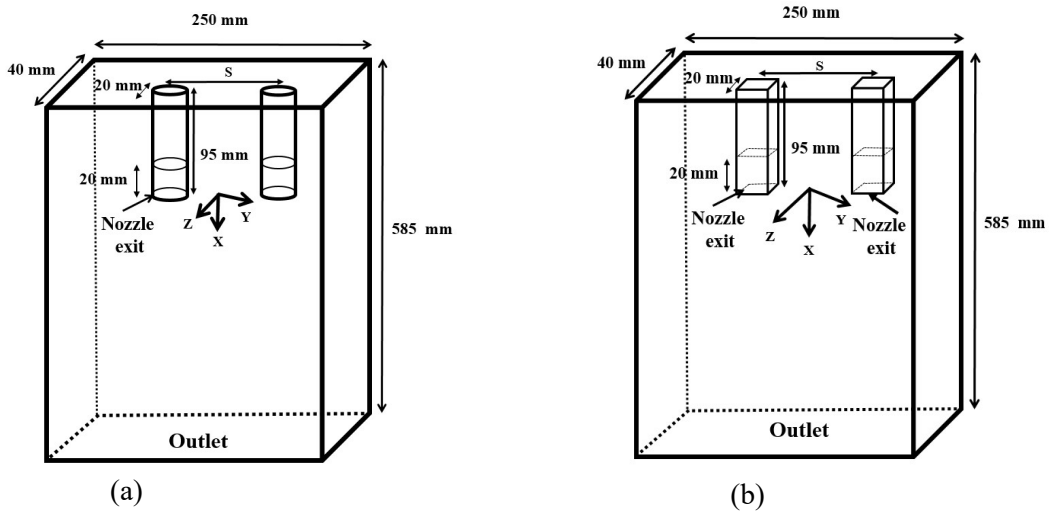


Fig. 2.2 Cavity configuration (not to scale): (a) twin round jets, (b) twin square jets

2.2.2 Jet simulation

The computational domain (i.e., confinement cavity) is discretized using a hexahedral mesh with 6 million cells, as illustrated in Figs. 2.3 and 2.4. This cell size was determined to be adequate after performing simulations on several mesh sizes. For this mesh, the dimensionless distance of the first cell from the walls ($Y^+ = Yu_\tau/\nu$) is less than one, where ν is kinematic viscosity and u_τ is

friction velocity defined as $u_\tau = (\tau_w/\rho)^{0.5}$, where τ_w is wall shear stress. Details regarding mesh independence are presented in Chapter 3. Figures 2.3 and 2.4 show the mesh generated for the single and twin jets simulations, respectively.

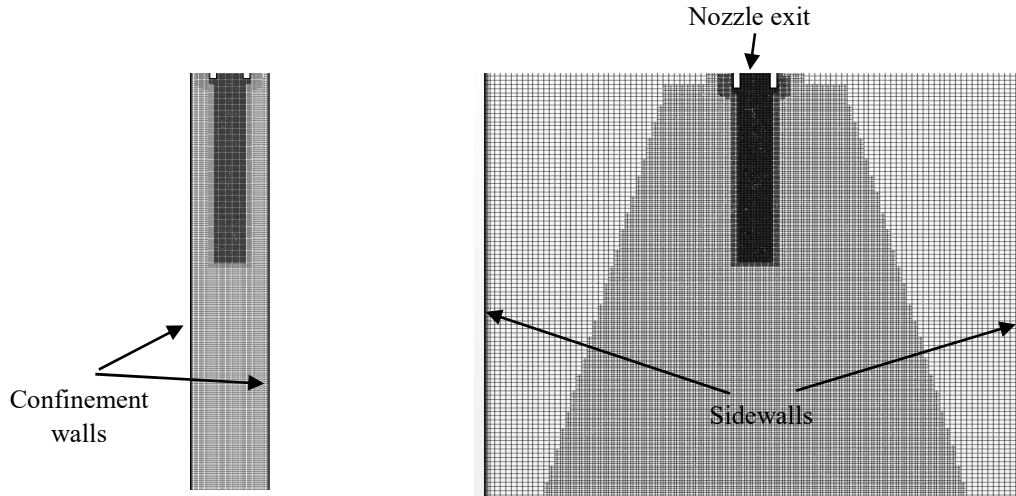


Fig. 2.3 Cross-sections of the mesh generated in a single square jet domain: (a) XZ plane, (b) XY plane

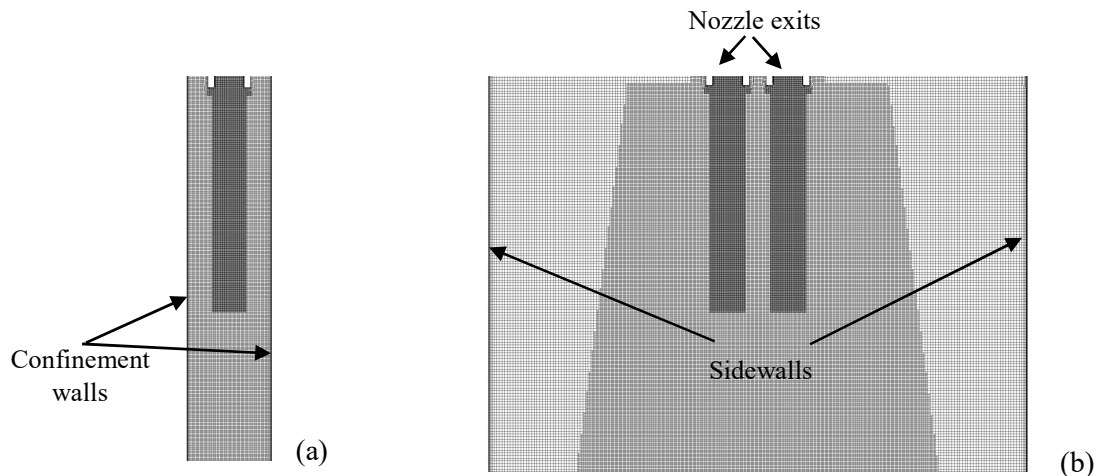


Fig. 2.4 Cross-sections of the mesh generated in the twin square jets domain: (a) XZ plane, (b) XY plane

The governing Navier-Stokes equations are discretized by the finite volume method and solved using the commercial software STAR-CCM+ with a second-order upwind scheme for convection terms and second-order time implicit scheme for time discretization. The time step is set at 0.01 ms which ensures that the Courant number is less than one. The results are shown to be time step independent in Chapter 3. The SIMPLE algorithm is used for pressure-velocity coupling. The

Reynolds-Averaged Navier-Stokes equations in tensorial notation for unsteady incompressible flow are²¹

$$\frac{\partial U_j}{\partial X_j} = 0 \quad (1)$$

$$\rho \left(\frac{\partial U_i}{\partial t} + U_j \frac{\partial U_i}{\partial X_j} \right) = -\frac{\partial P}{\partial X_i} + \frac{\partial}{\partial X_j} \left[\mu \frac{\partial U_i}{\partial X_j} - \overline{\rho u'_i u'_j} \right] \quad (2)$$

where U_i and u'_i are the mean and fluctuating velocity components, respectively, P is the pressure, ρ is the density, μ is the dynamic viscosity and the overbar denotes time-averaged values. Using the Boussinesq assumption, the components of the Reynolds stress tensor are given by²¹

$$\overline{\rho u'_i u'_j} = \frac{2}{3} \rho k \delta_{ij} - \mu_t \left(\frac{\partial U_i}{\partial X_j} + \frac{\partial U_j}{\partial X_i} \right) \quad (3)$$

where k is the turbulent kinetic energy, μ_t is referred to as turbulent viscosity and δ_{ij} is the Kronecker delta. In this study, the unsteady Elliptic Blending Reynolds Stress Model (EBRSM)²¹, which consists of transport equations for each of the stress tensor components, is used to model turbulence.

The Reynolds stress equations are

$$\left(\frac{\partial \overline{u'_i u'_j}}{\partial t} + U_k \frac{\partial \overline{u'_i u'_j}}{\partial X_k} \right) = P_{ij} - \epsilon_{ij} + \pi_{ij} - \left(\frac{\partial \overline{u'_i u'_j u'_k}}{\partial X_k} \right) + \frac{\mu}{\rho} \left(\frac{\partial^2 \overline{u'_i u'_j}}{\partial X_k^2} \right)$$

where P_{ij} , ϵ_{ij} and π_{ij} are the production, dissipation and velocity–pressure gradient tensors, respectively.

The production tensor

$$P_{ij} = -\left(\overline{u'_k u'_i} \frac{\partial U_j}{\partial X_k} + \overline{u'_k u'_j} \frac{\partial U_i}{\partial X_k} \right) \quad (5)$$

accounts for the kinetic energy transfer of the mean flow to the fluctuating velocity field. The production sustains the turbulence of the flow through the energy transfer of large scale mean motions to the small scale fluctuating motions²².

Energy is transferred from larger to smaller eddies. In the smallest eddies, turbulent energy can be converted to internal energy due to viscous dissipation. In other words, the smallest eddies convert

kinetic energy to thermal energy at the molecular level. The mean rate of work which is done by the fluctuating strain rate against fluctuating viscous stresses is given by the dissipation tensor²³

$$\epsilon_{ij} = 2 \frac{\mu}{\rho} \left(\overline{\frac{\partial u'_i}{\partial X_k} \frac{\partial u'_j}{\partial X_k}} \right) \quad (6)$$

The pressure-strain correlation

$$\pi_{ij} = -\frac{1}{\rho} u'_j \frac{\partial P'}{\partial X_i} + u'_i \frac{\partial P'}{\partial X_j} \quad (7)$$

redistributes energy among the Reynolds stresses components.

The dissipation rate of ϵ can be computed from

$$\frac{\partial}{\partial x_i} (\rho \epsilon u_i) = \frac{\partial}{\partial x_j} \left[\left(\mu + \frac{\mu_t}{\sigma_\epsilon} \right) \frac{\partial \epsilon}{\partial x_j} \right] C_{\epsilon 1} \frac{1}{2} P_{ii} \frac{\epsilon}{k} - C_{\epsilon 2} \rho \frac{\epsilon^2}{k} \quad (8)$$

where $\sigma_\epsilon = 1$, $C_{\epsilon 1} = 1.44$ and $C_{\epsilon 2} = 1.92$. The turbulent kinetic energy is computed from the Reynolds stress tensor

$$k = \frac{1}{2} \overline{u'_i u'_i} \quad (9)$$

The turbulent viscosity is defined by

$$\mu_t = \rho C_\mu \frac{k^2}{\epsilon} \quad (10)$$

where $C_\mu = 0.09$.

The production, dissipation and velocity pressure-gradient balance each other. The terms $\left(\overline{\frac{\partial u'_i u'_j u'_k}{\partial X_k}} \right)$ and $\left(\overline{\frac{\partial^2 u'_i u'_j}{\partial X_k^2}} \right)$ are the turbulent transport and viscous diffusion tensors. The diffusion of turbulent energy is responsible for diffusing the mean flow momentum.

The energy conservation equation is expressed as

$$\rho \left(\frac{\partial T}{\partial t} + U_i \frac{\partial T}{\partial X_i} \right) = \frac{\partial}{\partial X_i} \left[\frac{\mu}{Pr} \frac{\partial T}{\partial X_i} - \overline{\rho u'_i \theta} \right] \quad (11)$$

where T is the temperature, θ is the temperature fluctuation and Pr is the Prandtl number. Based on the Boussinesq assumption, the temperature fluctuation is defined as

$$\overline{\rho u'_i \theta} = \sigma_t \frac{\partial T}{\partial X_i} \quad (12)$$

where σ_t is a turbulent Prandtl number, defined by

$$\sigma_t = \frac{\mu_t}{\alpha_t} \quad (13)$$

where the α_t is turbulent thermal diffusivity.

2.2.3 Boundary conditions

Steady RANS RSM with a uniform inlet flow and a pressure outlet condition at the exit is applied in STAR-CCM⁺ to provide fully developed flow in the duct. The round and square ducts exit conditions are mapped as an inlet condition for the simulation in the confinement cavity. The inlet boundary conditions are applied inside the nozzle to ensure an accurate representation of the flow at the exit plane. All walls of the confinement cavity are treated as no-slip boundaries and an outflow condition is applied at the outlet of the computational domain.

2.2.4 Visualization methods

Different vortex identification methods such as vorticity threshold, pressure threshold and velocity gradient-based methods such as Q-criterion, Δ -criteria and λ_2 -criterion have been developed to identify vortex structures in a flow field. Each method comes with its own strengths and weaknesses, which are highlighted below. The method of choice for the current research is the λ_2 -criterion for reasons that will become apparent.

The simplicity of the vorticity threshold method, which identifies vortex structures as regions where the vorticity is larger than a prescribed threshold value, makes it attractive. However, the threshold value is arbitrary, and this method cannot distinguish between vortical regions with swirling flow which is a vortex, and shear layer vorticity which is not a vortex. Furthermore, the maximum vorticity does not always occur at the center of the vortex area²⁴. In the pressure threshold method, the vortex is defined where the static pressure is lower than a prescribed pressure threshold. Although this method is useful for vortex identification in turbulent boundary layer flow, the threshold level is arbitrary and the pressure decays with a lower rate than vorticity²⁵. Also, all vortices do not show a low-pressure core, as in the case of an anticyclone weather system which has high pressure at the core²⁴.

The Q-criterion method identifies regions where the second invariant of the velocity gradient tensor, Q , is positive. This second invariant is a measure of the excess rate of rotation tensor over the strain tensor. If the threshold of Q is set too low, large regions can be identified as vortices although they are not physically significant²⁶. The Δ -criterion method determines a vortex as a region where the velocity gradient tensor has complex eigenvalues. This criterion considers the complex eigenvalues to show the region where the streamlines are closed or form a spiral pattern^{24,27}.

The λ_2 -criterion is especially attractive since it is derived from the requirement that the pressure minimum occurs at the vortex core. Jeong and Hussain²⁸ observed that there is not a consistent relation between minimum pressure and vortex core due to two effects. First, unsteady straining creates a vortical structure without any observed pressure minimum and second, viscous effects eliminate minimum pressure in the vortical flow. In the λ_2 -criterion method, the effects of unsteadiness and viscosity are ignored. To formulate the problem in terms of a rate of strain tensor, the first step is to take the gradient of the incompressible Navier-Stokes equations. The second step is to decompose the resulting equation into symmetric and antisymmetric parts. The last step is to subtract off the vorticity transport equation, yielding the equation

$$\frac{D\mathbf{S}}{Dt} - \frac{\mu}{\rho} \nabla^2 \mathbf{S} + \mathbf{S}^2 + \mathbf{\Omega}^2 = -\frac{1}{\rho} \nabla(\nabla P) \quad (14)$$

where \mathbf{S} is the shear strain rate tensor, $\mathbf{\Omega}$ is the rotation rate tensor. The first and second terms represent the rate of irrotational straining and viscous effects, respectively. Ignoring unsteady and viscous effects reduces the Navier-Stokes equations to

$$\mathbf{S}^2 + \mathbf{\Omega}^2 \approx -\frac{1}{\rho} \nabla(\nabla P) \quad (15)$$

Jeong and Hussain²⁷ showed that the pressure Hessian matrix $\nabla(\nabla P)$ is symmetric, the eigenvalues are real and the eigenvectors are orthogonal. When the pressure matrix has two positive eigenvalues a minimum local pressure is observed. These two positive eigenvalues of $\nabla(\nabla P)$ correspond to two negative eigenvalues of $\mathbf{S}^2 + \mathbf{\Omega}^2$. Therefore, $\mathbf{S}^2 + \mathbf{\Omega}^2$ has three real eigenvalues $\lambda_1 \geq \lambda_2 \geq \lambda_3$ where λ_2 has a negative value which is used to identify minimum pressure at the vortex core²⁸. Since the λ_2 -criterion considers pressure minima which is created due to the vertical motion, it is a good method to identify a vortex core. Therefore, the λ_2 -criterion was chosen for the visualization of three-dimensional structures in this work.

References

1. I. Wygnanski and H. Fiedler, "Some measurements in the self-preserving jet," *J. Fluid Mech.* 3, 577-612 (1969).
2. E.J. List, "Turbulent jets and plumes," *Ann. Rev. Fluid Mech.* 14, 189-212 (1982).
3. H.J. Hussein, S.P. Capp and W.K. George, "Velocity measurements in a high-Reynolds-number, momentum-conserving, axisymmetric, turbulent jet," *J. Fluid Mech.* 258, 31-75 (1994).
4. S. Sami, "Balance of turbulence energy in the region of jet-flow establishment," *J. Fluid Mech.* 29, 81-92 (1967).
5. P.E. Dimotakis, R.C. Miake-Lye and D.A. Papantoniou, "Structure and dynamics of round turbulent jets," *Phys. Fluids* 26, 3185-3192 (1983).
6. R.J. Adrian, K.T. Christensen and Z.C. Liu, "Analysis and interpretation of instantaneous turbulent velocity fields," *Exp. Fluids* 29, 275-290 (2000).
7. A. Agrawal and A.K. Prasad, "Properties of vortices in the self-similar turbulent jet," *Exp. Fluids* 33, 565-577 (2002).
8. A.-M. Shinneeb, J.D. Bugg and R. Balachandar, "Quantitative investigation of vortical structures in the near-exit region of an axisymmetric turbulent jet," *J. Turbul.* 9, 1-20 (2008).
9. E.J. Gutmark and F.F. Grinstein, "Flow control with noncircular jets," *Annu. Rev. Fluid Mech.* 31, 239-272 (1999).
10. W.R. Quinn and J. Militzer, "Experimental and numerical study of a turbulent free square jet," *Phys. Fluids* 31, 1017-1025 (1988).
11. L.P. Chua, Y.F. Li, S.C.M. Yu and T. Zhou, "Axis-switching of a square jet," 14th Australasian Fluid Mechanics Conference, Adelaide University, Adelaide, Australia (2001).
12. S.C.M. Yu, J.J. Ai, L. Gao and A.W.K. Law, "Vortex formation process of a starting square jet," *AIAA J.*, 46, 223-231 (2008).
13. A. Ghasemi, V. Roussinova and R. Balachandar, "A study in the developing region of the square jet," *J. Turbul.* 14, 1-24 (2013).
14. F. Sforza, J. Mi and G.J. Nathan, "Statistical properties of turbulent free jets issuing from nine differently-shaped nozzles," *J. Flow Turbul. Combust.* 84, 583-606 (2010).

15. G. Xu and R.A. Antonia, "Effect of different initial conditions on a turbulent round free jet," *Exp. Fluids* 33, 677–683 (2002).
16. J. Mi, D.S. Nobsy and G.J. Nathan, "Influence of jet exit conditions on the passive scalar field of an axisymmetric free jet," *J. Fluid Mech.* 432, 91-125 (2001).
17. E. Ferdman, M. Otugen and S. Kim, "Effect of initial velocity profile on the development of round jets," *J. Propul. Power* 16, 676-686 (2000).
18. L.P. Chua and A.C. Lua, "Measurements of a confined jet," *Phys. Fluids*, 10, 31-37 (1998).
19. M.T. Kandakure, V.C. Patkar and A.W. Patwardhan, "Characteristics of turbulent confined jets," *J. Chem. Eng. Proc.* 47, 1234–1245 (2008).
20. N.J. Lawson, M.P. Arrudab and M.R. Davidson, "Control of a submerged jet in a thin rectangular cavity," *J. Fluids Struct.* 20, 1025–1042 (2005).
21. K. Hoffmann and S.T. Chiang, *Computational Fluid Dynamics*, Vol. 3, 4th Edition, Engineering Education System, Wichita, Kansas, USA (2000).
22. M. Gibson and B.E. Launder, "Ground effects on pressure fluctuations in the atmospheric boundary layer," *J. Fluid Mech.* 86, 491–511 (1978).
23. I.B. Celik, "Introductory Turbulence Modeling," Lecture Notes, West Virginia University, Morgantown, West Virginia (1999).
24. B.P. Epsy, "Review of vortex identification methods," 55th AIAA Aerospace Sciences Meeting, Grapevine, Texas (2017).
25. S.K. Robinson, "Coherent motions in the turbulent boundary layer," *Annu. Rev. Fluid Mech.* 23, 601- 639 (1991).
26. J.C.R. Hunt, A.A. Wray and P. Moin, "Eddies, streams, and convergence zones in turbulent flows," *Proceedings of the Summer Program, Stanford University, CA*, 193-208 (1988).
27. M.S. Chong, A.E. Perry and B.J. Cantwell, "A general classification of three-dimensional flow fields," *Phys. Fluids A: Fluid Dyn.* 2, 765-777 (1990).
28. J. Jeong and F. Hussain, "On the identification of a vortex," *J. Fluid Mech.* 285, 69-94 (1995)

Chapter 3. Characteristics of self-oscillating jets in a confined cavity

3.1 Summary

Jets emanating into a confined cavity exhibit self-oscillating behavior. This study is focused on evaluating characteristics of oscillating square and round jets. The jet exits from a submerged square or round nozzle of the same hydraulic diameter into a thin rectangular cavity at Reynolds number of 54,000 based on nozzle hydraulic diameter and average jet exit velocity. An investigation of the three-dimensional self-oscillatory flow structures is conducted using the unsteady Reynolds-Averaged Navier-Stokes equations with the Reynolds stress turbulence model. Vortex identification using the λ_2 -criterion is used to investigate the flow dynamics. For the oscillating square jet, vortex rings initially have a square shape near the nozzle exit, before axis-switching and transforming into a circular ring. Upon impact on the walls, two tornado-like vortices are produced. The decay rate of oscillating square and round jets initially show a trend traditionally noted in the corresponding free jets but changes significantly with distance from the nozzle as the effects of oscillation and confinement begin to dominate. Reynolds stress profiles for both types of jets are qualitatively similar and show two peaks on either side of the centerline, which convert to mild peaks farther downstream. Spread and decay rates of oscillating square jets are higher, while oscillating round jets have higher turbulence intensities near the jet center. Compared to free jets, more uniform Reynolds stresses at farther distances from the jet centerline in oscillating jets will enhance heat transfer over a larger area, making oscillating jets suitable in many cooling applications.

Key Words: Oscillating jets, confined cavity, computational fluid dynamics

3.2 Introduction

Oscillating jets are used in many applications including mixing enhancement, flow control, and cooling systems. Thermal management is an important consideration in the cooling of electronic chips and can affect the cooling system's cost, design and performance. The use of multiple jets impinging underneath the heated surfaces has been recommended. However, geometry limitations can prevent the use of jet arrays. Oscillating jets can potentially provide an alternate means of enhancing cooling efficiency. The presence of the Coanda effect causes the jet to deflect to the walls and the pressure gradient between the concave and convex side of the jet leads to oscillation.

Furthermore, non-circular free jets have attracted considerable attention due to the axis-switching process, which plays an important role in increasing jet entrainment and mixing properties. Since cooling jets are confined by walls in many applications¹, there is a need to study the characteristics of both circular and non-circular cross-section jets in the presence of confinement walls.

Extensive numerical and experimental studies have been carried out to observe the near-field and far-field characteristics of a round jet. These include the effects of Reynolds number on the coherent structures², and the effects of confinement on the flow field³. Although many studies have been conducted to evaluate the near-field dynamics of round jets, there are only a few studies on the near-field of square jets. Entrainment enhancement in square jets is mainly due to higher self-induced velocity at the corners of the vortex rings which rotate by 45° compared to the initial orientation. This phenomenon is known as the axis-switching process. Quinn and Militzer⁴ and Quinn⁵ studied the near-field of a square free jet. In their experiments, hot-wire measurements indicated an off-center peak of streamwise velocity near the jet exit due to axis-switching. Their near-field numerical results did not match well with their experiments, possibly because of their coarse grid and the use of the $k-\epsilon$ turbulence model. Grinstein and Devore⁶ carried out visualization of the near-field of a square jet. They investigated the effects of the initial conditions such as momentum thickness, turbulence level and Reynolds numbers on vortex deformation and axis-switching. Grinstein⁷ studied rectangular vortex ring deformation for nozzle with aspect ratios of $1 \sim 4$ at high Reynolds number ($> 120,000$). They demonstrated that only one axis-switching occurs at aspect ratios less than 3. However, the vortex ring bifurcates at the aspect ratio of 4. The two bifurcated rings reconnect farther downstream and create a larger deformed vortex, resulting in a second axis-switching. Chua et al.⁸ investigated the effects of initial boundary conditions, turbulence intensity, and momentum thickness in the diagonal and spanwise directions on axis-switching. They demonstrated that a high ratio of momentum thickness along the diagonal to spanwise direction has an adverse effect on the axis-switching process. However, a decrease in turbulence intensity and an increase in the ratio of nozzle hydraulic diameter to spanwise momentum thickness tends to produce axis-switching. Yu et al.⁹ investigated starting jets at Reynolds numbers in the range of 2,000-5,000 using Planar Laser-Induced Fluorescence (PLIF) and Particle Image Velocimetry (PIV). They observed axis-switching and leapfrog processes at all Reynolds numbers, and a leading vortex pinch-off at higher Reynolds numbers. During the leapfrog process the radius of the front rings increase and the rear rings with higher velocity move

ahead of the front rings. Sankar et al.¹⁰ investigated the effects of confinement and axis-switching of a square jet at a Reynolds number of 40,000. The jet was confined by a cavity with a solid bottom wall and a free surface at the top. They used quadrant decomposition to analyse the flow field which indicated different turbulent characteristics in the bottom and top regions. They demonstrated that after a distance of 15 nozzle diameters, the flow loses free jet characteristics due to the interaction with the boundaries and Reynolds stresses indicate higher mixing properties in the bottom region of the cavity rather than the top. Chen and Yu¹¹ studied rectangular jets with aspect ratios ranging from 1 to 3 and reported a correlation between the secondary flow and downstream velocity during the axis-switching. They showed that the location of axis-switching is not dependent on aspect ratio, while it is related to corner effects due to the entrainment process. Ghasemi et al.¹² studied the developing region of free round and square jets using PIV at Reynolds number of 50,000. They showed a faster break-up of the shear layer resulting in a decreased length of the potential core for the square jet. Besides observing the double peak in streamwise velocity profiles, they also observed the formation of the secondary vorticity at the edge of the square nozzle and close to the centerline. In another study dealing with square jet vortex dynamics at Reynolds numbers of 8,000 and 45,000, Ghasemi et al.¹³ used Large-Eddy Simulations (LES) to evaluate the axis-switching process and the influence of the pressure field on vortex ring deformation.

Oscillating jets are created when the flow field is confined and the vortex rings interact with the walls. The characteristics of this interaction is important in the flow evolution. Several studies¹⁴⁻¹⁵ have been conducted on a confined vortex ring with circular and elliptical cores that interact with the wall. Lim et al.¹⁶ presented the interaction of a laminar vortex ring with an inclined wall that created helical vortex lines. They reported a rebound process, which is essentially a vortex core distortion due to wall confinement. Walker et al.¹⁷ also performed a study of the interaction of a laminar vortex ring with confinement walls. They observed the generation of secondary and tertiary vortex formation near the walls. Chang et al.¹⁸ investigated the effects of confinement walls on elliptical vortex rings. They demonstrated vortex deformation and fluid entrainment when the vortex ring approaches the walls, creating two tornado-like vortices. Sooraj and Sameen¹⁹ studied the decay of circular vortex rings in a square confined enclosure. They showed the effects of the confinement ratio, which is defined as the ratio of vortex ring diameter to the confinement width

of the enclosure, on vortex ring deformation. They observed that the effects of non-axisymmetric confinements are present at $Re = 1,300$, while it is not visible at a lower $Re = 300$.

The main mechanism influencing the oscillation of a jet is the Coanda effect. A comprehensive study on shear layer instabilities and the nature of oscillation in a shallow cavity by Coanda effect has been reported by Rockwell and Naudascher²⁰ and Rockwell²¹. Gebert et al.²² conducted a two-dimensional numerical simulation for a submerged entry circular nozzle into a rectangular cavity. They demonstrated that the oscillation can be changed or stopped by manipulating the cross-flow. Lawson²³ investigated a submerged round jet in a rectangular cavity using PIV and Laser Doppler Velocimetry (LDV). They showed that the frequency of oscillations is independent of cavity thickness, while the frequency decreases by increasing the cavity width.

The oscillation frequency can be controlled by the Reynolds number, cavity width-to-nozzle diameter ratio, Lorentz forces and the use of side jets. Righolt et al.²⁴ studied a self-oscillating confined square jet in a rectangular cavity using the LES turbulence model. They showed that the oscillation disappears when the Reynolds number is below a critical value ($Re_{critical} = 1,600$) and for aspect ratios larger than a critical value ($(width/diameter)_{critical} = 50$). They noticed stable and unstable oscillation modes at different Reynolds numbers and aspect ratios. Kalter et al.^{25,26} experimentally investigated the effects of Lorentz forces on the self-oscillation of a submerged square jet. They introduced a critical Stuart number (N_c) and showed that jet oscillation is independent of Reynolds number for $N < N_c$. Lawson et al.²⁷ investigated using one lateral injection jet below and one above the primary submerged round jet and perpendicular to the main jet. They showed that a maximum thrust vectoring performance occurs when the side jet is located above the main jet (at 12% cavity width). Also, the mass ratio of the side jet to the main jet should be less than 25%. Bensider et al.²⁸ numerically studied a self-oscillating submerged round jet in a rectangular cavity with two side injections above the main jet. The authors revealed that the main jet has a minimum frequency and maximum deflection when the mass ratio of side jet to main jet is less than 0.25. Mataoui et al.²⁹ studied the interaction of the turbulent round jet with a cavity with two lateral walls and a bottom wall. They showed different flow regimes, steady, stable oscillation, and unstable oscillation for different nozzle exit locations in the cavity. They demonstrated the absence of oscillation and stable oscillation when the nozzle is close to the walls, and far from the walls in the core flow, respectively. In another study, Mataoui et al.³⁰ observed a

linear behavior of frequency with Reynolds number and a decrease in frequency when the impingement distance increases in a periodic jet oscillation.

The objective of the current study is to investigate the characteristics of oscillating jets. The literature review shows the lack of a comprehensive study of the oscillatory flow field which can potentially contribute to mixing and entrainment. The focus of this study is on the physics of the flow, thereby providing a better understanding of how oscillatory flow may be used to control heat transfer and surface temperature uniformity in applications. To this end, the self-oscillation mechanism of round and square jets is explored. The effects of oscillation on the behavior of flow properties such as the mean velocity, turbulent intensities and Reynolds shear stresses are compared with corresponding quantities in free jets. A better understanding of the characteristics of oscillating jets will help identify regions with potentially higher heat transfer rates and greater surface temperature uniformity due to higher jet spread.

3.3. Methodology

3.3.1 Geometry set up

The rectangular confinement cavity illustrated in Fig. 3.1 has dimensions of 250 mm x 585 mm x 40 mm. The jet exits from the submerged nozzle into the cavity. The submerged entry nozzle has a round or square shape with a hydraulic diameter $d = 14$ mm and length of 95 mm. The nozzle wall thickness is 3 mm and the fluid (water) is assumed to be incompressible with a density (ρ) of 997 kg/m³ and dynamic viscosity (μ) of 9.7×10^{-4} kg/(m.s). All solid walls are assumed to be smooth. The cavity configuration adopted in this work is the same as Lawson et al.²⁷ to enable a direct comparison for the purpose of validation.

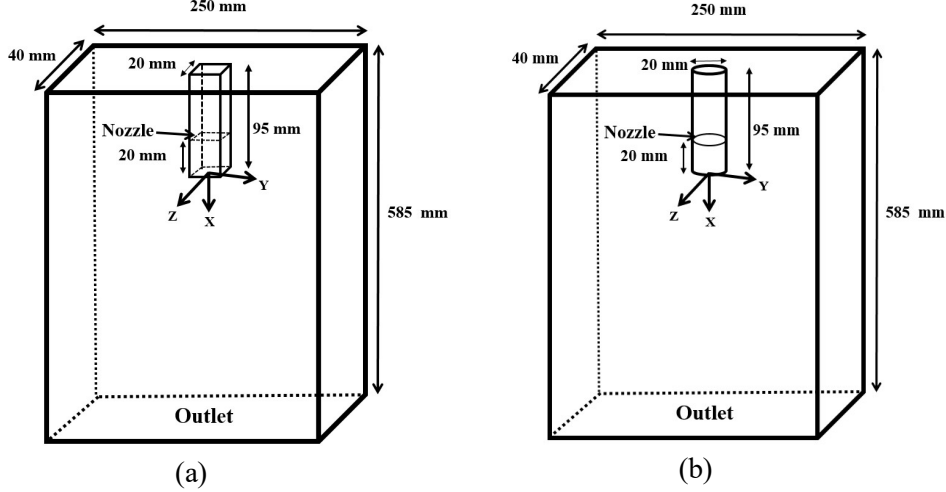


Fig. 3.1 Cavity configuration: (a) square jet, (b) round jet

3.3.2 Jet simulation

The computational domain (i.e. confinement cavity) is discretized using a multiblock structured hexahedral mesh with 6 million cells. This cell size was determined to be adequate after performing the simulations on several mesh sizes, as shown in Section 3 below. For the 6 million cell mesh, the dimensionless distance of the first cell from the walls ($Y^+ = Y\rho u_\tau/\mu$) is less than one, where u_τ is friction velocity defined as $u_\tau = (\tau_w/\rho)^{0.5}$ and τ_w is wall shear stress. The governing Navier-Stokes equations are discretized by the finite volume method and solved using the commercial software STAR-CCM+³¹ with a second-order upwind scheme for convection terms and second-order implicit scheme for time discretization. The time step is set at 0.01 ms which ensures that the Courant number is less than one. The SIMPLE algorithm is used for pressure-velocity coupling. The Reynolds-Averaged Navier-Stokes equations in tensorial notation for unsteady incompressible flow are³²

$$\frac{\partial U_j}{\partial X_j} = 0 \quad (1)$$

$$\rho \left(\frac{\partial U_i}{\partial t} + U_j \frac{\partial U_i}{\partial X_j} \right) = - \frac{\partial P}{\partial X_i} + \frac{\partial}{\partial X_j} \left[\mu \frac{\partial U_i}{\partial X_j} - \rho \overline{u'_i u'_j} \right] \quad (2)$$

where U_i and u'_i are the mean and fluctuating velocity components, respectively, P is the pressure, and the overbar denotes time-averaged values. Using the Boussinesq assumption, the components of the Reynolds stress tensor are given by³²

$$\rho \overline{u'_i u'_j} = \frac{2}{3} \rho k \delta_{ij} - \mu_t \left(\frac{\partial U_i}{\partial X_j} + \frac{\partial U_j}{\partial X_i} \right) \quad (3)$$

where k is the turbulent kinetic energy, μ_t is referred to as turbulent viscosity and δ_{ij} is the Kronecker delta. In this study, the unsteady Reynolds Stress Model (RSM)³³, which consists of transport equations for each of the stress tensor components, is used to model turbulence.

The Reynolds stress transport equations are

$$\left(\frac{\partial \overline{u'_i u'_j}}{\partial t} + U_k \frac{\partial \overline{u'_i u'_j}}{\partial X_k} \right) = P_{ij} - \epsilon_{ij} + \pi_{ij} - \left(\frac{\partial \overline{u'_i u'_j u'_k}}{\partial X_k} \right) + \frac{\mu}{\rho} \left(\frac{\partial^2 \overline{u'_i u'_j}}{\partial X_k^2} \right) \quad (4)$$

where the production, dissipation and velocity–pressure gradient tensors are defined as

$$P_{ij} = -(\overline{u'_k u'_i} \frac{\partial U_j}{\partial X_k} + \overline{u'_k u'_j} \frac{\partial U_i}{\partial X_k}) \quad (5)$$

$$\epsilon_{ij} = 2 \frac{\mu}{\rho} \left(\frac{\partial \overline{u'_i}}{\partial X_k} \frac{\partial \overline{u'_j}}{\partial X_k} \right) \quad (6)$$

$$\pi_{ij} = -\frac{1}{\rho} u'_j \frac{\partial P'}{\partial X_i} + u'_i \frac{\partial P'}{\partial X_j}. \quad (7)$$

The terms of $\left(\frac{\partial \overline{u'_i u'_j u'_k}}{\partial X_k} \right)$ and $\left(\frac{\partial^2 \overline{u'_i u'_j}}{\partial X_k^2} \right)$ are the turbulent transport and viscous diffusion tensors.

3.3.3. Boundary conditions

Prior to setting up the jet simulation in the computational domain, separate simulations are carried out for flow in a pipe and square duct to establish the flow conditions at the origin plane shown in Fig. 3.1. A steady RANS RSM simulation is performed with uniform inlet flow and an outflow condition at the exit to produce the fully developed flow in the pipe/duct. The fully developed streamwise velocity is validated using the results of den Toonder and Nieuwstadt³⁴ for a round pipe and Hoagland³⁵ for a square duct, as shown in Fig. 3.2(a) and Fig. 3.3(a), respectively. Here U_e is the average velocity at the exit plane and the coordinate Y^+ is indicated to commence at the

walls and extends towards the middle of the duct or pipe. Also, the mean streamwise velocity profile is compared to the law-of-the-wall in Figs. 3.2(b) and 3.3(b).

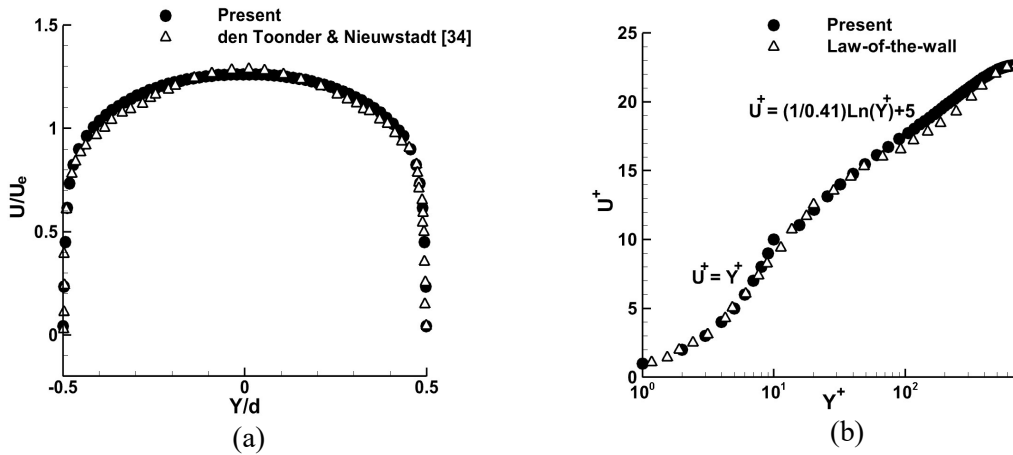


Fig. 3.2 Comparison of fully developed streamwise velocity for a round pipe, with (a) experimental results³⁴, (b) law-of-the-wall

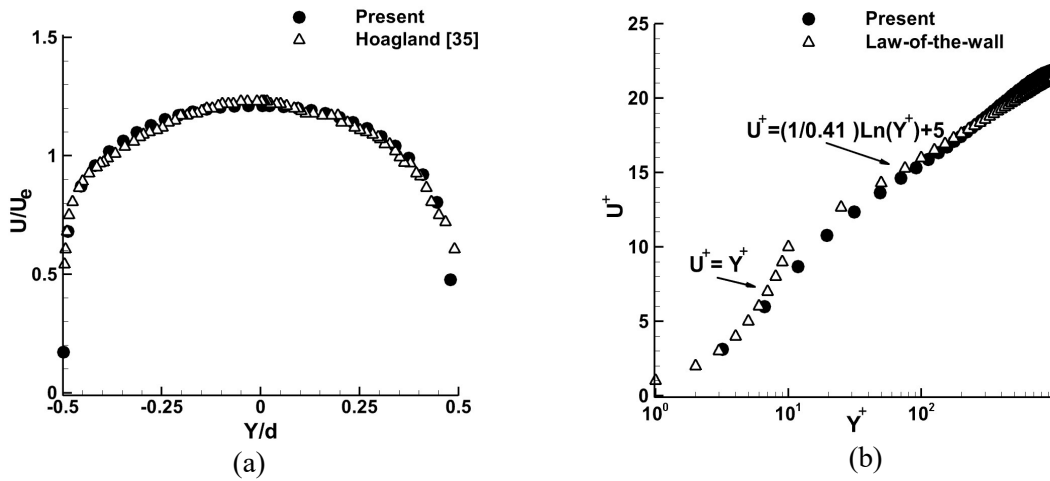


Fig. 3.3 Comparison of fully developed streamwise velocity for a square duct, with (a) experimental results³⁵, (b) law-of-the-wall

The square duct and pipe exit conditions are mapped as the inlet condition for the simulation in the confinement cavity. The inlet boundary conditions are applied inside the nozzles at 20 mm upstream of the exit to ensure an accurate representation of the flow at the exit plane. All smooth walls of the confinement cavity are treated as no-slip boundaries and an outflow condition is applied at the outlet of the computational domain.

3.3.4 Three-dimensional flow visualization

Different vortex identification methods such as Q-criterion, λ_2 -criterion and Δ -criteria have been developed to identify vortex structures in a flow field. The λ_2 -criterion is especially attractive since it is derived from the requirement that the pressure minimum occurs at the vortex core³⁶. In this analysis, λ_2 is the second eigenvalue of $\mathbf{\Omega}^2 + \mathbf{S}^2$ where \mathbf{S} and $\mathbf{\Omega}$ are the shear strain and rotation tensors, respectively, defined as:

$$S_{ij} = \frac{1}{2} \left(\frac{\partial U_i}{\partial X_j} + \frac{\partial U_j}{\partial X_i} \right) \quad (8)$$

$$\Omega_{ij} = \frac{1}{2} \left(\frac{\partial U_i}{\partial X_j} - \frac{\partial U_j}{\partial X_i} \right). \quad (9)$$

Jeong and Hussain³⁷ considered that the pressure minimum occurs at the vortex core. They split the Navier-Stokes equations into symmetric and antisymmetric parts and ignored unsteady and viscous effects to reduce the Navier-Stokes equations to

$$\mathbf{S}^2 + \mathbf{\Omega}^2 \approx -\frac{1}{\rho} \nabla(\nabla P). \quad (10)$$

The Hessian matrix of the pressure has three eigenvalues $\lambda_1 \geq \lambda_2 \geq \lambda_3$ and the local minimum pressure occurs where the Hessian matrix has two positive eigenvalues. These two positive eigenvalues correspond to two negative eigenvalues of $\mathbf{S}^2 + \mathbf{\Omega}^2$, whereby the λ_2 must have a negative value.^{36,37}

3.4. Validation

The present study is validated using the round jet results of Lawson et al.²⁷ and Bensider et al.²⁸ In the remainder of this paper, the tensorial notation is replaced by the conventional Cartesian notation, i.e., the X_i - components of velocity, U_i , are replaced by the X, Y, Z components U, V and W. Initially, the mean velocity of the oscillating jet is considered, and the results are compared with the Laser Doppler Anemometer (LDA) measurements of Lawson et al.²⁷ The multiblock hexahedral mesh used in this study comprises three different regions. A fine mesh (0.2 mm) covers the central core region of the jet, while an intermediate mesh (1.25 mm) is used in the jet expansion region and a coarser mesh (2.5 mm) is used in the outer regions of the cavity. Grid independency was established by comparing results using 6, 10 and 16 million cells. For each of these mesh sizes, Fig. 3.4 depicts a comparison with data from Lawson et al.²⁷ for the time series of the jet

cross-flow velocity at the downstream location (3.2d, 0, -0.9d). It can be observed that the oscillation is dependent on jet flow transport in the transverse direction. The Strouhal number, St_d , based on nozzle diameter, jet frequency (f) and mean jet exit velocity is defined as:

$$St_d = f \times \frac{d}{U_e} . \quad (11)$$

Based on a Fast Fourier Transform (FFT) of the velocity time history, the present simulation predicts a stable oscillation with a dominant frequency and Strouhal number which are in good agreement with the experimental data of Lawson et al.²⁷

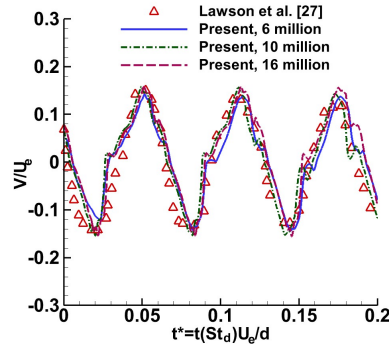


Fig. 3.4 Time series of cross-flow velocity in a round jet at point (3.2d, 0, -0.9d)

The normalized mean streamwise velocity along the jet centerline and along the line $X = 1.35d$, $Z = 0$ are shown in Figs. 3.5(a) and 3.5(b), respectively. The results are compared with that of Lawson et al.²⁷, which confirms the accuracy and grid independence of the present simulation.

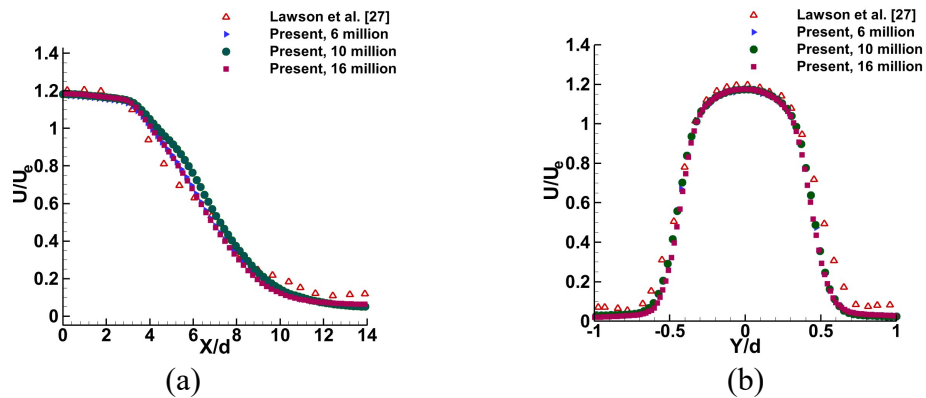


Fig. 3.5 Round jet streamwise velocity profile: (a) along centreline, (b) at $X = 1.35d$

To further validate results for the round jet, normalized Reynolds stresses at point (13d, 2.9d, 0) are compared with the Reynolds stresses $\overline{\rho u' u'}$ and $\overline{\rho v' v'}$ time histories of Bensider et al.²⁸ in Fig.

3.6, showing satisfactory results. The differences noticed in the peak amplitudes may be attributed to the more refined mesh and higher order temporal discretization used in our simulations and the more accurate representation of the inlet flow conditions.

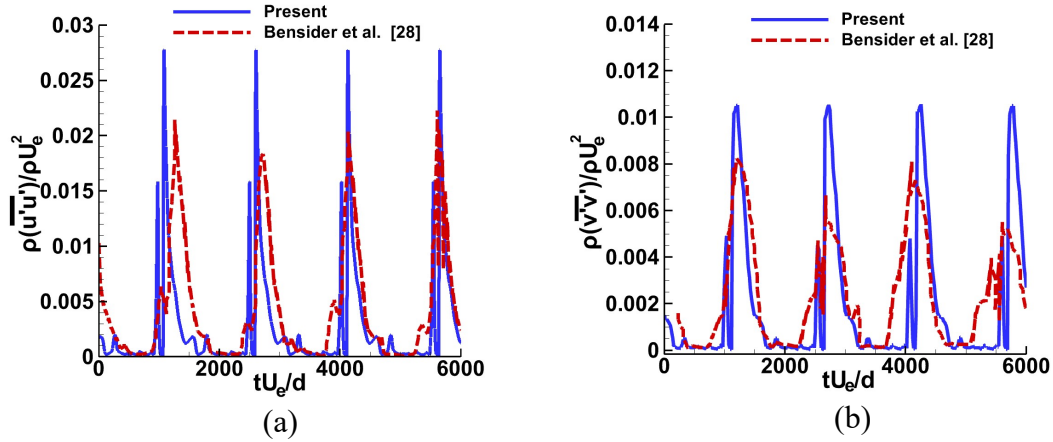


Fig. 3.6 Perpendicular Reynolds stresses at point $(13d, 2.9d, 0)$: (a) $\overline{\rho u' u'}$, (b) $\overline{\rho v' v'}$

Additional validation was considered by comparing the results from a square jet simulation with the results of Kalter et al.²⁵ To enable direct comparison, the Reynolds number and domain geometry were maintained the same as Kalter et al.²⁵ The fluid used in the experiment of Kalter et al.²⁵ was saltwater with constant properties. The streamwise velocity at $X = 8d$ and $X = 18d$ is compared in Fig. 3.7. Although the streamwise velocity in the present study accurately follows the trend in the experimental results, there is a small discrepancy in the value. The jet oscillation frequency evaluation of the velocity-time signal based on FFT at point $(25d, 0, 0)$ was found to be in excellent agreement with the experiment.

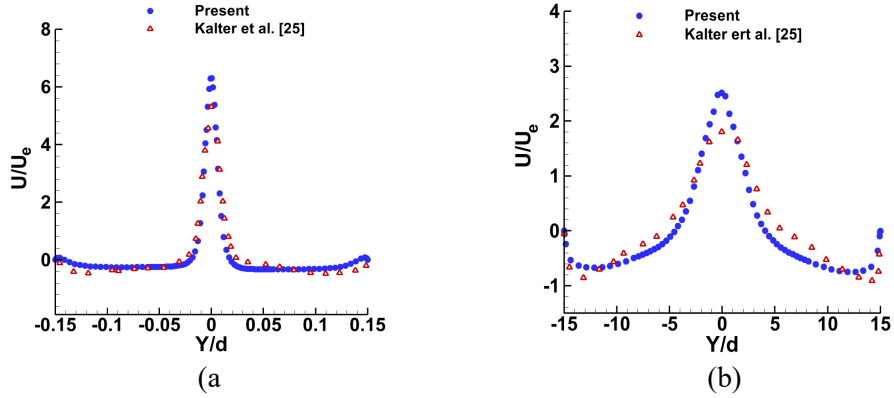


Fig. 3.7 Mean streamwise velocity on $Z = 0$ for a square jet at (a) $X = 8d$, (b) $X = 18d$

3.5 Results and discussion

3.5.1 Instantaneous near-field vortex deformation

It is well known that in a round jet, a vortex ring forms at the nozzle exit due to the roll-up of the shear layers at the edge of the jet due to Kelvin–Helmholtz instabilities. Figure 3.8 shows the evolution of the vortex ring in the present study for the round jet. The isosurface of λ_2 is used to identify the vortex structures in the starting jet flow ($t < 0.1$ s). The value of λ_2 is taken equal to -1 to enable the identification of the major vortical structures. The isosurface is colored by the streamwise velocity. A front view of the vortex evolution is shown in the top row of Fig. 3.8(a) at dimensionless times from $t^* = 1$ to 50, where the dimensionless time is defined as $t^* = U_e t / (0.42d)$. The value of 0.42 is included in the non-dimensional time to support visualization at integer t^* values and has no special significance¹³. The vortex ring radius and the shear layer thickness increase as the ring travels downstream. Eventually, the axisymmetric vortex ring becomes distorted and breaks down due to azimuthal instabilities, which create secondary rib vortices between two consecutive vortex rings as seen in the second row of Fig. 3.8(a). This process increases entrainment as the primary and secondary vortices interact. The vortex pattern until $t^* = 10$ is very similar to that noticed in previous free jet studies³⁸ and serves to further validate the present simulation. As the rings move farther downstream (view at $t^* = 50$), the distorted vortex ring collapses due to its interaction with the confinement wall. Figure 3.8(b) illustrates the $Y = 0$ cross-section of the vortex shedding process showing the eventual break down of the vortex rings.

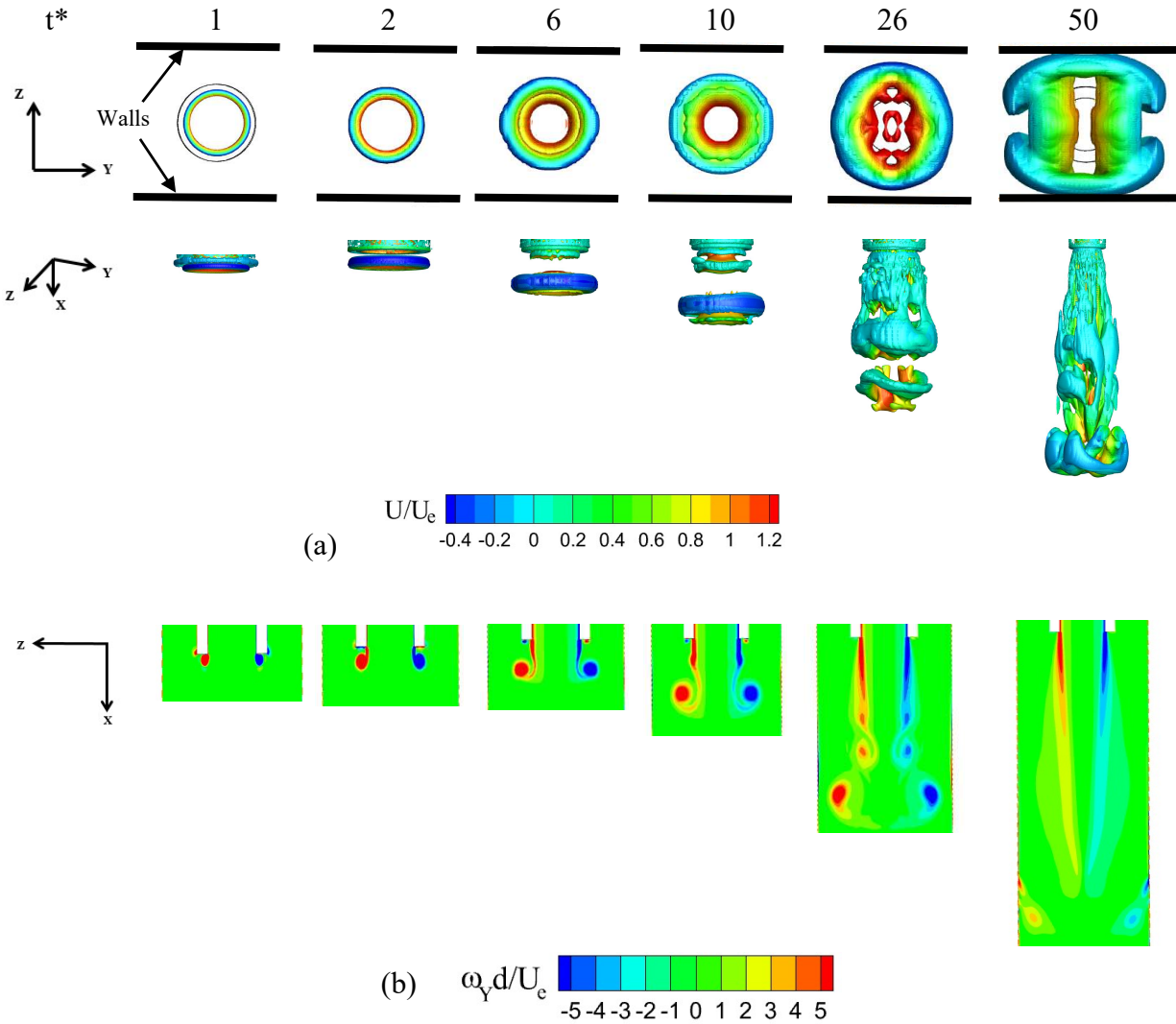


Fig. 3.8 Instantaneous vortex deformation of a round jet: (a) front and side views of $\lambda_2 = -1$ isosurface colored by streamwise velocity, (b) vorticity contours on the plane $Y = 0$

A similar vortex pattern for the square jet is shown in Fig. 3.9(a). At $t^* = 1$, the vortex ring has not yet deformed and has a near square shape. Small distortions of the ring are visible at $t^* = 2$ and axis-switching occurs at about $t^* = 6$, due to higher streamwise velocity at the corners of the ring compared to the flat sides, causing the square ring to rotate 45° . Axis-switching generates hairpin vortices at the corners of the ring which enhances the entrainment and mixing processes¹³. The results show that axis-switching occurs at $X/d \sim 0.7$ and that the wall confinements do not have much effect on the axis-switching location. These results are in good agreement with free square jet simulations of Ghasemi et al.¹³ who showed that axis-switching occurs at $X/d = 0.65$ from the nozzle exit plane. Figure 3.9(b) illustrates the vortex formation in the $Y = 0$ plane of the square

jet, showing the growth in the shear layers, vortex ring development, wall interaction and eventual break down of the vortex ring.

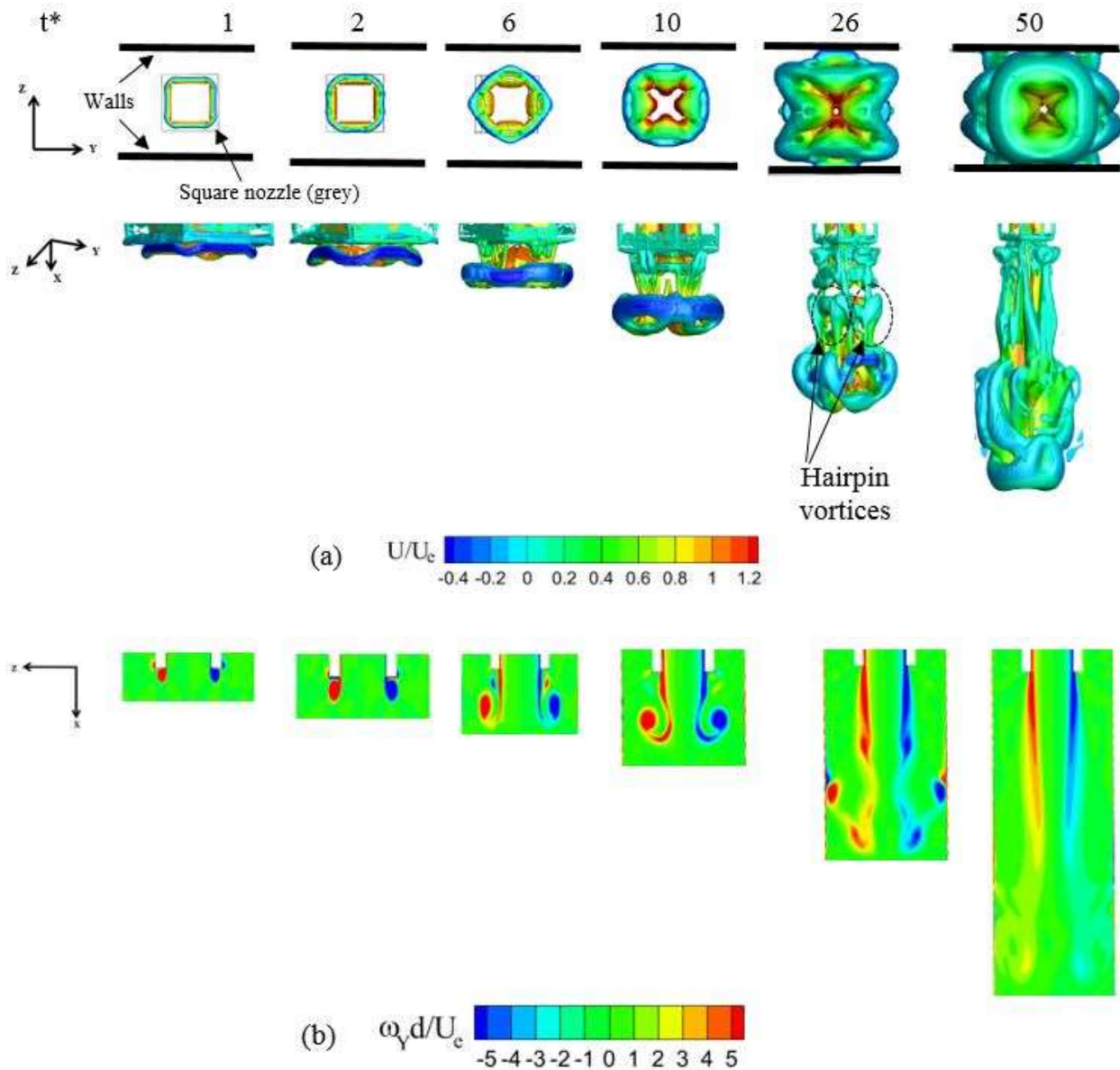


Fig. 3.9 Instantaneous vortex deformation of a square jet: (a) isosurface of λ_2 colored by streamwise velocity, (b) vorticity contours at plane $Y=0$

Observing a series of images, including the ones shown above, indicates that the square jet vortex ring attaches to the wall earlier, at about $t^* = 26$ ($t = 0.04$ s), while the round jet vortex ring wall attachment occurs at $t^* = 40$ ($t = 0.062$ s). The earlier wall attachment of the square vortex ring is due to vortex axis-switching which rotates the vortex ring corners and decreases the distance between the vortex and the walls. Unlike the round jet, the square jet creates hairpin-like (braid)

vortices due to the axis-switching, as illustrated in Fig. 3.9(b). The stretching and contraction of the vortex rings creates the hairpin-like vortices which were reported by Grinstein and Devore⁶. These braid vortices link two consecutive deformed vortex rings together as shown at times $t^* = 10$ and $t^* = 26$. Eventually, as the jet develops and the vortex rings move downstream, the hairpin-like vortices act as connectors between the deformed rings. The strong interaction of the vortex rings and braid vortices results in vortex ring break down which can be seen in Fig. 3.9(b) at $t^* = 50$.

3.5.2 Effects of confinement on vortex deformation

The effects of wall confinement appear as the jet penetrates farther downstream into the cavity. In Figs. 3.10 and 3.11, the distortion of the vortex ring using λ_2 equal to -1 is shown after it collides with the walls, i.e., after $t^* = 40$ for the round jet and $t^* = 26$ for the square jet. The first row in the figures show the view looking into the X-Z plane (strong confinement) while the second row illustrates the view from the X-Y plane (less confinement side). Due to the Biot-Savart law³⁹, as the vortex ring approaches the wall it creates a vortex layer on the wall. The sign of vorticity near the wall is opposite to that of the primary vortex ring and the interaction between the two vortices increases the rate of vortex decay. As the vortex ring approaches the wall, the wall vortex layer partially separates from the wall and a secondary vortex forms that twists around the deformed vortex ring. As it travels further downstream the vortex ring stretches and becomes thinner. The fluid near the wall entrains into the vortex ring and two tornado-like vortices are created, as seen in Figs. 3.10(e) and 3.11(e). During the connection process of the primary and secondary vortices, the vorticity direction changes from Y to Z-direction. Similar tornado-like vortices have been reported by Chang and Hertzberg¹⁸ at low Reynolds number. As the flow moves downstream, the distance between the two tornado-like vortex cores increases. There is no significant difference between the vortex ring deformation of the round and square jets after attaching to the confinement walls including the formation of the tornado-like vortices.

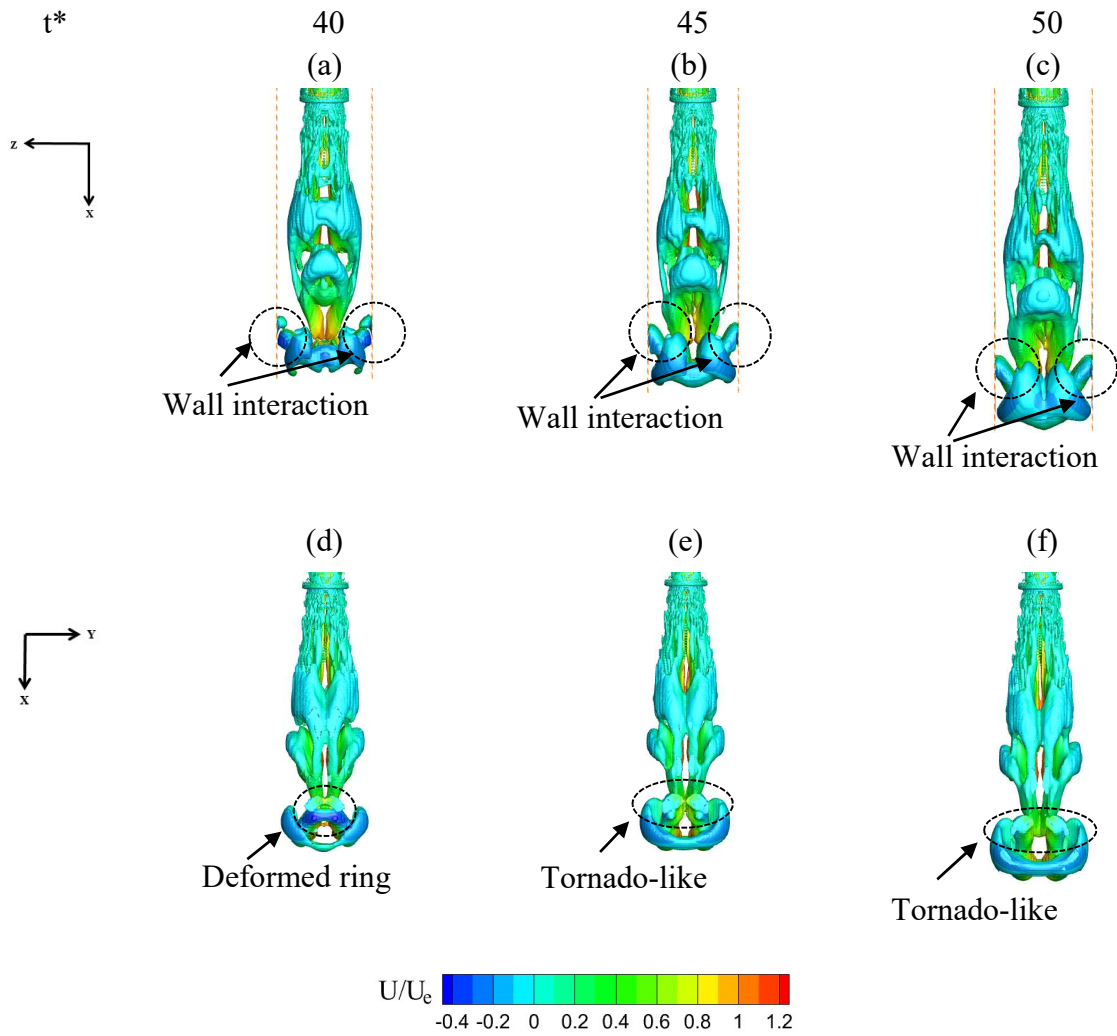


Fig. 3.10 Vortex interaction of the round jet with confinement wall at selected dimensionless times:
 (a,d) $t^* = 40$, (b,e) $t^* = 45$, (c,f) $t^* = 50$

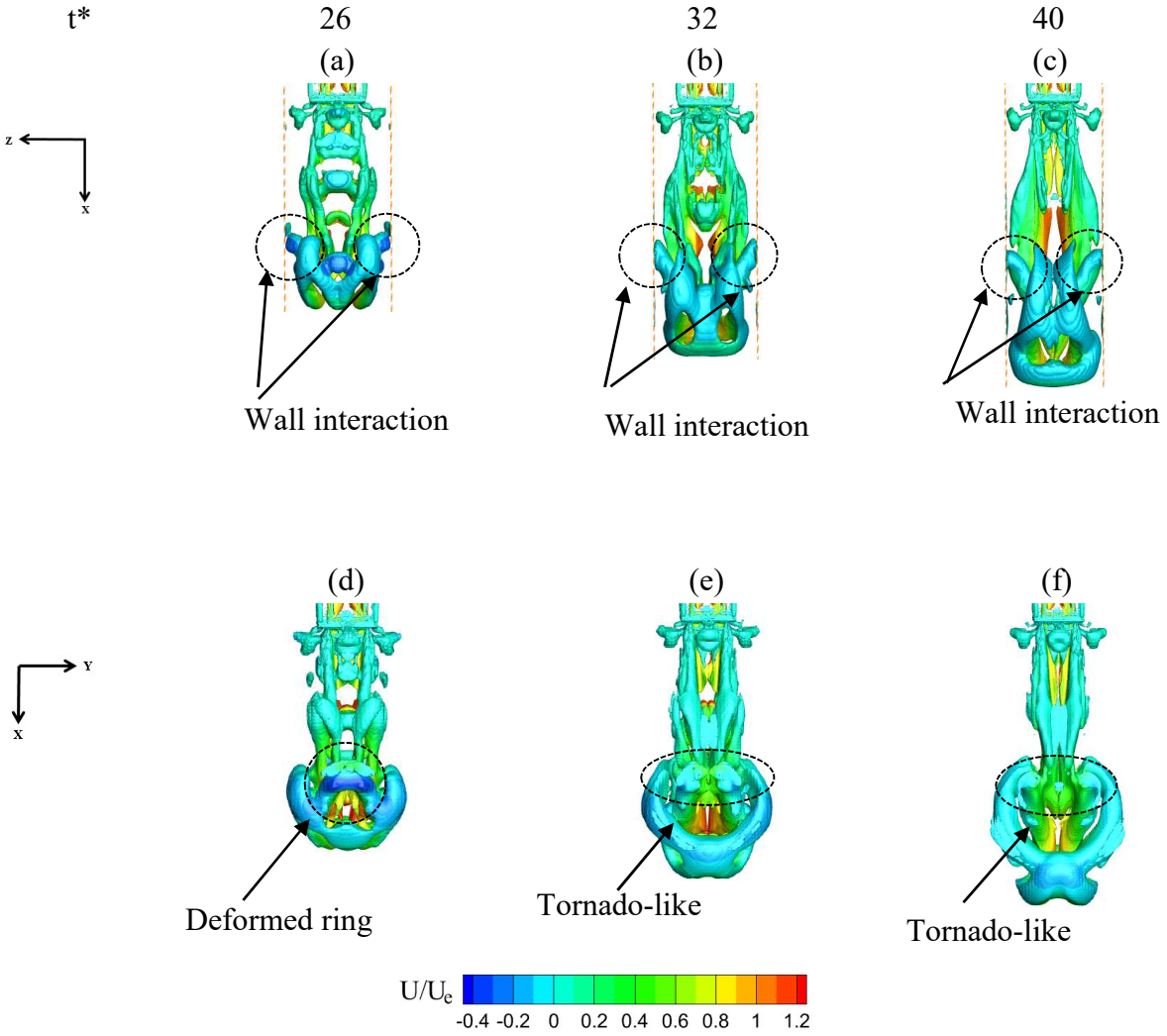


Fig. 3.11 Vortex interaction of square jet with confinement wall at selected dimensionless times: (a,d) $t^* = 26$, (b,e) $t^* = 32$, (c,f) $t^* = 40$

3.5.3 Oscillation mechanism

As demonstrated above, there is little qualitative difference between the round and square jet vortex ring behavior once the ring strikes the confinement wall. The present simulations indicate that both types of jets also display a similar pattern of oscillation. As the jet oscillates in the cavity, it attaches to one of the side walls followed by detachment and movement towards the other wall. This process continues to occur in a repeating fashion. The attachment locations on the side walls of the cavity for both the round and square jets are at the same distance from the nozzle exit. The frequency of oscillation for both the square and round jets is about 0.19 Hz.

For brevity, the square jet is used to elucidate the oscillation mechanism. Figure 3.12 shows the vorticity (ω_z) contours superimposed with the velocity vectors in the XY plane ($Z = 0$) over a

half-cycle of oscillation. It is well-known that due to the Coanda effect, the jet initially attaches to one side or the other depending on the randomness of the flow turbulence. At $t = t_0$, the jet is shown deflected to the left side wall and the velocity vectors indicate the formation of four rotating regions, indicated by A, B, C and D. When the jet impinges on the left side wall at $t = t_0$, the flow splits and creates the counterclockwise vortex A below the impingement point (I) and clockwise vortex B above the impingement point. The high vorticity noted along the right shear layer (indicated by red) tends to feed vortex A and the one on the left (blue) feeds vortex B. The corner vortices C and D with opposite sense of rotation are formed due to the flow being constrained at the top. Figure 3.13 illustrates the corresponding pressure contours superimposed with streamtraces. As vortex A in the high-pressure region grows, it gets constrained by the side walls of the cavity and the flow tends to move upwards, which then begins to squeeze vortex D (located in the low-pressure region) at the top right corner of the cavity and the fluid is transported around the nozzle. Due to continuity considerations and confinement effect of the cavity, a downward flow is established at the top left corner, which washes out vortex C and vortex B is moved downwards towards the bottom of the cavity as seen at $t = t_0 + T/4$. Simultaneously, as vortex A moves upwards into the low-pressure region, there is room for vortex B to expand, forcing the jet to move to the opposite side of the cavity at $t = t_0 + T/2$. The flow fields at $t = t_0$ and $t = t_0 + T/2$ are mirror images about the cavity centerline and, during the time interval from $t_0 + T/2$ to T , the above process is repeated (in reverse) to divert the jet back to the left side wall, completing one oscillation cycle.

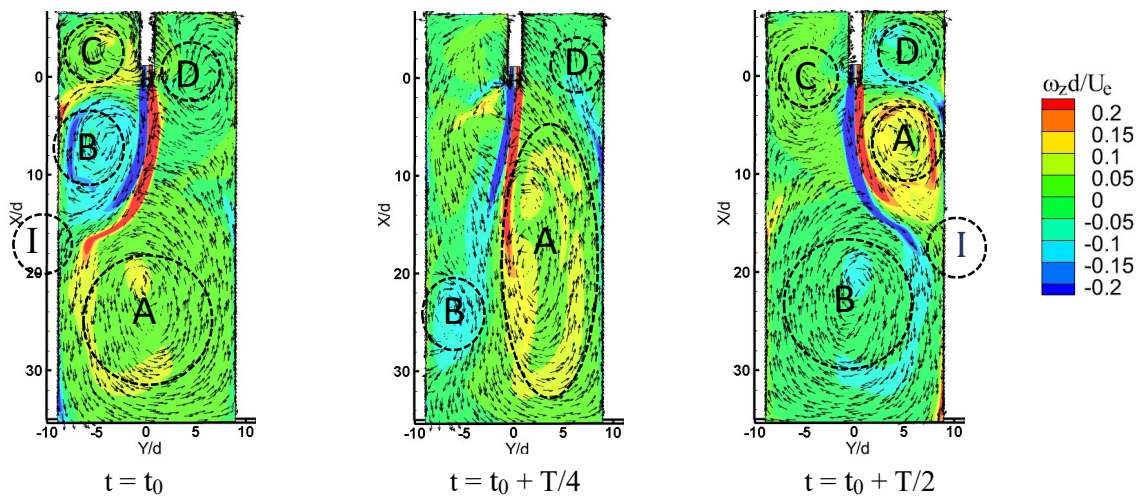


Fig. 3.12 Instantaneous velocity vectors of the oscillating square jet, superimposed on the vorticity contours on the plane $Z = 0$, during a half period ($T/2$)

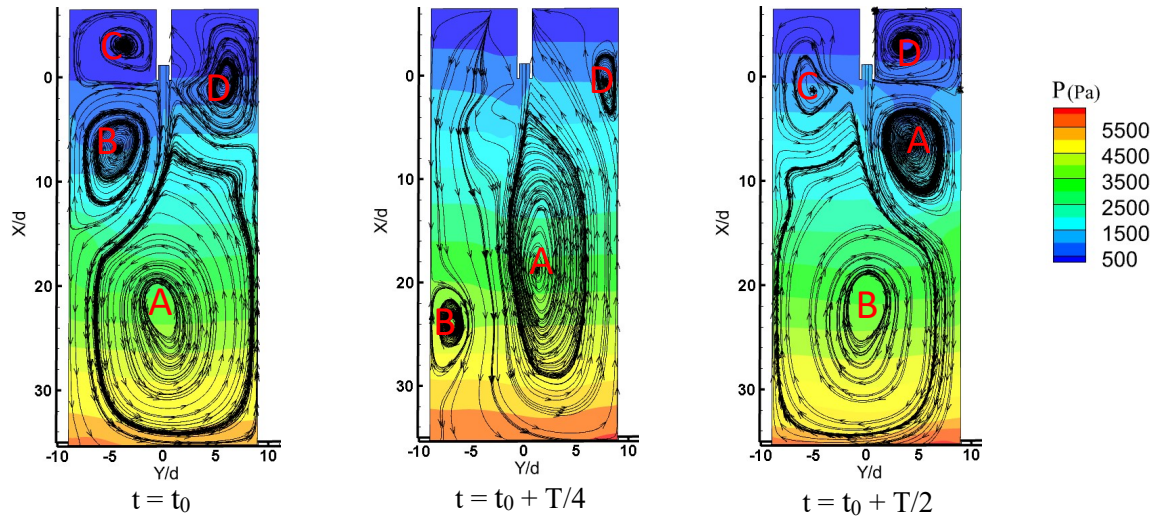
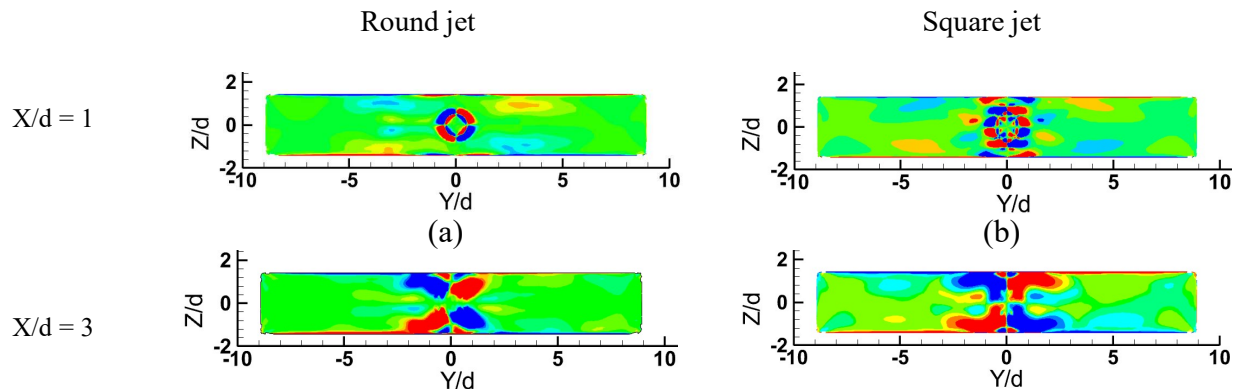


Fig. 3.13 Instantaneous streamtraces of the oscillating square jet, superimposed with static pressure (Pa) contours on the plane $Z = 0$, during a half period ($T/2$)

3.5.4 Mean vorticity

The vorticity fields at various downstream transverse planes from $X/d = 1$ to 10 are shown in Fig. 3.14. A comparison of the vorticity field of the two types of jets indicates that there are additional triangle-shaped eddies (see Figs. 3.14(a, b)) at $X/d = 1$ in the square jet. These additional eddies are a result of the secondary flow that occurs inside the square duct prior to the flow existing the nozzle and are transported out into the jet, as seen in the zoomed view at $X/d = 0.1$ in Fig. 3.14(i). The secondary eddies are generated due to an imbalance of momentum between the core and corners in the internal duct flow. These eddies redistribute the excess momentum from the core towards the corners. As indicated earlier, following collision with the walls around $X/d \sim 4$, the jet spreads in the Y -direction. The square jet attaches to the confinement walls earlier as illustrated in Figs. 3.10 and 3.11. For $X/d > 3$, there is not much difference between the round and square oscillating jets. As the jets move downstream, the eddies merge and the distance between the counter-rotating vortex cores increases (Figs. 3.14(g, h)).



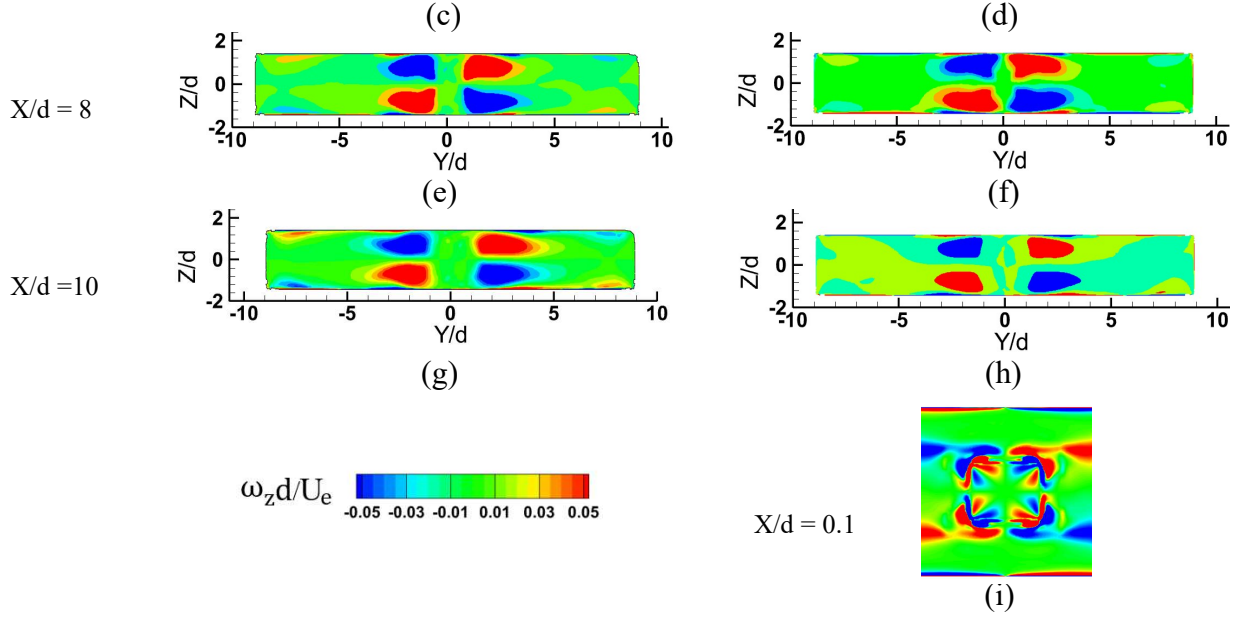


Fig. 3.14 Mean streamwise vorticity field at the YZ plane: (a, c, e, g) round jet, (b, d, f, h) square jet, (i) zoomed view near the square nozzle exit

3.5.5 Mean centerline velocity decay and jet width

It is common practice to quantify the centreline velocity decay and jet half-width to enable comparison between different types of jets. To this end, the normalized centerline velocity (U_j/U_{c1}) of both oscillating square (OS) and oscillating round (OR) jets are plotted in Fig. 3.15. Here U_{c1} is the centerline mean velocity at any X/d and U_j is the centerline jet exit velocity. It has been previously shown that the shape of the nozzle exit velocity profile (top-hat or fully developed) does not have a significant effect on the decay rate of the round jet⁴⁰. This result is confirmed by the decay rate comparison of the present simulations of free round (FR) and free square (FS) jets with fully developed inlet flow and the top-hat inlet flow of Tandalam et al.² (see inset in the figure 3.15). The centerline velocity decay of the confined oscillating and free jets for $X/d < 4$ is nearly the same and has a similar trend as the free jets of Quinn and Militzer⁴ and Ghasemi et al.¹². The nozzle cross-sectional shape affects jet entrainment and the higher entrainment of square jets, in the region $3 < X/d < 6$, is due to the interaction of the primary and secondary vortices during the axis-switching process. Higher entrainment reduces the length of the potential core of the square jet. In this work, the potential core length is defined as the distance from nozzle exit to the axial location where the centerline velocity is reduced to 99% of the nozzle centerline exit velocity. The extent of the potential core of the confined OR and OS jets are $3.8d$ and $3.3d$, respectively. Near

$X/d \sim 4$, the outward growth of the outer shear layers is interrupted in the Z-direction as the jet has now fully expanded to the width of cavity. This results in no further entrainment in this direction, however the jet continues to expand and entrain fluid in the Y-direction. Coupled with oscillations, this allows for entrainment and expansion of the jet, resulting in the overall increase of the transverse extent of the jet. For $X/d > 6$, Fig. 3.15 shows that the centerline velocity decay increases significantly in both round and square oscillating jets. The round oscillating jet decay rate (k_d) for $X/d > 6$, evaluated by a linear fit to the data, shows a higher value compared to the oscillating square jet (Table 3.1).

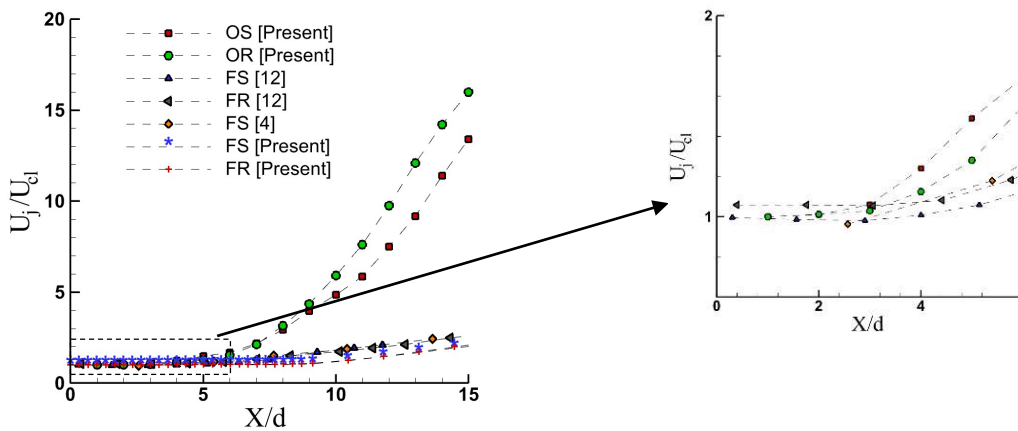


Fig. 3.15 The decay of centerline velocity (Jet types: OS - oscillating square, OR - oscillating round, FS - free square, FR - free round)

Table 3.1. Jet decay and spread rates of round and square oscillating jets

	Round oscillating jet		Square oscillating jet		Free square jet
	$3 < X/d < 6$	$6 < X/d < 15$	$3 < X/d < 6$	$6 < X/d < 15$	$6 < X/d < 15$
k_d	0.17	1.5	0.21	1.3	0.16
k_s	0.23 ($9 < X/d < 15$)		0.26 ($9 < X/d < 15$)		0.11

Figure 3.16 shows the half-width of the free square jet and round and square oscillating jets, normalized by the hydraulic diameter of the nozzle. The half-width is defined as the spanwise distance from the jet centerline to a lateral location where the mean velocity is one-half of the centerline streamwise velocity. As Fig. 3.16 illustrates, the square jet has a slightly larger jet width, especially for $X/d > 6$, which is due to higher entrainment. In the square jet, axis-switching in the near-field increases entrainment of the surrounding fluid into the jet, and mixing enhancement occurs. Higher entrainment increases the square jet spread rate (k_s). From the data in Table 3.1, the spread rate of the square and round jets are 0.26 and 0.23, respectively. This is contrary to free round and square jets which have similar decay and spread rates as reported by Quinn and Militzer⁴

and Ghasemi et al.¹². A comparison of free and oscillating jets shows that the spreading of the free jet and the oscillating jet is almost the same for the near-field ($X/d \leq 5$). Further downstream, the spread increases due to jet oscillation and higher entrainment. For example, the jet width at $X/d = 15$ is 2.2, 1.9 and 1.4 for the OS jet, OR jet and FS jet, respectively. These results provide evidence that the oscillating jet has better mixing than the free jet.

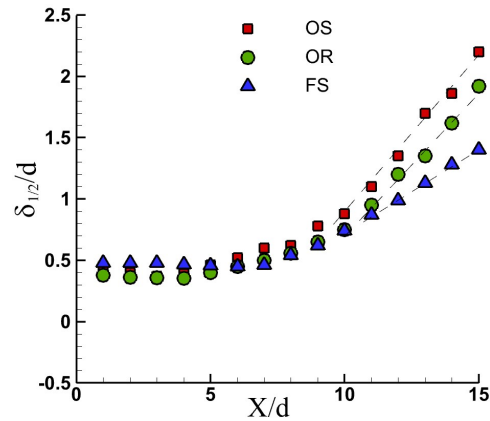


Fig. 3.16 Jet thickness of round and square oscillating jets and free square jet

Figure 3.17(a) shows the streamwise velocity of oscillating jets at various distances from the nozzle exit. At the nozzle exit, the velocity profile is fully developed. Over the region $0 < X/d < 7$, the peak value decreases by $\sim 50\%$ due to entrainment of the surrounding fluid. The jet oscillation causes the single peak to change into two milder peaks that move towards the side walls with increasing X/d (see $X/d = 11$). By $X/d = 15$, the peaks die out and the velocity of oscillating jets is closer to a uniform distribution. In the case of oscillating jets, the flow velocity near the walls ($Y/d > 7$) can either be upwards or downwards, as shown in Fig. 3.17(b). This is due to the formation of clockwise and counterclockwise re-circulating regions discussed above and illustrated in Fig. 3.12.

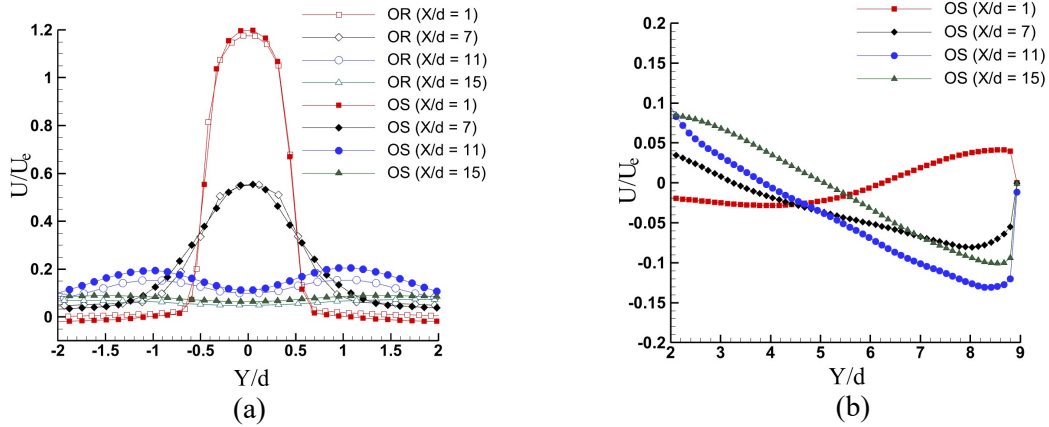


Fig. 3.17 Development of mean streamwise velocities profiles: (a) oscillating and free jets, (b) oscillating square jet near the wall

The normalized mean spanwise velocity profiles in the XY plane are shown in Fig. 3.18. The spanwise velocity illustrates the effects of oscillation on the jet entrainment and jet spread. The positive and negative spanwise velocities show outward flow away from the jet axis and inward flows toward the jet axis due to entrainment, respectively. At $X/d = 1$, the negative spanwise velocity for the oscillating square jet is 40% higher than for the oscillating round jet near the jet center ($\sim Y/d = 1$). This higher value for the OS jet is due to axis-switching. The oscillating jets demonstrate only inward flow towards the jet center for $1 < X/d < 7$. By $X/d = 11$, the amount of inward flow is significantly reduced, almost to zero in the OR jet. As flow proceeds downstream ($X/d = 15$) the entrainment is reduced and only outward flow occurs. Furthermore, at $X/d = 15$, the flow moves away from the core to the side walls in the XY plane and moves from the confinement walls to the jet centerline in the XZ plane.

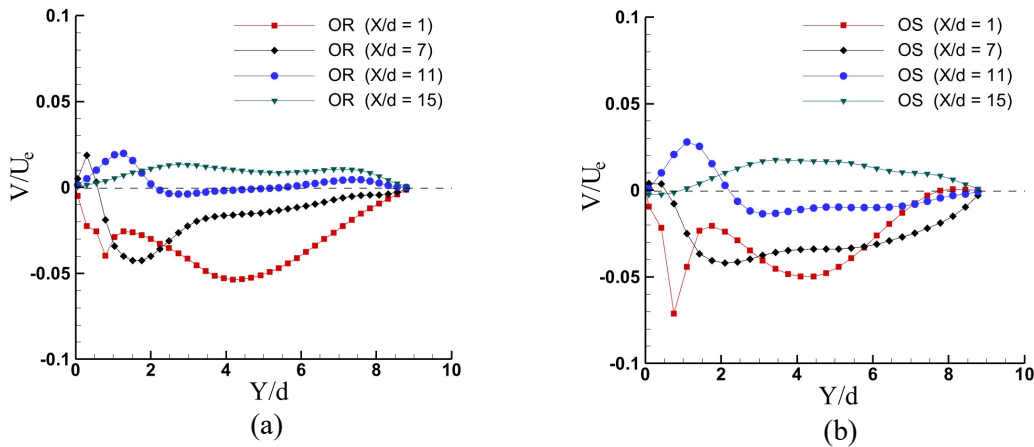
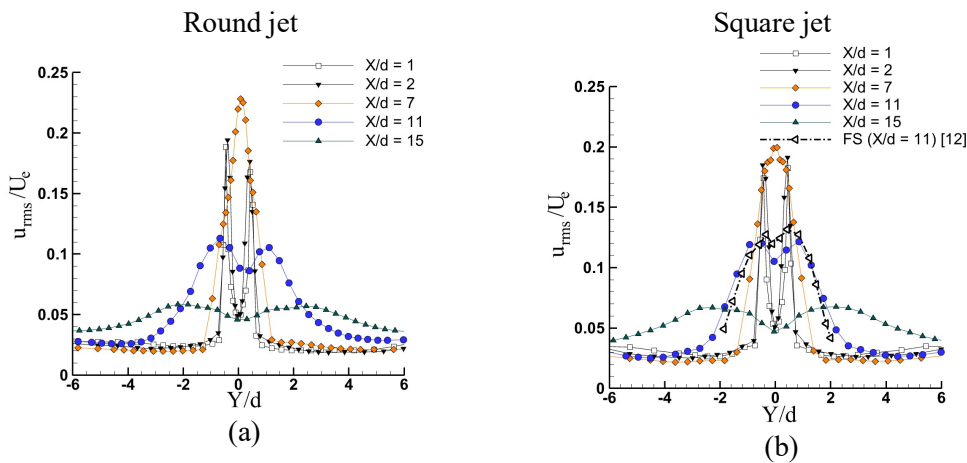


Fig. 3.18 Development of the profiles of the spanwise mean velocities: (a) oscillating round jet, (b) oscillating square jet

3.5.6 Turbulence intensity and Reynolds shear stress

The streamwise turbulence intensity u_{rms}/U_e , where u_{rms} is the root mean square value of the streamwise velocity fluctuations, is shown at various axial locations in Fig. 3.19. Near the nozzle ($X/d = 1, 2$), two peaks in the profiles occur in the vicinity of the shear layers due to the high production of turbulence in these regions. The confinement walls decrease the entrainment in the Z-direction and the walls provide for an increase in turbulence dissipation and a decrease in turbulent kinetic energy. Higher u_{rms} is due to momentum transport from the spanwise and lateral directions to streamwise direction during jet spreading. The results show an increase in the peak values of turbulence intensity for OS and OR jets moving downstream until $X/d \sim 7$, where the turbulence intensity value at the centerline is highest with one peak. Beyond $X/d = 7$, the turbulence intensity decays as jet oscillations become the dominant feature of the flow. A significant difference between OS and OR jets is illustrated in the streamwise turbulence intensity profiles in the XZ plane. Unlike the round jet, axis switching of the square jet (at $X/d \sim 0.7$) produces a second peak at $X/d = 1$ and 2 which is indicated in Fig. 3.19(d). The OS and OR jets show the same overall trend and the peak values are almost the same for $X/d > 11$. However, for $X/d < 11$, the turbulence intensities are 20% higher for the round jet. Compared to the free jet¹², oscillating jets have lower turbulence intensity near the center of the jet ($|Y/d| < 1$) and a higher value farther from the center ($|Y/d| > 1$). For instance, Figs. 3.19(a,b) show that the FS turbulence intensity near the center is 15% higher than the OR and OS jets at $X/d = 11$. Farther downstream at $X/d = 15$, the FS turbulence intensities are zero for $|Y/d| > 3$, while the turbulence intensity values of the OS and OR jets are about 5%.



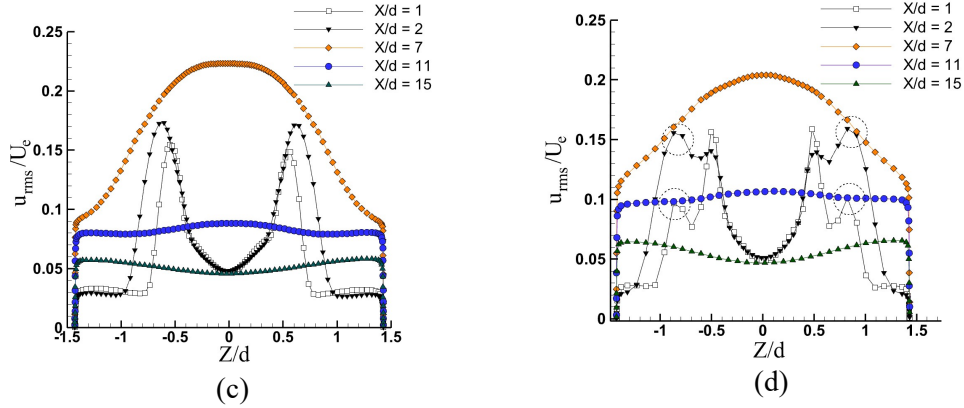


Fig. 3.19 Streamwise turbulence intensity profiles, u_{rms}/U_c : (a) round jet in XY plane, (b) square jet in XY plane, (c) round jet in XZ plane, (d) square jet in XZ plane

The centerline turbulence intensity values for the round and square jets are shown in Fig. 3.20, normalized by jet mean centerline velocity, U_{cl} . The turbulent intensity near the nozzle is low but as the jet evolves downstream the turbulence intensity increases due to higher entrainment. The effects of confinement and oscillation are observed farther downstream. For $X/d > 4$, centerline turbulence intensity values of both oscillating jets increase, with OR jets increasing more rapidly. The round and square oscillating jets shows almost the same rate of decay of turbulence intensity for $X/d < 6$, with the round nozzle producing a higher ($\sim 10\%$) turbulence intensity for $X/d > 6$. The centerline turbulence intensity of a free jet gradually becomes constant with an asymptotic value of ~ 0.2 as reported by Ghasemi et al.¹² and Quinn and Militzer⁴. In contrast, the oscillating jet centerline turbulence intensity does not attain an asymptotic value, reaching a maximum value at $X/d \sim 13$ before decreasing.

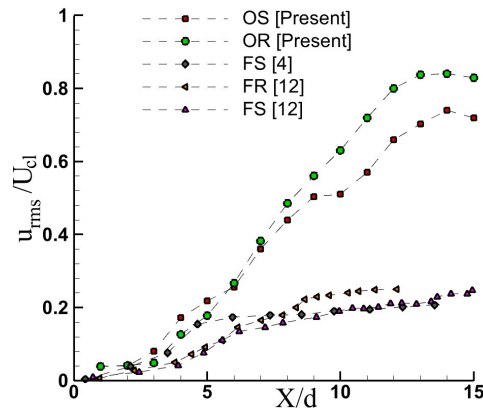
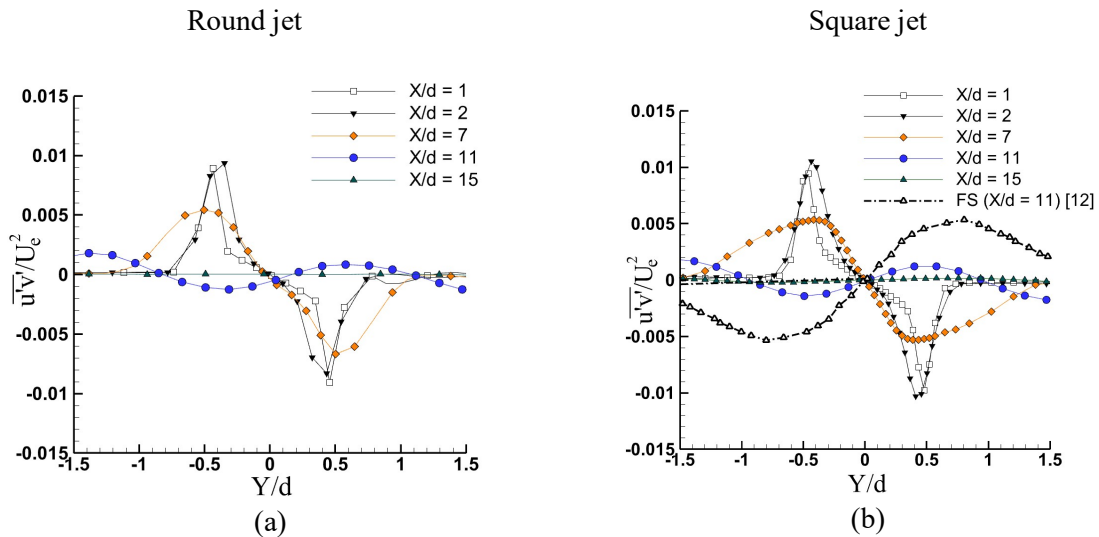


Fig. 3.20 Comparison of streamwise centerline turbulence intensities with experimental and other CFD data for free jets

The normalized Reynolds shear stress for both the square and round oscillating jets are shown on the $Z = 0$ plane in Figs. 3.21(a,b) and on the $Y = 0$ plane in Figs. 3.21(c,d). As illustrated, the maximum absolute shear stress occurs along the shear layers due to maximum velocity gradient in these regions and the minimum occurs at the center ($Y = 0$). The OS and OR jets show the same trend in the Reynolds shear stress distribution. The profiles show two peaks until $X/d \sim 7$, while for $X/d > 7$ four peaks are produced due to the oscillating motion of the jets, in contrast to the free jet where there are only two peaks as reported by Shinnee et al.³ At a farther downstream distance, the maximum Reynolds stresses ($\overline{u'v'}/U_e^2$ and $\overline{u'w'}/U_e^2$) decrease and shift toward the walls where it falls to zero. Eventually the peaks dissipate, and several mild peaks are observed. The highest value of shear stress drops from 1% near the nozzle to 0.1% at the downstream. Also, at farther distance from the center, $|Y/d| > 3$, the oscillating jet Reynolds shear stress value ($\overline{u'v'}/U_e^2$) reduces from 0.1% to zero at the wall where the effects of confinement suppress the Reynolds shear stress. Around the centerline, the shear stress shows a near linear behavior, which was also reported by Shinnee et al.³ The oscillating jet increases entrainment which decreases the jet momentum, resulting in a lower Reynolds shear stress for OS and OR jets compared to the FS jet¹² (see Fig. 3.21(b)).



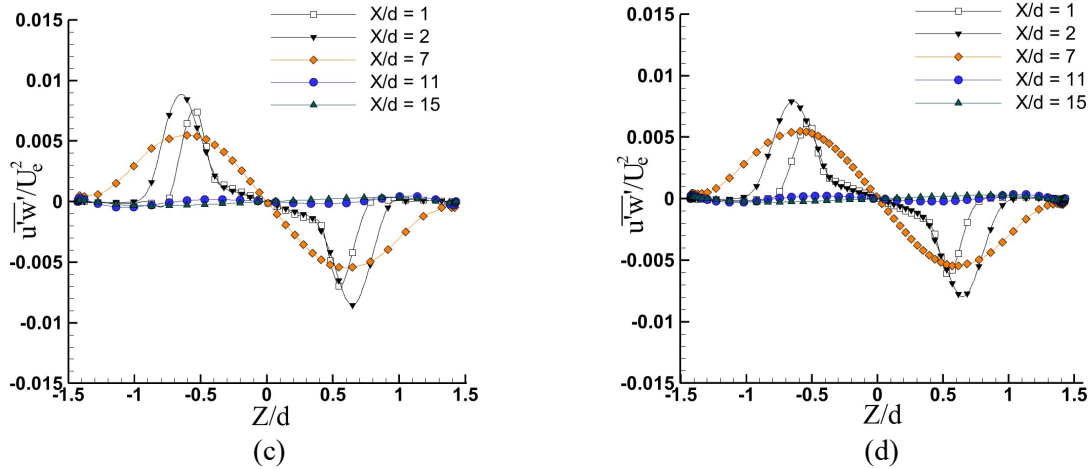


Fig. 3.21 Reynolds shear stress on $Z = 0$ plane: (a) round jet, (b) square jet; Reynolds shear stress on $Y = 0$ plane, (c) round jet, (d) square jet

3.6 Conclusions

In this study, the unsteady Reynolds stress turbulence model is used to investigate vortex ring deformation and present a detailed comparison between confined round and square jets at a Reynolds number of 54,000. To this end, the deformation of the vortex structures was carefully observed at the start of the jet flow and as it impinges on the confinement walls. Examination of the instantaneous vortex deformation shows that for the square jet, axis-switching occurs at approximately 0.7 diameters from the nozzle exit. This result is consistent with previous free square jet studies. For both confined jets studied herein, it is shown that the deformed ring converts to two tornado-like vortices and the vorticity direction changes from the confinement direction to the spanwise direction as the jet penetrates further into the cavity. A comparison of the oscillating round and square jets shows that nozzle geometry shape does not affect the impingement point of the jet on the side walls nor the frequency of oscillation. The oscillating round jet shows a lower decay rate in the region $3 < X/d < 6$ and higher decay rate for $6 < X/d < 15$ compared to the square jet. The spanwise velocity of both oscillating jets show an inward only flow in the XY plane for $X/d = 1$ to 7, and an outward flow at $X/d = 15$. The streamwise turbulence intensities demonstrate two peaks in the near-field, and a single peak at $X/d = 7$. Farther downstream, the turbulence intensity decreases due to jet oscillation and two peaks reappear. Investigation of the Reynolds shear stress shows the minimum values at the centerline for both oscillating jets. The results show that the oscillating square jet has a wider spread compared to the round jet, and both have wider jet spread (40% higher) than the corresponding free jets. The greater jet spread can be used to

achieve more surface temperature uniformity over a larger surface area in heat transfer applications. Comparison between free and confined oscillating jets shows the advantages of using oscillating jets in certain industrial applications.

Nomenclature

d	Nozzle diameter
f	Frequency
FS	Free square
OR	Oscillating round
OS	Oscillating square
P	Pressure
P_{ij}	Production tensor
t	Time (s)
T	Period of oscillations (s)
S	Strain tensor
St_d	Strouhal number
U_e	Nozzle exit average velocity ($m\ s^{-1}$)
U_{cl}	Jet centerline velocity ($m\ s^{-1}$)
U_j	Maximum value of U_{cl} ($m\ s^{-1}$)
U, V, W	Mean velocity ($m\ s^{-1}$)
u', v', w'	Velocity fluctuations ($m\ s^{-1}$)
u_{rms}	Streamwise rms value ($m\ s^{-1}$)
v_{rms}	Spanwise rms value ($m\ s^{-1}$)
w_{rms}	Confined direction (Z) rms value ($m\ s^{-1}$)
X, Y, Z	Cartesian coordinates
Y^+	Wall normal distance
δ_{ij}	Kronecker delta
ϵ_{ij}	Dissipation tensor
π_{ij}	Velocity–pressure gradient tensor
ρ	Density
μ	Dynamic viscosity
Ω	Rotational tensor
μ_t	Turbulent viscosity

ω	Vorticity
$\lambda_1, \lambda_2, \lambda_3$	Eigenvalues of $-(S^2 + \Omega^2)$

Acknowledgement: This research was made possible by the facilities of the Shared Hierarchical Academic Computing Network (SHARCNET: www.sharcnet.ca) and Compute/Calcul Canada, and funding from the Natural Sciences and Engineering Research Council Discovery Grant program.

Data Availability Statement: Raw data were generated at the University of Windsor CFD Lab facility. Derived data supporting the findings of this study are available from the corresponding author upon reasonable request.

References

1. M.T. Kandakure, V.C. Patkar and A.W. Patwardhan, “Characteristics of turbulent confined jets,” *Chemical Engineering and Processing* 47, 1234–1245 (2008).
2. A. Tandalam, R. Balachandar and R. Barron, “Reynolds number effects on the near-exit region of turbulent jets,” *J. Hydraul. Eng.* 136, 633-641 (2010).
3. A.M. Shinneeb, R. Balachandar and J.D. Bugg, “Confinement effects in shallow-water jets,” *J. Hydraul. Eng.* 137, 300-314 (2011).
4. W.R. Quinn and J. Militzer, “Experimental and numerical study of a turbulent free square jet,” *Phys. Fluids* 31, 1017–1025 (1988).
5. W.R. Quinn, “Streamwise evolution of a square jet cross section,” *AIAA J.* 30, 2852-2857, (1992).
6. F.F. Grinstein and C.R. Devore, “Dynamics of coherent structures and transition to turbulence in free square jets,” *Phys. Fluids* 8, 1237–1251 (1996).
7. F.F. Grinstein, “Self-induced vortex ring dynamics in subsonic rectangular jets,” *Phys. Fluids* 7, 2519-2521 (1995).
8. L.P. Chua, Y.F. Li, S.C.M. Yu and T. Zhou, “Axis-switching of a square jet,” 14th Australasian Fluid Mechanics Conference, Adelaide University, Adelaide, Australia (2001).

9. S.C.M. Yu, J.J. Ai, L. Gao and A.W.K. Law, "Vortex formation process of a starting square jet," *AIAA J.* 46, 223-231 (2008).
10. G. Sankar, R. Balachandar and R. Cariveau, "Characteristics of a three-dimensional square jet in the vicinity of a free surface," *J. Hydraul. Eng.* 135, 989-994 (2009).
11. N. Chen and H. Yu, "Mechanism of axis switching in low aspect-ratio rectangular jets," *Computers and Mathematics with Applications* 67, 437-444 (2014).
12. A. Ghasemi, V. Roussinova and R. Balachandar, "A study in the developing region of the square jet," *J. Turbulence* 14, 1-24 (2013).
13. A. Ghasemi, V. Roussinova, R. Barron and R. Balachandar, "Large-eddy simulation of the near-field vortex dynamics in starting square jet transitioning into steady-state," *Phys. Fluids* 28, 085104, 1-24 (2016).
14. I. Danaila, F. Kaplanski and S. Sazhin, "Modelling of confined vortex rings," *J. Fluid Mech.* 774, 267-297 (2015).
15. I. Danaila, F. Kaplanski and S.S. Sazhin, "A model for confined vortex rings with elliptical-core vorticity distribution," *J. Fluid Mech.* 811, 67-94 (2017).
16. T.T. Lim, T.B. Nickels, and M.S. Chong, "A note on the cause of rebound in the head-on collision of a vortex ring with a wall," *Exp. Fluids* 12, 41-48 (1991).
17. J.D.A. Walker, C.R. Smith, A.W. Cerra and T.L. Doligalski, "The impact of a vortex ring on a wall," *J. Fluid Mech.* 181, 99-140 (1987).
18. T.Y. Chang, J.R. Hertzberg and R.M. Kerr, "Three-dimensional vortex/wall interaction: entrainment in numerical simulation and experiment," *Phys. Fluids* 9, 57-66 (1997).
19. R. Sooraj and A. Sameen, "Effect of confinement on the decay of vortex rings," *Phys. Scr.* 94, 084001-1-084001-6 (2019).
20. D. Rockwell and E. Naudascher, "Self-sustained oscillations of impinging free shear layers," *Ann. Rev. Fluid Mech.* 11, 67-94 (1979).
21. D. Rockwell, "Oscillations of impinging shear layers," *AIAA J.* 21, 645-664 (1983).
22. M. Gebert, M.R. Davidson and M.J. Rudman, "Computed oscillations of a confined submerged liquid jet," *Appl. Math. Modelling* 22, 843-850 (1998).
23. N.J. Lawson, "Self-sustained oscillation of a submerged jet in a thin rectangular cavity," *J. Fluids and Structures* 15, 59-81 (2001).

24. B.W. Righolt, S. Kenjereš, R. Kalter, M.J. Tummers and C.R. Kleijn, “Dynamics of an oscillating turbulent jet in a confined cavity,” *Phys. Fluids* 27, 095107, 1-13 (2014).
25. R. Kalter, M.J. Tummers, S. Kenjereš, B.W. Righolt and C.R. Kleijn, “Effects of electromagnetic forcing on self-sustained jet oscillations,” *Phys. Fluids* 26, 06510-1-06510-18 (2014).
26. R. Kalter, M.J. Tummers, S. Kenjereš, B.W. Righolt and C.R. Kleijn, “Electromagnetic flow control of a bifurcated jet in a rectangular cavity,” *Int. J. Heat and Fluid Flow* 47, 113–122 (2014).
27. N.J. Lawson, M.P. Arrudab and M.R. Davidson, “Control of a submerged jet in a thin rectangular cavity,” *J. Fluids and Structures* 20, 1025–1042 (2005).
28. N. Bensider, A. Mataoui and M. Aksouh, “Control of self-sustained jet oscillations in a 3D thin rectangular cavity,” *J. Chem. Eng. Res. and Des.* 117, 533–541 (2017).
29. A. Mataoui, R. Schiestel and A. Salem, “Flow regimes of interaction of a turbulent plane jet into a rectangular cavity: Experimental approach and numerical modelling,” *J. Flow Turbul. Combust.* 67, 267–304 (2001).
30. A. Mataoui R. Schiestel and A. Salem, “Study of the oscillatory regime of a turbulent plane jet impinging in a rectangular cavity,” *J. Appl. Math. Modelling* 27, 89–114 (2003).
31. STAR-CCM+, User Guide, Version 13.06, Siemens, Munich, Germany (2018).
32. K. Hoffmann and S.T. Chiang, “Computational Fluid Dynamics,” Vol. 3, 4th Edition, Engineering Education System, Wichita, Kansas, USA (2000).
33. B.E. Launder, G.J. Reece and W. Rodi, “Progress in the development of a Reynolds-stress turbulence closure,” *J. Fluid Mech.* 68, 537–566 (1975).
34. J.M.J. den Toonder and F.T.M. Nieuwstadt, “Reynolds number effects in a turbulent pipe flow for low to moderate Re ,” *Phys. Fluids* 9, 3398–3409 (1997).
35. L.C. Hoagland, “Fully developed turbulent flow in straight rectangular ducts - secondary flow, its cause and effect on the primary flow,” Ph.D. Thesis, Massachusetts Institute of Technology (1960).
36. B.P. Eppsy, “Review of vortex identification methods”, 55th AIAA Aerospace Sciences, Grapevine, Texas (2017).
37. J. Jeong and F. Hussain, “On the identification of a vortex,” *J. Fluid Mech.* 285, 69-94 (1995).

38. C. Anghan, S. Dave, S. Saincher and J. Banerjee, “Direct numerical simulation of transitional and turbulent round jets: Evolution of vortical structures and turbulence budget,” *Phys. Fluids* 31, 065105, 1-24 (2019).
39. D. Margerit and J.-P. Brancher, “Asymptotic expansions of the Biot-Savart law for a slender vortex with core variation,” *J. Eng. Math.* 40, 297–313 (2001).
40. G. Xu and R.A. Antonia, “Effect of different initial conditions on a turbulent round free jet,” *J. Exp. Fluids* 33, 677–683 (2002).

Chapter 4. Characteristics of self-oscillating twin jets

4.1 Summary

This study is focused on the behaviour of self-oscillating twin jets emanating from round and square cross-section nozzles into a narrow cavity. Computational fluid dynamics simulations are carried out in a confined rectangular cavity using the Reynolds stress turbulence model. Flow field characteristics are evaluated at nozzle spacing-to-diameter ratios (S/d) of 2, 3, 4, 5, at a jet Reynolds number of 27,000 based on nozzle exit velocity and diameter (d). Effects of nozzle spacing on the frequency of oscillation, mean velocity, vortex structure and turbulence features are examined. For S/d up to four, the two jets merge downstream and oscillate as an equivalent single jet. At larger spacing, the two jets do not merge but oscillate separately between the sidewalls and cavity centerline. Comparison of round and square twin jets demonstrates that the nozzle shape does not significantly affect the jet decay. The turbulence intensity of twin jets shows higher values at the center of the cavity for $S/d < 5$, and around the centerline of each jet for $S/d = 5$. With increasing nozzle spacing, the Reynolds shear stress demonstrates that mixing increases in the inner shear layer region and the Reynolds shear stress values for $S/d < 5$ are lower than for $S/d = 5$. Twin oscillating jets produce higher spread and turbulence intensity over a wider area which may be beneficial for cooling of hot devices in industrial applications.

4.2 Introduction

Multiple jet flow configurations can be found in many applications including cooling, heating, air conditioning, water and wastewater treatment. The interaction between two or more jets creates a complicated flow field. A simple twin jet configuration is comprised of two parallel jets issuing from nozzles with the same diameter (d) and at a specified spacing (S) between them. The general features of twin free jets are illustrated schematically in Fig. 4.1. During the initial jet expansion phase, the inner shear layers spread towards each other and merge at what is known as the merging point (X_{mp}). The region between the nozzle exit and the merging point is defined as the converging region. Following merging, the two jets continue to spread and are completely intertwined beyond the combining point (X_{cp}), creating a single jet. The region between the merging and combining points is referred to as the merging region, and the combined region starts downstream of X_{cp} , as shown in Fig. 4.1.

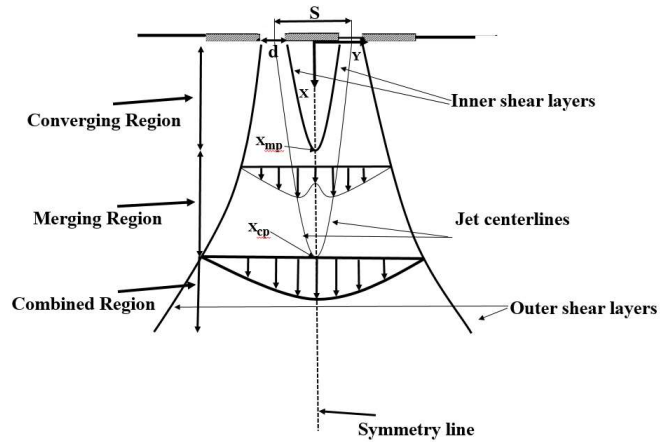


Fig. 4.1 Schematic of twin free jets configuration (adapted from Laban et al.¹¹)

Many researchers have carried out experimental investigations and, to a lesser extent, numerical simulations on non-oscillating submerged twin jets, but only a few have considered self-oscillating twin jets. Some of the studies related to the present research are summarized in Table 4.1, including some of the key contributions to the characterization the flow fields for plane, round and non-circular jet configurations.

Table 4.1 Summary of literature on twin jets

Author	Technique	Re	Jet type	S/d	X_{mp}/d
Tanaka ^{1,2}	HWA	4300 - 9000	Plane	8.5 - 25	<ul style="list-style-type: none"> · $5.06(S/d)^{0.27}$ for $S/d < 16$ · $0.68(S/d)$ for $S/d \geq 16$
Lin & Sheu ³	HWA	4000 - 9000	Plane	30, 40	· $18.7+0.48(S/d)$ for $S/d > 30$
Anderson & Spall ⁴	HWA, CFD	6000	Plane	9, 13, 18	· ~ 10,14,18
Nasr & Lai ⁵	LDA	8300 - 19800	Plane	4.25	· ~ 4
Lee & Hassan ⁶	PIV	4,900	Plane	3	<ul style="list-style-type: none"> · $0.07(S/d)^{3.25}$ for $S/d < 3$ · $1.15(S/d) - 0.23$ for $3 \leq S/d < 10$
Zang & New ⁷	PIV	3300	Plane	1.5, 2, 3	<ul style="list-style-type: none"> · < 2 for $S/d = 1.5$ · ~ 3 for $S/d = 2$ · > 4 and < 6 for $S/d = 3$
Okamoto & Yagita ⁸	Pitot tube	2300	Round	5, 8	· ~ 4, 12.4
Harima et al. ^{9,10}	HWA	25000	Round	2, 4, 8	· ~ 2, 9, 19
Laban et al. ¹¹	PIV	10000	Round	3-7	· ~ 5 - 18
Naseri Oskouie et al. ¹²	PIV	10000	Rectangular	2-7	· ~ 1.5 - 11

Essel & Tachie ¹³	PIV	5000	Round offset	2; Offset distance = 1d, 2d, 4d	· ~ 2
Rahman & Tachie ¹⁴	PIV	2000 -12000	Round offset	2.6; Offset distance = 2d	· ~ 1.1 - 1.6
Greco et al. ^{15, 16}	PIV	6700	OR	1.1, 3, 5	· not reported

HWA: Hot wire anemometry, CFD: Computational Fluid Dynamics, LDA: Laser Doppler anemometry, PIV: Particle image velocimetry, OR: Oscillating round, OS: Oscillating square

Tanaka¹ examined the structure of the twin plane jets, focusing on the converging and merging regions to show the effects of nozzle spacing ratio (S/d , see Fig. 4.1) on velocity and static pressure at different Reynolds numbers. The author demonstrated that stagnation occurs at X_{mp} and there is a linear relationship between the nozzle spacing and the merging point distance from the nozzle exit for $S/d \geq 16$. In another study, Tanaka² investigated the effects of nozzle spacing ratio, focusing on the combined region ($X/d \sim 30-100$). The results indicated that the Reynolds number does not have much effect on the symmetry line maximum pressure point and the maximum value of the mean streamwise velocity. The comparison of single and twin jets showed a higher decay rate for the twin jets, and the decay rate difference increased in the combined region at higher nozzle spacings. The results revealed that the velocity profiles of the combined jet are similar at various nozzle spacings. Furthermore, the spread of the combined jet is linear and increases at higher nozzle spacing with a higher rate compared to a single jet. Lin and Sheu³ studied two plane parallel air jets at large nozzle spacings ($S/d = 30, 40$). They demonstrated that the nozzle spacing and merging point location have a linear correlation which is in agreement with the results of Tanaka¹. Furthermore, their results illustrated that the centerline velocity decay is proportional to $(S/d)^{0.5}$ in the combined region, which is also consistent with Tanaka². They also showed that the velocity decay occurs at a lower rate in the combined region compared to the converging region. The outer shear layer spread rates of twin jets are greater than the inner shear layer, facilitated by a higher entrainment of external fluid. Also, the spread rate in the converging region increases more rapidly compared to that in the combined region. Anderson and Spall⁴ investigated plane twin jets experimentally and numerically. The experiments were conducted using a hot-wire anemometer and the Reynolds stress and $k-\epsilon$ turbulence models were used for the numerical simulations. Their simulations accurately predicted the location of the merging and combining points but showed a narrower jet width compared to the experimental results. This difference may be due to sensitivity

of the simulation to inlet boundary conditions which affects the entrainment into the jet. Nasr and Lai⁵ experimentally investigated the effects of Reynolds number on the mean flow properties of twin plane jets at $S/d = 4.25$. They determined a critical Reynolds number ($Re_{critical}$) beyond which the mean streamwise velocity distribution does not depend on Re . The results showed that at $Re = Re_{critical}$ the velocity of the single jet at the centerline has a higher value compared to that of the twin jets before the combining point. However, after the combining point the centerline velocity of the twin jets is higher. They also demonstrated that the turbulent intensity peak value is smaller in the inner shear layer compared to the outer shear layer. Lee and Hassan⁶ investigated the flow field around the merging point of twin parallel plane jets and proposed a non-linear correlation between X_{mp} and nozzle spacing ratio for $S/d < 3$, and a linear correlation for $S/d \geq 3$. Their results showed that the converging region length is 1.15 times the nozzle spacing for $S/d \geq 3$. They used proper orthogonal decomposition (POD) to analyze the vortex structure in the converging region near the merging point. Using time-resolved PIV at low Reynolds number, Zang and New⁷ observed an oscillatory counter-rotating flow, like that behind a bluff body, in the inner shear layer region. They also found that an increase of the nozzle spacing leads to a twin jet dominant frequency that is closer to that of a single jet.

Using free round jets, Okamoto and Yagita⁸ established that after the streamwise distance of $X/d = 17.5$ for $S/d = 5$ and $X/d = 20$ for $S/d = 8$, the twin-jet configuration centerline velocity decayed at a higher rate ($\sim 22\%$) compared to a single jet. Using a velocity threshold of 10% of the centerline velocity to define the spread of the twin jets, they showed that the spread rate of the twin jets is higher than a single jet in the inner shear layer region and lower at the outer shear layer region. Harima et al.^{9,10} also confirmed that the locations of merging and combining points increase linearly as a function of nozzle spacing. Also, the merging of the jets, which occurs earlier at lower nozzle spacing, causes a higher mean velocity and turbulent intensity at the symmetry line. Their results demonstrated that there is no dependency of the centerline streamwise turbulent intensity peaks on S/d . Furthermore, entrainment is reduced at lower nozzle spacing, resulting in a lower decay rate in the combined region. Laban et al.¹¹ used PIV to carry out a comprehensive study on the effects of nozzle spacing on velocity and high-order turbulence characteristics of single and twin round jets for $3 \leq S/d \leq 7$ and Reynolds number of 10,000. They reported that a decrease in the nozzle spacing increases the growth of the inner shear layers and the turbulence intensity at the symmetry plane. As expected, at the lower nozzle spacing, the velocity decay rate of the jet core

decreased due to lower entrainment in the inner shear layer region. Their comparison of single and twin jets turbulence characteristics demonstrated that the decay and spread rates of the single and twin jets were nearly the same. Furthermore, the turbulence intensity along the centerline of twin jets increased to an asymptotic value which was higher than the single jet value. Naseri Oskouie et al.¹² studied the characteristics of twin rectangular jets (at a low aspect ratio of 2) at various nozzle spacing ratios ($2 \leq S/d \leq 7$) and confirmed the linear correlation between merging and combining point locations and nozzle spacing. Their results demonstrated that increasing the nozzle spacing increases the decay and spread rates and decreases the distance between the combining point and the location where the Reynolds shear stress is self-similar. Their comparison of round and rectangular nozzles showed earlier converging and combining points for the rectangular nozzles.

Essel and Tachie¹³ studied the effects of an offset ratio and confinement (free surface or solid wall) on the flow features. The twin jets were confined only on one side, while the opposite side was maintained at a distance far from the jets. Their results showed that decreasing the offset ratio increased the combining point distance. They reported that this distance was longer when the flow was confined by a wall compared to a free surface confinement. Furthermore, the turbulence intensity and Reynolds stresses were dampened more near the wall confinement and the turbulence intensity increased at the lower offset ratio. Rahman and Tachie¹⁴ investigated the effects of Re on flow characteristics of single and twin round jets with a free surface using PIV measurements with Reynolds number between 2,000 - 12,000. They showed that the Reynolds number does not have much effect on the merging point location, but that the free surface attachment length of both single and twin jets was more sensitive for $Re < 3,900$ and independent at higher Re values

There are a limited number of studies on oscillating twin jets. Greco et al.^{15,16} studied the flow field of twin round synthetic oscillating jets having a phase shift of 180° . At $S/d = 1.1$, due to higher interaction between the two jets, a double vortex ring was visualized which generated higher axial velocity and lower jet width. Also, they found that twin jets with $S/d = 3$ and 5 show the same behavior as a single jet and the twin synthetic jets behave like two separated synthetic jets.

As seen from above, most previous research deals with either free or plane jets. The current study is the first CFD study of twin self-oscillating jets in a confined cavity. Although some experimental research on free and semi-confined twin jets and oscillating synthetic jets has been reported in the literature, there is a lack of understanding of the flow characteristics of self-oscillating twin jets in a confined cavity, wherein the oscillations are self-driven by the Coanda effect¹⁷⁻¹⁸. The motivation

of this study is to evaluate the influence of geometry and flow parameters which are critical to identifying potential regions with higher heat transfer rates that can be exploited in industrial applications. These parameters include nozzle shape, spacing between the nozzles, growth and transport of vortices in the cavity and turbulence characteristics in terms of turbulence intensities and Reynolds shear stresses. This study is an extension of our previous work on single self-oscillating jets¹⁸.

4.3 Numerical modelling and methodology

The present study involves the use of two identical jets simultaneously flowing into a narrow rectangular cavity. The cavity confines the jets which interacts with two close walls (referred to as confinement walls) and two sidewalls which are farther apart, as illustrated in Fig. 4.2. The cavity has dimensions 250 mm x 585 mm x 40 mm. Both round (Fig. 4.2(a)) and square cross-section (Fig. 4.2(b)) nozzles are used, which protrude 95 mm into the cavity and have a hydraulic diameter $d = 14$ mm and a wall thickness of 3 mm. These dimensions are identical to those in the experimental work of Lawson et al.¹⁹ and were chosen to facilitate validation of the numerical model. The spacing (S) separating the twin nozzles is varied from $2d$ to $5d$. The fluid (water) is assumed to be incompressible with a density (ρ) of 997 kg/m^3 and dynamic viscosity (μ) of $9.7 \times 10^{-4} \text{ kg/(m.s)}$. All solid walls are assumed to be smooth.

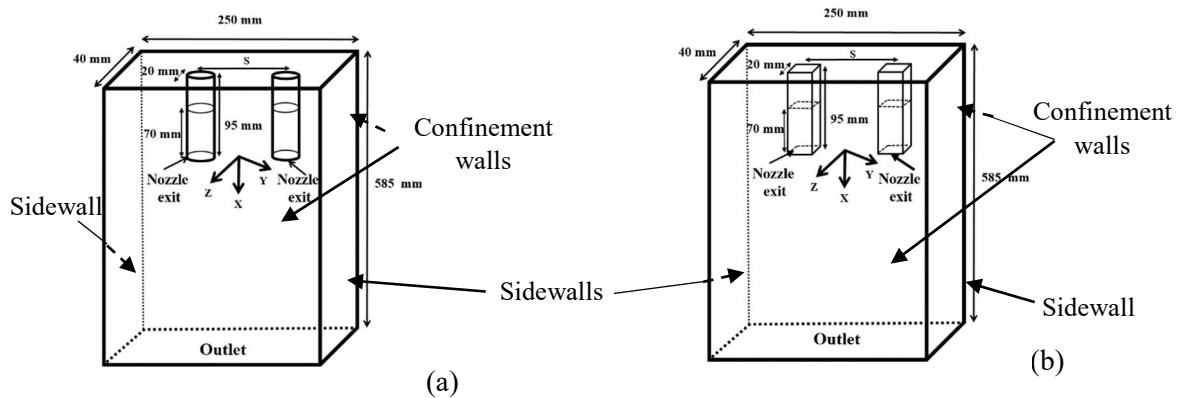


Fig. 4.2 Cavity configurations (not to scale): (a) twin round jets, (b) twin square jets

The turbulent flow in the cavity is modeled using the Reynolds-Averaged Navier-Stokes (RANS) equations governing unsteady incompressible flow, expressed in tensorial notation as²⁰

$$\frac{\partial U_j}{\partial X_j} = 0 \quad (1)$$

$$\rho \left(\frac{\partial U_i}{\partial t} + U_j \frac{\partial U_i}{\partial X_j} \right) = -\frac{\partial P}{\partial X_i} + \frac{\partial}{\partial X_j} \left[\mu \frac{\partial U_i}{\partial X_j} - \overline{\rho u'_i u'_j} \right] \quad (2)$$

where $i, j = 1, 2, 3$, X_i are the Cartesian coordinates X, Y, Z , t is the time, U_i and u'_i are the mean and fluctuating velocity components, respectively, P is the pressure, ρ is the density, μ is the dynamic viscosity and the overbar denotes time-averaged values. Using the Boussinesq assumption, the components of the Reynolds stress tensor are given by²¹

$$\overline{\rho u'_i u'_j} = \frac{2}{3} \rho k \delta_{ij} - \mu_t \left(\frac{\partial U_i}{\partial X_j} + \frac{\partial U_j}{\partial X_i} \right) \quad (3)$$

where k is the turbulent kinetic energy, μ_t is referred to as turbulent viscosity and δ_{ij} is the Kronecker delta. Based on previous validations^{18,22}, the turbulence is modeled using the unsteady Elliptic Blending Reynolds Stress Model (EBRSM)²¹, which consists of transport equations for each of the stress tensor components. The Reynolds stress equations are

$$\left(\frac{\partial \overline{u'_i u'_j}}{\partial t} + U_k \frac{\partial \overline{u'_i u'_j}}{\partial X_k} \right) = P_{ij} - \epsilon_{ij} + \pi_{ij} - \left(\frac{\partial \overline{u'_i u'_j u'_k}}{\partial X_k} \right) + \frac{\mu}{\rho} \left(\frac{\partial^2 \overline{u'_i u'_j}}{\partial X_k^2} \right) \quad (4)$$

where the production, dissipation and velocity–pressure gradient tensors are defined as

$$P_{ij} = -\overline{(u'_k u'_i \frac{\partial U_j}{\partial X_k} + u'_k u'_j \frac{\partial U_i}{\partial X_k})} \quad (5)$$

$$\epsilon_{ij} = 2 \frac{\mu}{\rho} \left(\frac{\partial u'_i}{\partial X_k} \frac{\partial u'_j}{\partial X_k} \right) \quad (6)$$

$$\pi_{ij} = -\frac{1}{\rho} u'_j \frac{\partial P'}{\partial X_i} + u'_i \frac{\partial P'}{\partial X_j}. \quad (7)$$

The terms $\left(\frac{\overline{\partial u'_i u'_j u'_k}}{\partial X_k}\right)$ and $\left(\frac{\partial^2 \overline{u'_i u'_j}}{\partial X_k^2}\right)$ are the turbulent transport and viscous diffusion tensors, respectively.

The governing equations (1), (2) and (4) are discretized by the finite volume method and solved using the commercial software STAR-CCM+²³ with a second-order upwind scheme for convection terms and a second-order implicit scheme for time discretization. The SIMPLE algorithm is used for pressure-velocity coupling.

All walls of the confinement cavity are treated as no-slip boundaries and an outflow condition is applied at the outlet of the computational domain. To ensure fully developed flow conditions at the entrance to the cavity, separate RANS simulations were conducted for the turbulent flow in a round pipe and a square duct with hydraulic diameter $d = 14$ mm. The resulting fully developed nozzle exit profiles were mapped as inlet conditions for the simulations in the confinement cavity and applied inside the nozzle at 70 mm from the exit to allow for the possibility of some backflow into the nozzle. The Reynolds number for these simulations was 27,000 based on the nozzle hydraulic diameter, giving the average exit velocity $U_e = 1.875$ m/s.

The computational domain (i.e., confinement cavity) is discretized using a hexahedral mesh. The domain and mesh in two vertical cross-sections through the nozzles are illustrated in Fig. 4.3. The multiblock hexahedral mesh used in this study is comprised of three different regions. A fine mesh (0.4 mm) covers the central core region of the jet, while an intermediate mesh (1.6 mm) is used in the jet expansion region and a coarser mesh (2.4 mm) is used in the outer regions of the cavity. An adequate cell size was determined by performing the simulations on several mesh sizes for the case $S/d = 2$. Several time steps were also considered to ensure time accuracy and numerical stability. The grid and time step independence were established by comparing results using 6, 9 and 14 million cells, and time steps of 0.1 ms, 0.05 ms and 0.01 ms. Based on Figs. 4.4 and 4.5 shown for the twin square oscillating jet, a mesh size of 6 million cells and time step size of 0.05 ms were selected for subsequent simulations. In these figures, U is the streamwise velocity, U_e is the average nozzle exit velocity and $t^* = t \times f$ is a nondimensional time, where f is the oscillating jet frequency. For the 6 million cell mesh, the dimensionless distance of the first cell from the walls ($Y^+ = Y u_\tau \rho / \mu$) is less than one, where u_τ is friction velocity defined as $u_\tau = (\tau_w / \rho)^{0.5}$ and τ_w is wall shear stress. The time step of 0.05 ms ensures that the Courant number is less than one

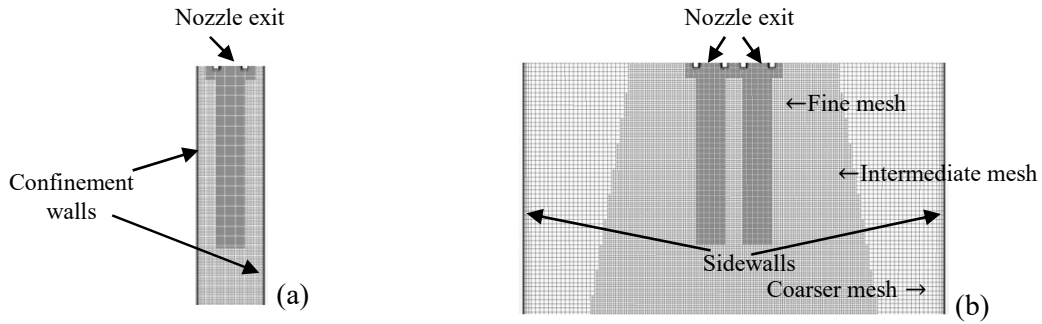


Fig. 4.3 Cross-sections of the mesh in the twin square jets domain: (a) XZ plane, (b) XY plane

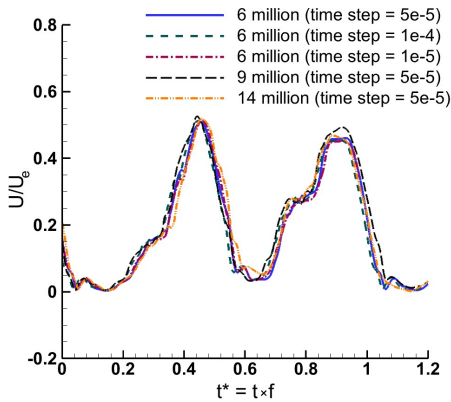


Fig. 4.4(a) Time series of streamwise velocity in a square jet at point (14.0d, 0.0, 0.0)

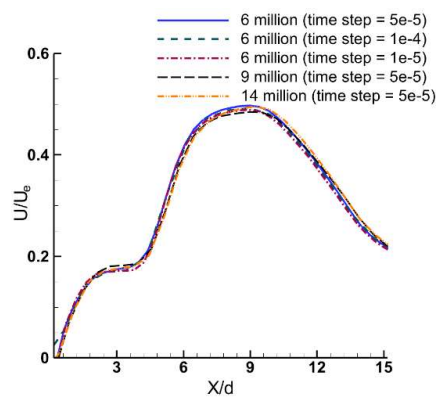


Fig. 4.4(b) Nondimensional streamwise velocity along the symmetry line

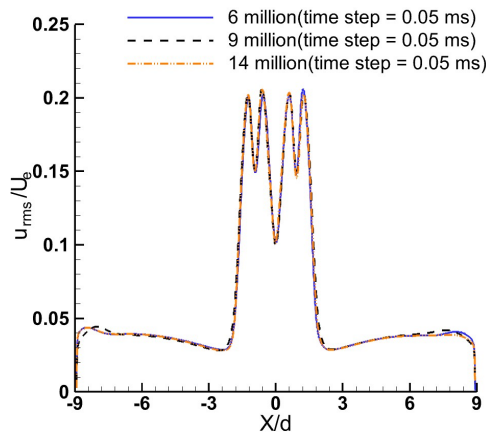


Fig.4.5 Non-dimensional streamwise turbulence intensity at X = 5d

The validation was carried out based on the guidelines recommended by the American Institute of Aeronautics and Astronautics (AIAA) for validation of CFD results²⁴. The CFD results must be validated with several benchmark cases to ensure that the physics of the flow field is properly captured. As a first step, the fully developed flow at the nozzle exit was validated with experimental results of den Toonder and Nieuwstadt²⁵ for pipe flow and Hoagland²⁶ for a square

duct flow. In the second step, the CFD results were validated with the experimental data of Lawson et al.¹⁹ as reported in our earlier study on single round and square confined oscillating jets¹⁸. The predicted streamwise velocity along the centerline and at the streamwise distance of $X = 1.35d$ showed good agreement with the results of Lawson et al.¹⁹ The third step involved validation of turbulence characteristics. Since Lawson et al.¹⁹ did not report turbulence intensity measurements, the simulation results were compared with that of Bensider et al.²² for streamwise and spanwise turbulence intensities. Comparison of the Reynolds stresses $\overline{\rho u' u'}$ and $\overline{\rho v' v'}$, which are computed as primary quantities in RSM, demonstrated satisfactory agreement. Additional validation was considered by comparing the results for a square jet simulation with the experimental results of Kalter et al.²⁷ The jet oscillation frequency evaluation of the velocity-time signal based on FFT at point (25.0d, 0.0, 0.0) was found to be in excellent agreement with the experiment. Furthermore, the CFD results for the streamwise velocity at two different streamwise distance ($X = 8d$ and $X = 18d$) accurately followed the trend of the experimental results (for more details see¹⁸). For brevity, the validation results are not repeated here.

4.4 Results and discussion

In this section, the effects of nozzle spacing on the velocity, vortex structures, turbulence characteristics and oscillation frequency are discussed for both the oscillating round (OR) and oscillating square (OS) twin jets.

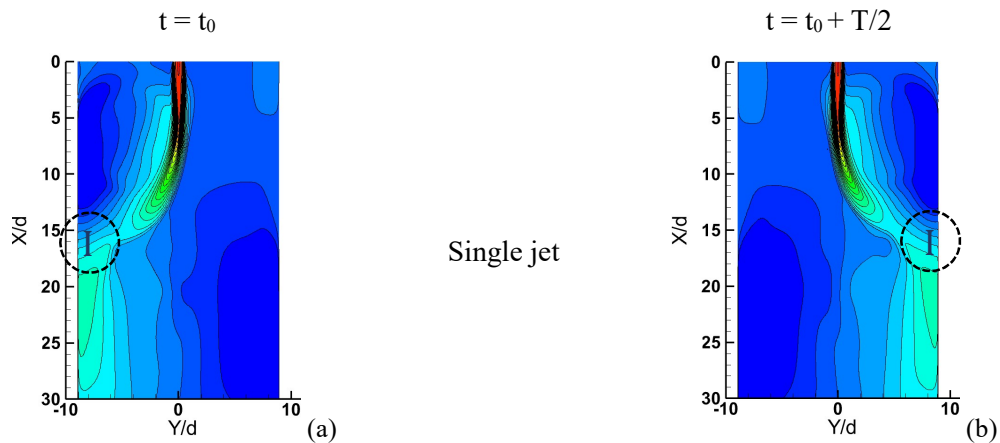
4.4.1. Oscillation mechanism of single and twin jets

The left column in Figure 4.6 shows the flow fields when the single and twin square jets are in their maximum left position at some time $t = t_0$ during the oscillation process. The flow fields are shown in the maximum right position (right column) of the jet(s) at $t = t_0 + T/2$, where T is the period of oscillation. One should note that the values of t_0 and T (see Table 2) are case dependent. For a single nozzle (Figs. 4.6(a,b)), the jet initially attaches to one sidewall of the cavity due to the Coanda effect. As illustrated in Mosavati et al.¹⁸, the interaction between the flow features in the cavity generates self-sustained oscillation of the jet. In the case of twin jets with a small spacing, entrainment between the two jets creates a low-pressure region between them, resulting in deflection towards each other². As illustrated in Figs. 4.6(c,d) for $S/d = 2$, the pair of jets merge and the oscillation mechanism is similar to that of a single jet. This aspect is better described in Fig. 4.7, which shows the Z -component of the instantaneous vorticity field with arrows

superimposed to indicate direction of flow. In Fig. 4.7(a), at time $t = t_0$, the combined jet is deflected to the left sidewall and three rotating regions are formed (labeled as A, B and C). As the jet impinges on the left sidewall, a large counterclockwise vortex (A) below the impingement point (I) and a clockwise vortex (B) above the impingement point are generated. The high vorticity along the right shear layer (indicated in red) feeds vortex A and the one on the left (blue) feeds vortex B. The corner vortex (C) is formed at the left top corner as the flow is constrained by the top wall. Following impingement on the left wall, the jets commence their movement towards the right wall. The mechanics of this process is similar to that reported earlier for a single oscillating jet¹⁸. The motion of the shear layers towards the right, combined with the physical constraints imposed by the cavity walls, cause vortex A to be squeezed and become smaller (Fig. 4.7(b)). Simultaneously, the flow in the right-half of the cavity is directed upwards which washes out vortex C. As vortex A moves upwards (Fig. 4.7(c)) the flow near the top end is mostly directed to the left, with a small portion directed to the right forming a new vortex C' in the top right corner. A major portion of the flow is directed downwards along the left-hand side of the cavity, facilitating the growth of vortex B as it is transported downwards. Eventually, vortex B occupies most of the bottom half of the cavity and the jet impinges on the right wall at time $t = t_0 + T/2$, as shown in Fig. 4.6(d) and Fig. 4.7. Following impingement on the right wall and due to the prevailing pressure difference, the jets begin their motion towards the left wall. Twin jets with spacing $S/d = 3$ and 4 also merge and exhibit the same oscillatory behavior described above.

For the higher nozzle spacing ($S/d = 5$), the two jets shown in Fig. 4.6(e) oscillate separately without merging. Unlike smaller values of S/d , the jets travel away from each other and eventually the left jet impinges (indicated by I) on the left wall, and simultaneously the right jet impinges on the right wall. At one-half of the oscillation period (Fig. 4.6(f)), the jets approach the middle of the cavity. A more complete evolution of the flow is presented in Fig. 4.8, which shows the instantaneous vorticity field on the plane $Z = 0$ over a typical oscillating period. As shown in Fig. 4.8(a), at $t = t_0$, three vortical regions (A, B, C) are formed on each side of the cavity symmetry plane ($Y = 0$). Vortices B are formed due to the roll up of the two outer shear layers, while vortices A are fed by the inner shear layers. The two A vortices, rotating in opposite directions, push fluid upwards in the region of the symmetry line, while the jets direct fluid downwards. Consequently, a saddle point (S) is formed at the symmetry line in the vicinity of $X/d = 16$. Due to the space available in the bottom half of the cavity, vortices A entrain fluid and grow in size, while the

growth of vortices B are restricted by the side walls. Furthermore, near the side walls in the vicinity $2 < X/d < 4$, high shear regions (red and blue regions) develop between the counter-rotating vortices B and C, which feed the growth of vortices C. On impingement, the inner shear layers begin their journey towards the middle of the cavity. At $t = t_0 + T/8$ (Fig. 4.8(b)), the inner shear layers penetrate further into the cavity and stretch the vortices A vertically, which results in pushing more fluid upwards between the two jets causing the saddle point to move upwards ($\sim X/d = 4$). As vortices A continue to stretch vertically and grow in size, they push more fluid upwards between the two jets and the saddle point gradually disappears (Figs. 4.8(c) and 4.8(d)). This upward flow between the two jets is confined by the top wall and feeds into vortices C. One can note that from $t = t_0$ to $t = t_0 + 3T/8$, the jets move inwards towards each other. The growth of vortices C pushes vortices B downward as the inner shear layers move closer to the symmetry plane. Vortices A occupy the space between $X/d = 20$ and the outlet. At $t = t_0 + 4T/8$ (Fig. 4.8(e)), the inner shear layers get close to each other and begin the process of pushing away from each other towards the side walls. In the next few instances, vortices A become smaller and smaller as they are pushed towards the outlet ($t = t_0 + 6T/8$, Fig. 4.8(g)). As the inner shear layers approach the side walls, they once again begin to roll up and form new vortices (denoted as A') rotating in opposite directions. When $t = t_0 + T$ (Fig. 4.8(i)), the inner shear layers again impinge on the side walls and the flow features are similar to that noted at $t = t_0$ (Fig. 4.8(a)). The oscillations continue with the movement of the jets towards the center of the cavity. It is clear from Fig. 4.7 that at lower values of S/d , the outer shear layers cause the dominant vortices to be formed, whereas in Fig. 4.8, the dominant vortices are associated with the inner shear layer at larger jet spacing.



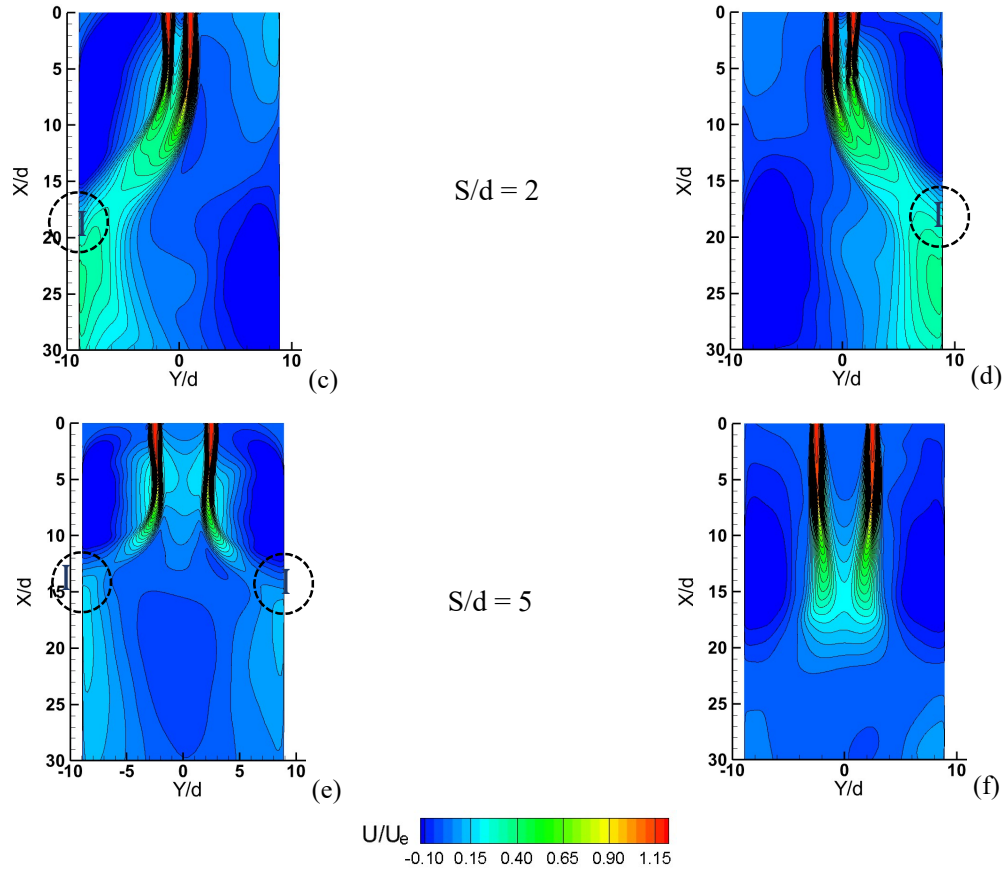


Fig. 4.6 Instantaneous streamwise velocity contours at times t_0 (left column) and $t_0 + T/2$ (half-period; right column): (a,b) single OS jet, (c,d) twin OS jets at $S/d = 2$, (e,f) twin OS jets at $S/d = 5$

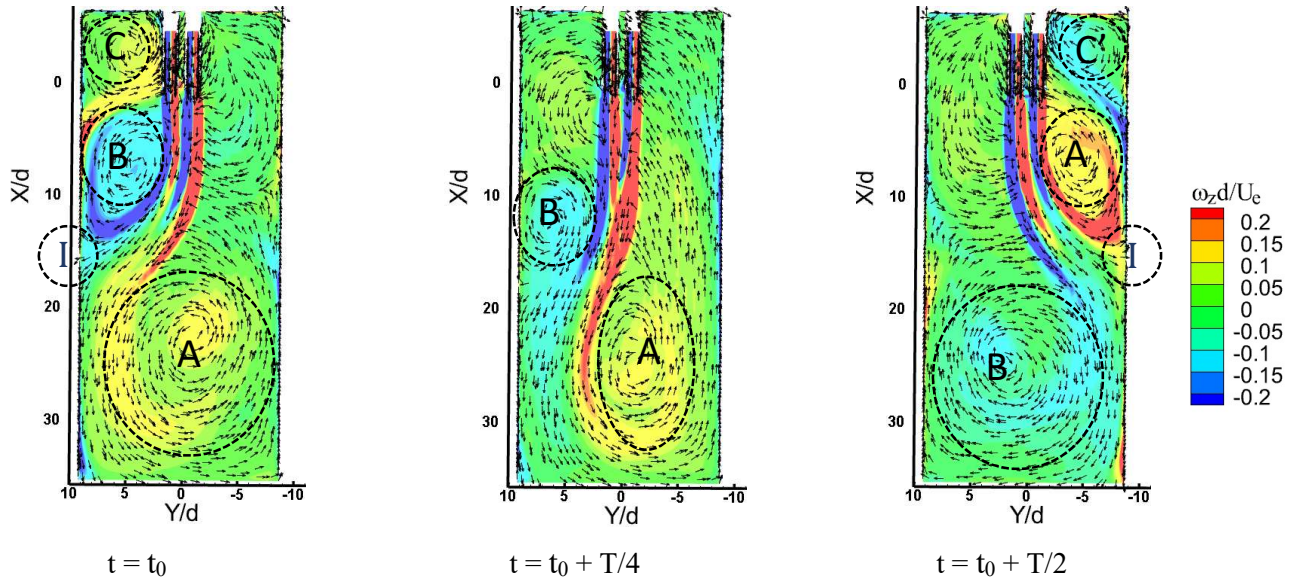
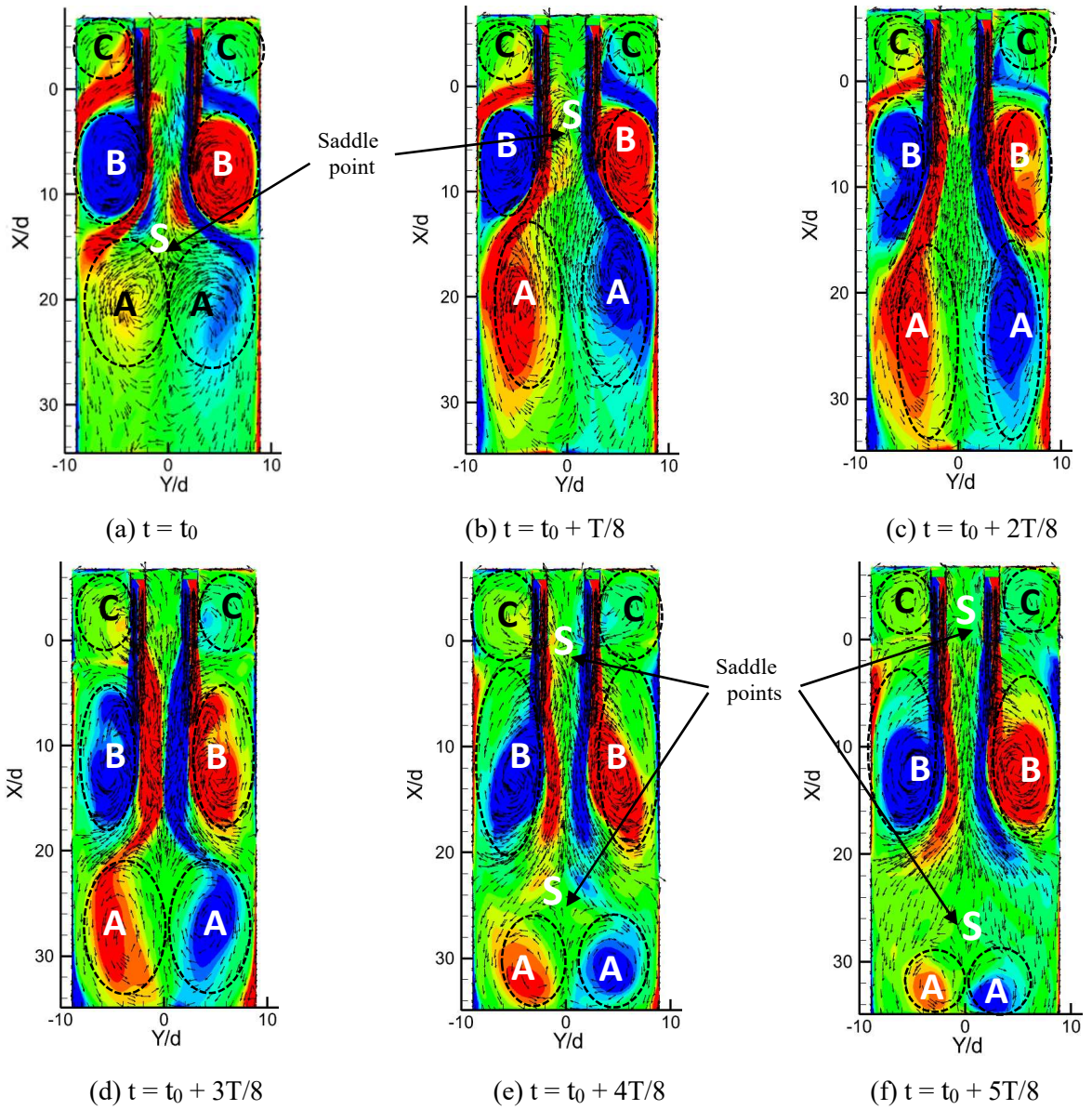


Fig. 4.7 Instantaneous velocity vectors of the OS twin jet ($S/d = 2$), superimposed on the vorticity contours on the plane $Z = 0$, during a half period ($T/2$)



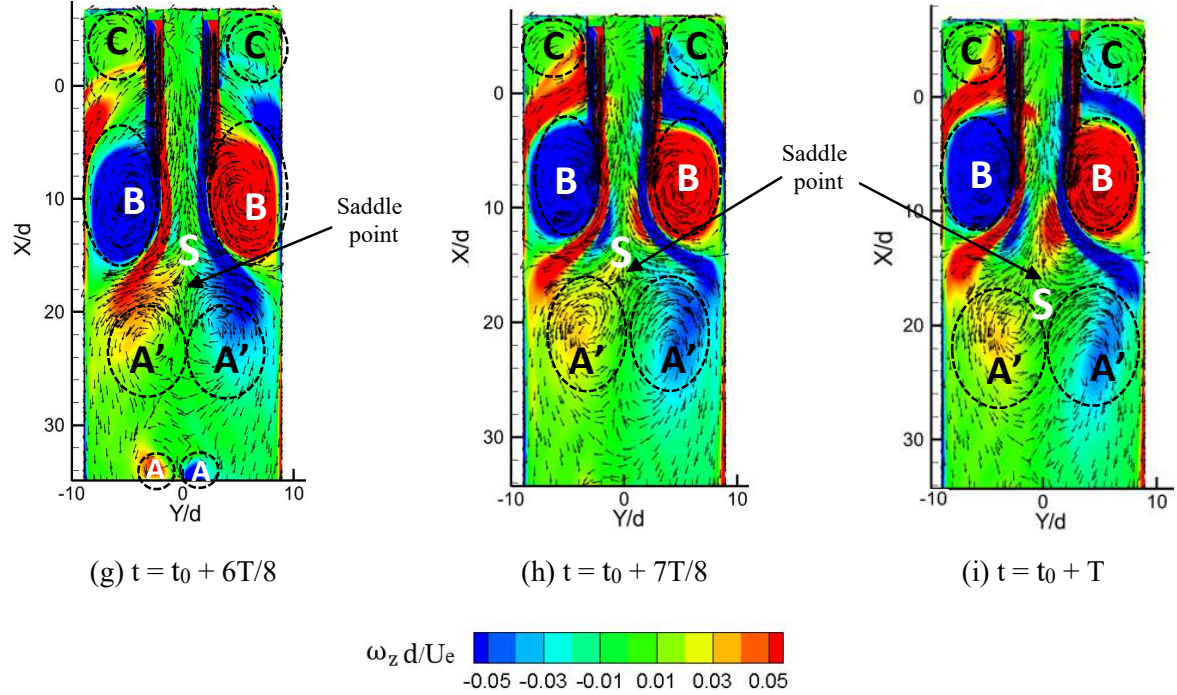


Fig. 4.8 Instantaneous velocity vectors of the OS twin jet ($S/d = 5$), superimposed on the vorticity contours on the plane $Z = 0$, during a period (T); (a – i) correspond to time increments of $T/8$

4.4.2 Effects of jet spacing on jet frequency

The frequency of jet oscillation has an important role in influencing the jet characteristics. The frequency of oscillations was evaluated from Fast Fourier Transform (FFT) of the time series of the jet crossflow velocity at the downstream location ($13.0d, 2.9d, 0.0$). The Strouhal number, St_w , based on cavity width W of 250 mm, jet frequency (f) and average jet exit velocity (U_e) is defined as:

$$St_w = f \times \frac{W}{U_e} \quad (8)$$

and shown in Table 2. The results show that the frequency is not significantly affected by changes in the jet spacing when the nozzles are relatively close together and the value of St_w is about 25 % higher than that of the single oscillating jet. However, as seen in Figs. 4.6(e,f), when $S/d = 5$, the two jets oscillate separately between the wall and center of the cavity, without merging. Hence, the Strouhal number for this case should be based on the half-width ($W/2$) and has a value of 0.014 which is higher than the single jet and slightly lower than the twin merged jets. The square jets have a slightly larger ($\sim 6\%$) St_w than the oscillating round jets for $S/d < 3$. It should be noted that in heat transfer applications, twin jets with a higher nozzle spacing ($S/d = 5$) can remove heat from

hot devices simultaneously on both sides of the cavity, potentially providing for a more uniform cooling.

Table 4.2. Effect of nozzle spacing on the frequency of oscillating round and square twin jets

	Spacing ratio	St_w	
		OR jet	OS jet
Single jet ¹⁸	-	0.012	0.012
Twin jets	S/d = 2	0.015	0.016
	S/d = 3	0.015	0.016
	S/d = 4	0.015	0.015
	S/d = 5	0.014	0.014

4.4.3 Mean velocity decay

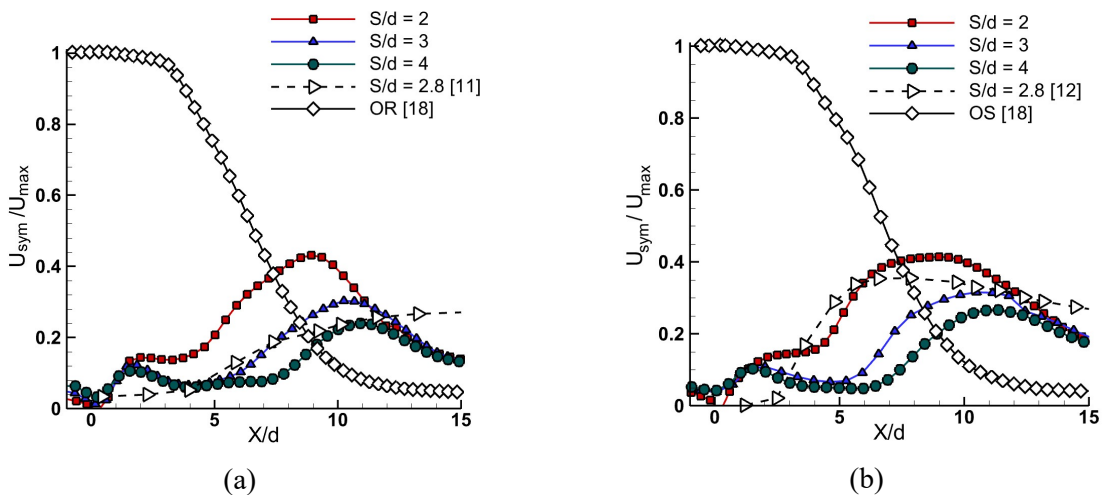
Figure 4.9(a,b) shows the evolution of the streamwise mean velocity along the symmetry line for twin round and square jets at different jet spacing (S/d). One may recall from Fig. 4.1 that the symmetry line refers to the centerline of the cavity, which is located between the two nozzles. To enable direct comparison with the results of earlier studies, U_{max} at the center of the nozzle exit is used as the normalizing variable. Results from Mosavati et. al¹⁸ for a single oscillating jet, Laban et al.¹¹ and Naseri Oskouie et al.¹² for free twin jets are also shown to facilitate discussion.

As seen from Fig. 4.9(a), for a single oscillating round jet, the symmetry line mean velocity, which is also the mean velocity along the nozzle axis, is nearly constant for $X/d < 4$ and can be related to the traditional potential core region seen in jets. For $X/d > 4$, the results indicate a significant jet decay. As noted in our previous study¹⁸, the growth of the outer shear layers is interrupted in the Z-direction in the vicinity of $X/d = 4$ as the jet has by then fully expanded to the confinement walls of the cavity. It should also be noted that the annular shear layers emanating from the nozzle are now converted to inner and outer shear layers travelling through a rectangular cross-section and with different capacities to entrain external fluid. Coupled with oscillations, the expansion characteristics are different from free jets¹⁸.

In both Figs. 4.9(a) and 4.9(b), the present twin jet results show that the symmetry line mean velocity variation is quite different from that of both single OR and OS jets, and twin free jets. The twin oscillating jets display two local peaks, one of which is nearly independent of S/d and located at $X/d \sim 2$. With increasing S/d , the second peak decreases in magnitude but is located farther from the nozzle exit. For non-oscillating twin free jets, the results of Laban et al.¹¹ and Naseri Oskouie

et al.¹² do not indicate the occurrence of the first peak noted in our study. Furthermore, in the twin free jet studies of Laban et al.¹¹ and Naseri Oskouie et al.¹², in the vicinity of $X/D \sim 0$, the symmetry line velocity results start at zero, whereas for the present flow configuration, the symmetry line velocity is influenced by the interaction seen in Fig. 4.7 that keeps the fluid flowing around the nozzles, and up and down inside the cavity as demonstrated earlier.

Meslem et al.²⁸ have suggested that for twin free jets, the merging point can be determined by the location where the cavity symmetry line velocity U_{sym} is 10% of the jet centerline velocity. Laban et al.¹¹ have also identified their merging point using this definition. However, in twin oscillating jets this definition may not be appropriate as the flow physics involves other aspects due to the oscillation and high degree of confinement. A detailed evaluation of the streamwise velocity distribution through the flow cross-section reveals that although there is interaction between the jets, the flow field is quite complex and determination of a definitive merging point is not possible. Figure 4.9(c) shows the variation of U_{sym} with X/d at three time instances within the same period of oscillation for $S/d = 4$. Each curve in the graph refers to a different position of the jets within the cavity. The curve at $t = t_A$ corresponds to the jets being in the extreme right position, the curve at $t = t_A + T/8$ corresponds to a position between the symmetry line and the right cavity wall and the curve at $t = t_A + T/4$ corresponds to the jets being in the mid-cavity region. It is clear that at each position of the jets within the cavity, the distributions are quite distinct. The three distributions show the two peaks, though the first peak is located farther into the cavity when the jet is positioned at the extreme right. Since the instantaneous distribution varies significantly, it may not be meaningful to evaluate a mean merging point for oscillating twin jets.



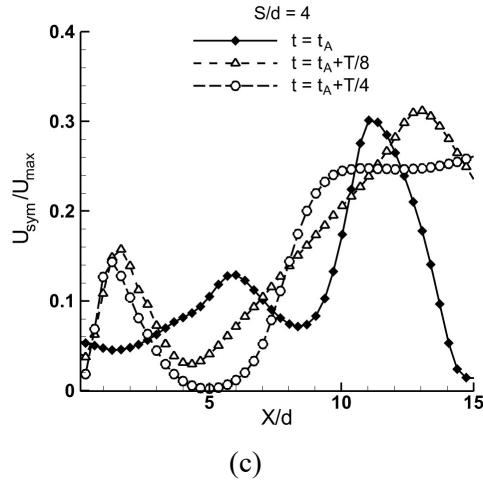


Fig. 4.9 Streamwise velocity profiles of twin jets at the symmetry line: Mean velocity (a) round twin jets, (b) square twin jets; (c) Instantaneous velocity for round twin jets at $S/d = 4$

Figure 4.10(a) shows the mean streamwise velocity of twin oscillating round jets at various distances from the nozzle exit for $S/d = 2$. The velocity distribution is symmetric and one half of the jet is shown. Over the region $0 < X/d < 7$, the peak jet velocity decreases by $\sim 40\%$ due to entrainment of the surrounding fluid. As the jets begin to interact, they can still be individually identified, but the peaks shift towards the line of symmetry as seen at $X/d = 5$ and $X/d = 7$. At $X/d = 9$, the two jets appear to combine and behave like a single jet, with a single peak at the line of symmetry. For convenience, the concept of an “equivalent single jet” is introduced when two jets behave like a single jet. Farther downstream, for $11 < X/d < 13$, the equivalent single jet velocity decays and the maximum velocity at the symmetry line decreases by $\sim 45\%$. As the flow proceeds downstream, the jet oscillation causes the single peak to change into two milder peaks that move towards the sidewalls at $X/d = 15$. These trends are also observed at nozzle spacings of $S/d = 3$ and 4. At the larger nozzle spacing, $S/d = 5$, the two jets can be identified individually. As shown in Fig. 4.10(b), peaks in the velocity profiles for each jet are observed at the nozzle centerline at all downstream distances in the range $1 < X/d < 15$, and the peak value decays as the flow proceeds downstream.

Figure 4.11 shows the mean streamwise velocity of twin oscillating round and square jets at various distances from the nozzle for $S/d = 2$ and 3, and the trend is similar at $S/d = 4$. Beyond $X/d = 11$ these twin jets behave as an equivalent single jet. For $11 < X/d < 15$, the percent of centerline velocity decay of equivalent round jets are $\sim 64\%$, 54% and 46% for $S/d = 2, 3$ and 4, respectively.

Also, the percent of centerline velocity decay of square jets are $\sim 42\%$, 31% and 25% for $S/d = 2$, 3 and 4, respectively. The results show that the equivalent single round jets decay faster than the square jets. Moreover, for $11 < X/d < 15$, the percent of centerline velocity decay of a round jet is 55% for $S/d = 5$ (Fig. 4.10(b)), which is lower than for $S/d = 2$ due to the difference in the oscillation characteristics. At $S/d = 5$, the two jets behave as two single oscillating jets¹⁸. The trend of velocity decay for the round and square oscillating jets are similar at $S/d = 5$. Furthermore, for $11 < X/d < 15$, the percent of centerline velocity decay of the single oscillating¹⁸ jets are $\sim 53\%$ and 56% for the round and square jets, respectively.

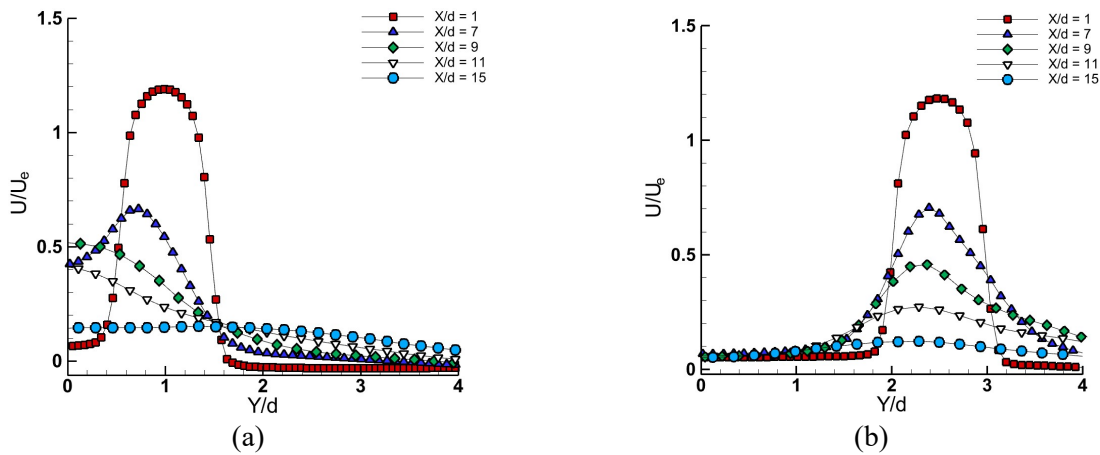


Fig. 4.10 Mean streamwise velocity of twin oscillating round jets: (a) $S/d = 2$ (b) $S/d = 5$

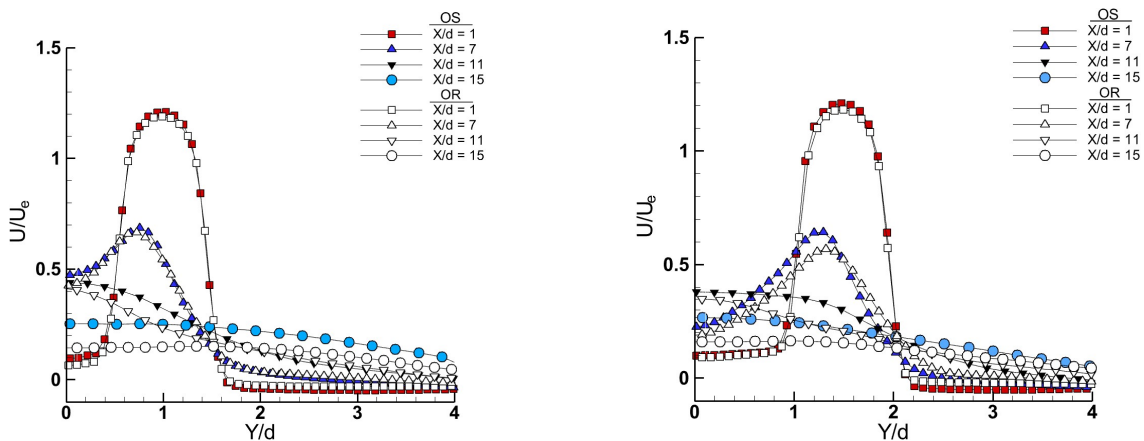


Fig. 4.11 Mean streamwise velocity of oscillating twin round and square jets: (a) $S/d = 2$, (b) $S/d = 3$

In turbulent jets, decay and spread rates are important, and a higher rate of jet decay and spread improves jet mixing due to higher entrainment with the surrounding fluid. However, as seen from the above discussion, the flow physics of the oscillating jets is complex. As illustrated in Fig.

4.9(c), the symmetry line velocity of the jets changes during the oscillation and the decay and spread rates are not straight-forward calculations. The time-averaged results help to understand the trends and provide a qualitative comparison with traditional free jets.

4.4.4. Turbulence characteristics and Reynolds shear stress

The streamwise turbulence intensity u_{rms}/U_e for twin round jets at various axial locations for $S/d = 2$ and 5 are shown in Figs. 4.12(a,b). The streamwise turbulence intensity is symmetric and one half of the jet is shown. Figure 4.12(a) shows that near the nozzle exit ($X/d = 1$), the turbulence intensity profiles exhibit four peaks (two for each jet) in the vicinity of the shear layers due to the high production of turbulence in these regions. During expansion of the jets, the outer shear layers shift inwards and, at $X/d = 9$ the inner shear layer has disappeared and the equivalent single jet is formed. Furthermore, the turbulence intensity at the center of the cavity ($Y = 0$) increases gradually. At $X/d = 11$ and $X/d = 13$, the turbulence intensity has one peak at the center. The turbulence intensity is maximum at $X/d = 11$ which decreases by 25% at $X/d = 13$. Farther downstream, at $X/d = 15$, the turbulence intensity at the center decays by 30% and one peak converts to two mild peaks due to jet oscillation. Twin jets with larger nozzle spacing ($S/d = 3$ and 4) behave similar to the $S/d = 2$ case. Figure 4.12(b) illustrates that twin jets at $S/d = 5$ behave like two separate jets with four peaks (two peaks at the shear layers of each jet) for $X/d < 9$. Moreover, the maximum turbulence intensity at the centerline of each jet increases until $X/d = 9$, where one peak is observed on each side. Further downstream the turbulence intensity decays gradually. The flow oscillation patterns for $S/d = 2$ and $S/d = 5$ are different. Twin jets have a higher turbulence intensity at the center of the cavity for $S/d = 2, 3, 4$, and around the centerline of each jet when $S/d = 5$, which can be exploited in different industrial applications. Furthermore, the results in Fig 4.12(a) demonstrate that the maximum turbulence intensity at the center of cavity for a single jet¹⁸ is 20% higher than the maximum for twin jets at $S/d = 2$.

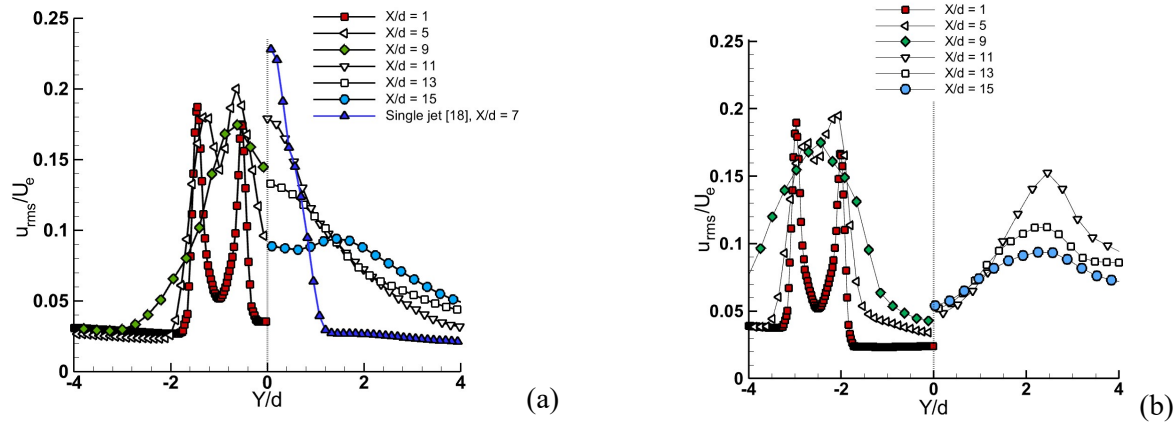


Fig. 4.12 Mean streamwise turbulence intensity of oscillating twin round jets: (a) $S/d = 2$, (b) $S/d = 5$

The normalized Reynolds shear stress ($\overline{u'v'}/U_e^2$) of twin round jets are shown on the $Z = 0$ plane for $S/d = 2$ in Fig. 4.13(a). The normalized Reynolds shear stress is symmetric and one half of the jet is shown. The larger spatial extension of the outer shear layer compared to the inner shear layer promotes greater mixing in the outer region. When the two jets spread, the spanwise development of the jets is inhibited by the presence of the neighboring jet, and the jets cannot develop freely, leading to greater development of the outer shear layer compare to the inner shear layer. Increasing nozzle spacing decreases the interaction between the jets, allowing the jets to develop more in the spanwise direction, increasing the size of the inner shear layer as illustrated in Fig. 4.13(b). The profiles in Fig. 4.13(a) show four peaks (two peaks for each jet) for $1 < X/d < 5$ and, moving downstream at $X/d = 9$, the equivalent single jet shows one peak at each side. Furthermore, the Reynolds shear stress peak values move towards the symmetry line as shown for $X/d = 1$ to 9. Further downstream, for $9 < X/d \leq 15$, the Reynolds stress dissipates and the maximum value decreases. At $S/d = 5$, Fig. 4.13(b) demonstrates that the flow oscillation trend is like a single¹⁸ oscillating jet and the Reynolds shear stress values are higher than for $S/d < 5$ due to higher entrainment of the inner shear layer.

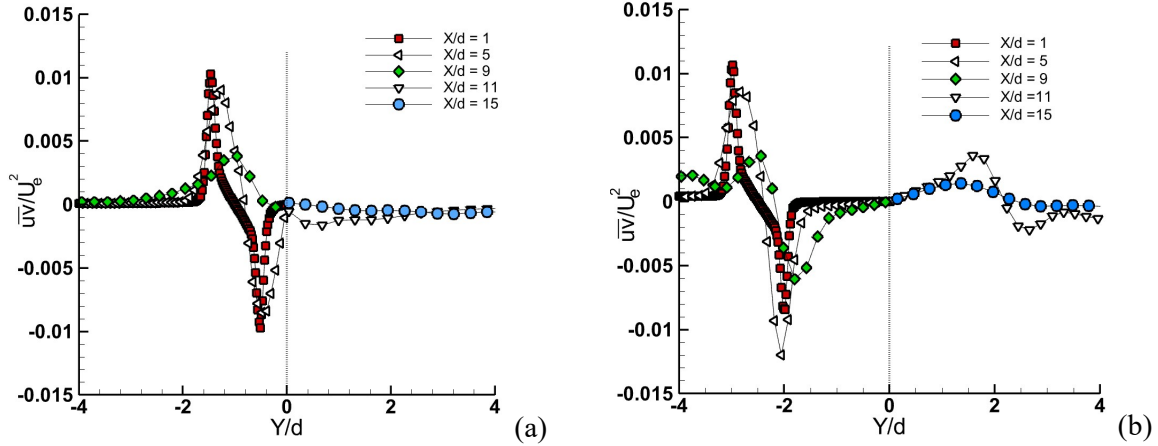


Fig. 4.13 Mean Reynolds shear stress of oscillating twin round jets: (a) $S/d = 2$, (b) $S/d = 5$

4.5 Conclusions

The unsteady Reynolds stress turbulence model is used to investigate twin self-oscillating round and square jets in a rectangular cavity at a Reynolds number of 27,000. The effects of nozzle spacing-to-diameter ratio (S/d) on the jet velocity, vortex structure, turbulence characteristics and oscillation frequency are studied. It is observed that the twin oscillating jets merge for low S/d and the oscillation frequency is not significantly affected by increasing the nozzle spacing. However, for nozzle spacing ratios $S/d = 5$, the two jets do not merge but oscillate separately between the sidewalls and center of the cavity.

The oscillation of the jets is due to the formation of vortices that expand, elongate and contract. For small S/d , the jets merge into an equivalent single jet. As these vortices move inside the cavity, fluid is pushed upward and downward along the sidewalls, deflecting the jet. The twin jets do not merge for larger S/d and, although the vortices continuously deform, they do not travel within the cavity, causing each jet to oscillate between the respective sidewall and the cavity centerline.

Investigation of the streamwise turbulence intensity of twin oscillating jets at different distances from the nozzle exit revealed that at small S/d the turbulence intensity profiles have four peaks in the vicinity of the shear layers. After jet expansion, the inner shear layers disappear and an equivalent single jet is formed. Farther downstream, the turbulence intensity at the center decays and two mild peaks are observed. Moreover, the twin jets have a higher turbulence intensity at the centerline of the cavity for $S/d < 5$, and the turbulence intensity is higher around the centerline of each jet when $S/d = 5$.

The Reynolds shear stress profiles of twin jets demonstrated that for $S/d = 5$, the flow oscillation trend is like two single oscillating jets. Furthermore, the Reynolds shear stress profiles for $S/d < 5$ show lower values compared to $S/d = 5$ due to the lower entrainment of the inner shear layer of $S/d < 5$. These results show that twin oscillating jets provide higher spread and turbulence intensity over a wider area which may be beneficial for cooling of hot devices in industrial applications.

Acknowledgement: This research was made possible by the facilities of the Shared Hierarchical Academic Computing Network (SHARCNET: www.sharcnet.ca) and Compute/Calcul Canada, and funding from the Natural Sciences and Engineering Research Council Discovery Grant program (RGPIN/06768-2016).

Data Availability Statement: Raw data were generated at the University of Windsor CFD Lab facility. Derived data supporting the findings of this study are available from the corresponding author upon reasonable request.

Nomenclature

d	Nozzle diameter
f	Frequency
k	Turbulent kinetic energy ($\text{m}^2 \text{s}^{-2}$)
OR	Oscillating round
OS	Oscillating square
P	Pressure
P_{ij}	Production tensor
St_w	Strouhal number
t	Time (s)
T	Period of oscillations (s)
U	Streamwise mean velocity (m s^{-1})
U_e	Nozzle exit average velocity (m s^{-1})
U_{sym}	Symmetry line velocity (m s^{-1})
U_{max}	Maximum velocity at nozzle exit (m s^{-1})
u', v'	Velocity fluctuations (m s^{-1})
u_{rms}	Streamwise rms velocity value (m s^{-1})
W	Cavity width

X, Y, Z	Cartesian coordinates
X_{mp}	Merging point of twin jets
X_{cp}	Combining point of twin jets
Y^+	Wall normal distance
δ_{ij}	Kronecker delta
ϵ_{ij}	Dissipation tensor
π_{ij}	Velocity–pressure gradient tensor
ρ	Density
μ	Dynamic viscosity
μ_t	Turbulent viscosity
ω_z	Z-component of vorticity

References

1. E. Tanaka, “The interference of two-dimensional parallel jets (1st Report, experiments on dual jet),” *Bull. JSME* 13, 272–280 (1970).
2. E. Tanaka, “The interference of two-dimensional parallel jets (2nd Report, experiments on dual jets),” *Bull. JSME* 17, 920–927 (1974).
3. Y.E. Lin and M.J. Sheu, “Investigation of two plane parallel unventilated jets,” *Exp. Fluids* 10, 17–22 (1990).
4. E.A. Anderson and R.E. Spall, “Experimental and numerical investigation of two-dimensional parallel jets,” *J. Fluids Eng.* 123, 401–406 (2001).
5. A. Nasr and J.C.S. Lai, “Two parallel plane jets: mean flow and effects of acoustic excitation,” *Exp. Fluids* 22, 251–260 (1997).
6. S. Lee and Y.A. Hassan, “Experimental study of flow structures near the merging point of two parallel plane jets using PIV and POD,” *Int. J. Heat Mass Transfer* 116, 871–888 (2017).
7. B. Zang and T.H. New, “On the wake-like vortical arrangement and behavior associated with twin jets in close proximity,” *Exp. Therm. Fluid Sci.* 69, 127–140 (2015).
8. T. Okamoto and M. Yagita, “Interaction of twin turbulent circular jet,” *Bull. JSME* 28, 617–622 (1985).

9. T. Harima, S. Fujita and H. Osaka, "Mixing and diffusion processes of twin circular free jets with various nozzle spacing," *Exp. Heat Transfer, Fluid Mech. Thermodyn.* Edizioni ETS, Pisa, Italy, 1017–1022 (2001).
10. T. Harima, S. Fujita and H. Osaka, "Turbulent properties of twin circular free jets with various nozzle spacing," *Int. Symposium on Engineering Turbulence Modelling and Measurements (ETMM6)*, Sardinia, Italy, 501–510 (2005).
11. A. Laban, S. Aleyasin, M. Tachie and M. Koupriyanov, "Experimental investigation of nozzle spacing effects on characteristics of round twin free jets," *J. Fluids Eng.* 141, 071201(1-11) (2019).
12. R. Naseri Oskouie, M. Tachie and B. Wang, "Effect of nozzle spacing on turbulent interaction of low-aspect-ratio twin rectangular jets," *J. Flow, Turbul. Combust.* 103, 323–344 (2019).
13. E.E. Essel and M. F. Tachie, "Submerged turbulent twin jets interacting with a free surface and a solid wall," *Int. J. Heat Fluid Flow* 71, 27–38 (2018).
14. M.S. Rahman and M.F. Tachie, "Reynolds number effect on flow characteristics of surface single and twin jets," *J. Hydraul. Res.* 57, 808-821 (2018).
15. C.S. Greco, A. Ianiro, T. Astarita and G. Cardone, "On the near field of single and twin circular synthetic air jets," *Int. J. Heat Fluid Flow* 44, 41–55 (2013).
16. C.S. Greco, A. Ianiro and G. Cardone, "Time and phase-averaged heat transfer in single and twin circular synthetic impinging air jets," *Int. J. Heat Mass Transfer* 73, 776–778 (2014).
17. D. Rockwell and E. Naudascher, "Self-sustained oscillations of impinging free shear layers," *Annu. Rev. Fluid Mech.* 11, 67–94 (1979).
18. M. Mosavati, R.M. Barron and R. Balachandar, "Characteristics of self-oscillating jets in a confined cavity," *Phys. Fluids* 32, 115103, 1-17 (2020).
19. N.J. Lawson, "Self-sustained oscillation of a submerged jet in a thin rectangular cavity," *J. Fluids Struct.* 15, 59-81 (2001).
20. K. Hoffmann and S.T. Chiang, "Computational Fluid Dynamics," Vol. 3, 4th Edition (2000), Engineering Education Systems, Wichita, KS, USA.
21. B.E. Launder, G.J. Reece and W. Rodi, "Progress in the development of a Reynolds-stress turbulence closure," *J. Fluid Mech.* 68, 537–566 (1975).

22. N. Bensider, A. Mataoui and M. Aksouh, "Control of self-sustained jet oscillations in a 3D thin rectangular cavity," *J. Chem. Eng. Res. Des.* 117, 533–541 (2017).
23. STAR-CCM+, User Guide, Version 13.06, Siemens, Munich, Germany (2018).
24. AIAA, "Guide for the verification and validation of computational fluid dynamics simulations," AIAA Paper G-077-1998(2002), 2002.
25. J.M.J. den Toonder and F.T.M. Nieuwstadt, "Reynolds number effects in a turbulent pipe flow for low to moderate Re ," *Phys. Fluids* 9, 3398–3409 (1997).
26. L.C. Hoagland, "Fully developed turbulent flow in straight rectangular ducts - secondary flow, its cause and effect on the primary flow," Ph.D. thesis, Massachusetts Institute of Technology (1960).
27. R. Kalter, M.J. Tummers, S. Kenjere, B.W. Righolt and C.R. Kleijn, "Effects of electromagnetic forcing on self-sustained jet oscillations," *Phys. Fluids* 26, 06510, 1-18 (2014).
28. A. Meslem, I. Nastase and F. Allard, "Passive mixing control for innovative air diffusion terminal devices for buildings," *J. Build. Environ.* 45, 2679–2688 (2010).

Chapter 5. Use of self-oscillating jets in cooling applications

5.1 Summary

In the present computational study, a preliminary assessment of self-oscillating jets for use in cooling applications is investigated. The jet exits from a square nozzle into a narrow rectangular cavity at a Reynolds number of 54,000 based on nozzle hydraulic diameter and average jet exit velocity. The heated devices, such as electronic chips, are located externally on the front surface of the cavity. A three-dimensional numerical simulation of the flow is conducted by solving the unsteady Reynolds-Averaged Navier-Stokes (URANS) and energy equations to assess the thermal features of the flow field. The turbulence is modeled using RSM. Furthermore, the cooling performance of a self-oscillating jet is compared with that of a wall jet and a channel flow for the same flow conditions and the same arrangements of the hot devices. To this end, the cooling efficacy of two different arrangements of heated devices is evaluated. The self-oscillating jet provides a higher heat transfer for heated blocks which are located farther from the central region, while the wall jet improves heat transfer around the central region. Self-oscillating jets can improve heat transfer over a larger area when the heated devices are aligned orthogonal to the axis of the nozzle. On a Nusselt number (Nu) comparative basis, the channel flow provides the least desirable heat transfer performance.

5.2 Introduction

Jets are used in many engineering heat transfer applications. Some potential applications include turbine blade surface cooling, oil jet cooling to prevent piston overheating, drying of paper or textiles, and cooling of electronic components. Jets provide a mechanism to improve heat transfer from the hot surfaces during the cooling process. Many cooling systems use impinging jets¹. In some applications, an unsteady oscillating jet can be used, especially when there are geometry constraints. Many studies have been reported for cooling systems using channel flow or jets. Some of the relevant studies are summarized in Table 5.1.

Table 5.1. Summary of literature review

Author	Flow type	Technique	Condition	Schematic of geometry
Xu et al. ²	Channel flow	CFD	$Re_L = UL/\vartheta = 10^4 - 1.5 \times 10^5$ $H/L = 0.125$ to 1	
Tou et al. ³	Channel flow	Experimental	$Re_L = 3000 - 84000$	
Tso et al. ⁴	Channel flow	Experimental	$Re_L = 600 - 8000$ $H/L = 0.5, 0.7, 1$	
Amon et al. ⁵	Oscillating flow (Communicating channels)	Experimental	$Re_H = 3/4 (U_e H/\vartheta) = 100 - 400$ $L/H = 2-6$ $L_1/H = 0.2$	
Valencia ⁶	Oscillating flow (Communicating channels)	Experimental/CFD	$Re_H = U_e H/\vartheta = 100 - 400$ $L_1/H = 0.5$	
Iachachene et al. ⁷	Self-oscillating impinging jet	CFD	$Re_d = U_e d/\vartheta = 4000 - 8000$	
Behera et al. ⁸	Pulsing impinging jet	CFD	$Re_d = 5000 - 8500$ $h/d = 5, 7, 9$	
Zhou et al. ⁹	Pulsing impinging jet	Experimental	$Re_d = 7500$ $h/d = 6$	
Xu et al. ¹⁰	Pulsing impinging jet	CFD	$Re_d = 3000 - 8000$ $h/d = 3, 5, 8$	
Park et al. ¹¹	Sweeping impinging jet	Experimental	$Re_d = 3600 - 15000$ Lower h/d ($h/d = 1 - 2$)	
Hossain et al. ¹²	Sweeping impinging jet	CFD	$Re_d = 10000 - 35000$ $h/d = 3 - 8$	
Hossain et al. ¹³	Sweeping impinging jet	Experimental	$h/d = 3 - 6$ $A/R = 0.5 - 1$ $S/d = 4, 6$ $\dot{m} = 0.1 - 4$ g/s	

*CFD: Computational study, H: Channel width, L: Heat source length, U: Channel average velocity, U_e : Nozzle average velocity, L_1/H : Blockage ratio, h/d : Stand-off distance ratio, A/R : Aspect ratio, P/d : Jet spacing ratio, \dot{m} : Mass flow rate

Xu et al.² conducted a numerical investigation of two-dimensional forced convection heat transfer between two walls, for the case in which discrete heat sources (electronic chips) were installed on one wall. The authors studied the effects of flow channel orientation and the ratio of the channel height to the heated block length on the heat transfer for two working fluids, water and Fluorinert™ Electronic Liquid (FC-72). Their results showed that the orientation of the channel did not have a significant effect on the cooling of the hot devices. Moreover, it was determined that water cooling performance was better than FC-72. Tou et al.³ investigated four hot blocks in a line for a single-phase heat transfer with FC-72 as a working fluid. The authors studied two configurations of protruding and flush-mounted blocks. The results indicated that heat transfer from the protruding blocks was greater than the flush-mounted blocks. Moreover, the heat transfer difference between the two configurations increased at higher Reynolds numbers. Tso et al.⁴ conducted an experimental study of forced convection heat transfer for four in-line hot blocks, which were located on a wall of a vertical rectangular channel. The results indicated that the effect of the channel height on the Nusselt number was weak, while the effect of Reynolds number on the Nusselt number was strong.

The use of an oscillating jet has attracted much attention for heat transfer enhancement. To compare heat transfer performance, Amon et al.⁵ carried out numerical and experimental investigations exploring the use of communicating channels as a mechanism to improve heat transfer. Rectangular bars were installed in a line at the center of the channel. It was concluded that use of the communicating channels with an interrupted surface increased the heat transfer compared with the plane channel. Communication between surfaces in the channel improved heat transfer by enhancing the mixing due to vortex generation in the transverse direction. In another study with similar geometry, Valencia⁶ numerically investigated the flow structure with mounted transverse vortex generators in the channel at a higher blockage ratio. The author showed that the heat transfer rate increased significantly due to the self-sustained oscillations. Iachachene et al.⁷ investigated the heat transfer in a cavity with a self-oscillating jet using the URANS $k-\omega$ model. It was determined that the cooling of walls of the cavity occurred simultaneously. The authors proposed a Nusselt number correlation based on nozzle-to-bottom wall distance and Reynolds number.

Furthermore, improving cooling performance using impinging jet heat transfer has been undertaken with pulsating oscillating jets. Behera et al.⁸ studied the effects of flow pulsation on heat transfer using the URANS $k-\epsilon$ model. It was concluded that the Nusselt number had a high value at a jet-to-plate spacing ratio of $h/d = 7$ compared to $h/d = 5$ and 9 . The heat transfer was enhanced for pulsating square and sine wave jets compared to the steady jet. They illustrated that the pulsed impinging jet increased the heat transfer in the wall jet region by 35% and 10% for square and sine wave jets, respectively. An experimental study was carried out by Zhou et al.⁹ to investigate the effects of unsteady jet impingement with sinusoidal and rectangular shape signal pulsations on smooth and non-smooth surfaces. With sinusoidal and rectangular pulsations, the average Nusselt number of the smooth surface increased up to 10% and 40%, respectively. Furthermore, sinusoidal pulsations decreased heat transfer of non-smooth surface, while rectangular pulsations increased the heat transfer of non-smooth surface significantly. Xu et al.¹⁰ conducted a two-dimensional numerical study of heat transfer under a pulsating turbulent slot impinging air jet using the Reynolds stress model (RSM). The intermittent pulsating jet showed a significant effect on the heat transfer rates. It was determined that the effects of intermittent pulsation were related to larger vortices, and higher entrainment and mixing, which were generated by flow instabilities.

Fluidic oscillators have also been used to generate sweeping jets for heat transfer enhancement in cooling systems. Park et al.¹¹ carried out an experiment to investigate the heat transfer of a sweeping air jet impinging on a flat wall at various Reynolds numbers (3600 - 15000) and low values of h/d ($= 1$ to 2). They observed two divided regions, and showed that the maximum Nu occurred at $Y/d < 1$, and the value of Nu decreased at $Y/d > 1$, where Y is the transverse distance from the impinging point. The results showed that heat transfer increased with increasing Reynolds number and decreasing h/d . At a farther distance from the center, the lateral velocity was reduced, which resulted in a decreasing heat transfer rate. Hossain et al.¹² investigated the effect of concave curvature on heat transfer by a sweeping air jet impingement using URANS SST $k-\omega$ at h/d in the range $3 - 8$ and Re_d in the range $10000 - 35000$. It was concluded that heat transfer augmentation increases with Reynolds number and decreases with jet-to-wall spacing for both sweeping and steady jet impingement. Furthermore, the results indicated that heat transfer deteriorated for highly curved surfaces, and heat transfer performance was enhanced for moderate curvature. In another study¹³, the authors carried out an experimental investigation of cylinder turbine blades cooling

using an array of sweeping jets for which $h/d = 3 - 6$, jet aspect ratio ($AR = 0.5 - 1$), jet spacing ($S/d = 4, 6$). It was concluded that the maximum sweeping jets cooling performance occurred at low h/d , high aspect ratio and low S/d .

The flow characteristics of self-oscillating jets have been investigated in our previous work¹⁴ and also reported in Chapter 3. The results showed that the oscillatory flow can potentially contribute to mixing and entrainment. The self-oscillating jet showed a complete mixing within a short distance from the nozzle, and a higher jet spread compared to non-oscillating jets. The main focus of this chapter is to extend our previous work¹⁴ to investigate the cooling performance of oscillating flow. While most of the previous studies were conducted on impinging jet cooling systems, this study is focused on self-oscillating jet cooling systems. To this end, the cooling performance of an unsteady self-oscillating jet, wall jet and channel flow with vertical and horizontal arrangements of heated blocks are compared in terms of temperature and Nusselt number.

5.3 Geometry and numerical procedure

The computational domain (i.e. confinement cavity) was discretized using a hexahedral mesh with 7 million cells for the self-oscillating and wall jets and 6 million cells for the channel flow. The cell sizes were determined to be adequate after performing a mesh dependency study for the channel flow and self-oscillating jet. For this mesh, the dimensionless distance of the first cell from the walls ($Y^+ = Yu_\tau/\nu$) is less than one, where ν is kinematic viscosity and u_τ is friction velocity defined as $u_\tau = (\tau_w/\rho)^{0.5}$, where τ_w is the wall shear stress. Moreover, the detailed analysis of the mesh dependency study has been investigated in our previous work¹⁴ on self-oscillating jets and it is not repeated here for brevity. An example of the channel flow mesh independence is presented in a forthcoming section. The governing Navier-Stokes equations were discretized by the finite volume method and solved using the commercial software STAR-CCM⁺¹⁵ with a second-order upwind scheme for convection terms and second-order time implicit scheme for time discretization. The time step was set at 0.01 ms, which ensured that the Courant number is less than one. The SIMPLE algorithm was used for pressure-velocity coupling. The Reynolds-Averaged Navier-Stokes equations for unsteady incompressible flow in the tensorial notation are¹⁶

$$\frac{\partial U_j}{\partial X_j} = 0 \quad (1)$$

$$\rho \left(\frac{\partial U_i}{\partial t} + U_j \frac{\partial U_i}{\partial X_j} \right) = -\frac{\partial P}{\partial X_i} + \frac{\partial}{\partial X_j} \left[\mu \frac{\partial U_i}{\partial X_j} - \rho \overline{u'_i u'_j} \right] \quad (2)$$

where U_i and u'_i are the mean and fluctuating velocity components, respectively, P is the pressure, ρ is the density, μ is the dynamic viscosity and the overbar denotes time-averaged values. Using the Boussinesq assumption, the components of the Reynolds stress tensor are given by

$$\overline{\rho u'_i u'_j} = \frac{2}{3} \rho k \delta_{ij} - \mu_t \left(\frac{\partial U_i}{\partial X_j} + \frac{\partial U_j}{\partial X_i} \right) \quad (3)$$

where k is the turbulent kinetic energy, μ_t is referred to as turbulent viscosity and δ_{ij} is the Kronecker delta. In this study, the unsteady Elliptic Blending Reynolds Stress Model (EBRSM)¹⁷, which consists of transport equations for each of the stress tensor components, was used to model turbulence. The energy conservation equation is expressed as

$$\rho \left(\frac{\partial T}{\partial t} + U_i \frac{\partial T}{\partial X_i} \right) = \frac{\partial}{\partial X_i} \left[\frac{\mu}{Pr} \frac{\partial T}{\partial X_i} - \rho \overline{u'_i \theta} \right] \quad (4)$$

where T is the temperature, θ is the temperature fluctuation and $Pr = \mu/\rho\alpha$ is the Prandtl number, where α is the thermal diffusivity. Based on the Boussinesq assumption, the temperature fluctuation is defined as

$$\overline{\rho u'_i \theta} = \sigma_t \frac{\partial T}{\partial X_i} \quad (5)$$

where σ_t is the turbulent Prandtl number, defined by the following equation:

$$\sigma_t = \frac{\mu_t}{\alpha_t} \quad (6)$$

Here, α_t is the turbulent thermal diffusivity.

For the investigation of cooling systems, hot blocks can be considered as electronic chips which are arranged in both vertical and horizontal arrangements as illustrated in Fig. 5.1.

In the case of the jets, a separate simulation was conducted for the turbulent flow in the square nozzle with hydraulic diameter $d = 14$ mm to produce fully developed flow conditions at the nozzle

exit. The inlet boundary conditions were applied inside the nozzle at 20 mm from the exit to ensure an accurate representation of the flow at the exit location. For the channel flow, the results of a separate simulation for fully developed flow was applied at the inlet. All walls of the confinement cavities had no-slip conditions and an outflow condition was applied at the outlet of the computational domain.

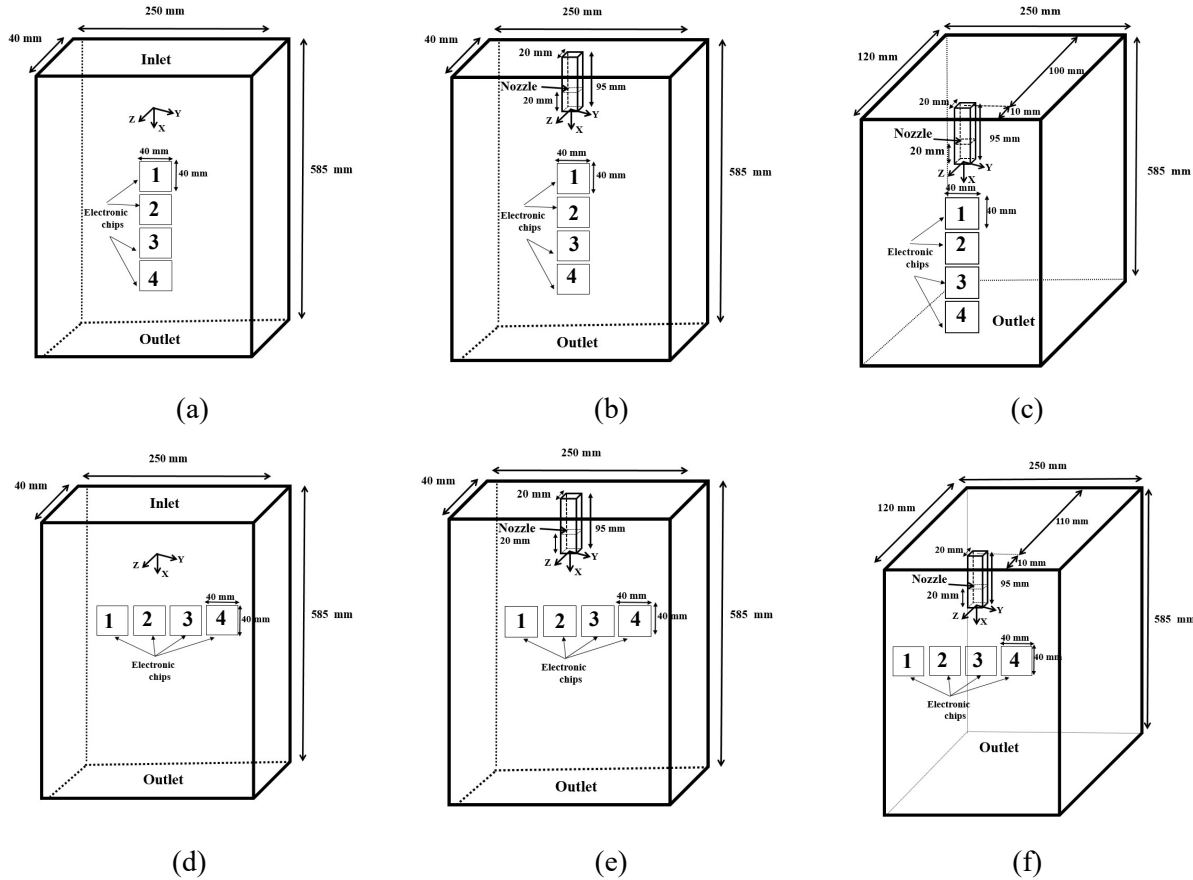


Fig. 5.1 Schematic of the cavity with hot blocks: (a, d) channel flow, (b, e) self-oscillating jet, (c, f) wall jet. Hot block arrangements: (a, b, c) vertical, (d, e, f) horizontal. (Not to scale)

For both arrangements, four in-line hot devices were located on the front surface of the cavity. Each device had a dimension of 40 mm x 40 mm. The distance between the heated blocks was 10 mm, and the hot block heat flux was 10^5 W/m^2 . Block number 1 was located at $X/d = 2.6$ and $X/d = 6.2$ for the vertical and horizontal arrangements, respectively. In the case of the jets, the coordinate system origin was located at the nozzle exit. However, the coordinate system for the channel flow was located 95 mm below the inlet (Fig. 5.1). The flow properties, as summarized in Table 5.2, were the same for both the vertical and horizontal arrangements. The fluid (water) was

assumed to be incompressible with a density of 997 kg/m^3 and dynamic viscosity of $9.7 \times 10^{-4} \text{ kg/(m.s)}$. All solid walls were assumed to be smooth.

Table 5.2. Flow parameters of channel flow, wall jet and self-oscillating jet

Channel flow			Wall jet			Self-oscillating jet		
Re_{dh}	U (m/s)	Inlet mass flow rate (kg/s)	Re_d	U (m/s)	Inlet mass flow rate (kg/s)	Re_d	U (m/s)	Inlet mass flow rate (kg/s)
5200	0.0735	0.7328	54000	3.75	0.7328	54000	3.75	0.7328

5.4 Validation

In this section, the two-dimensional forced convection heat transfer results for four in-line hot blocks with flush-mounted design in the channel flow are compared with the results of Xu et al.². The geometry is shown in Fig. 5.2, where the first discrete heat source was located at a distance of $3L$ from the channel entrance, and the channel exit was located at a distance of $5L$ from the last heat source, with $L = 12.7 \text{ mm}$. The inlet condition was a fully developed flow that was created in a separate simulation and the results were mapped to the main simulation inlet. The Reynolds numbers for water and FC-72 are 10^4 and 10^5 , respectively, with an inlet temperature of 30°C and heat flux of $q'' = 10^5 \text{ W/m}^2$.

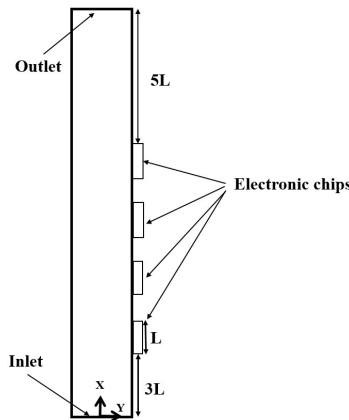


Fig. 5.2 Schematic of four in-line hot blocks (adapted from Xu et al.²) (Not to scale)

To investigate grid independency, 0.5, 1.0, 2.5 and 4.5 million cells were used to compare the predicted wall temperature distribution on the surface of the hot blocks. The results show that the temperature distribution did not change with increasing cell numbers, as illustrated in Fig. 5.3.

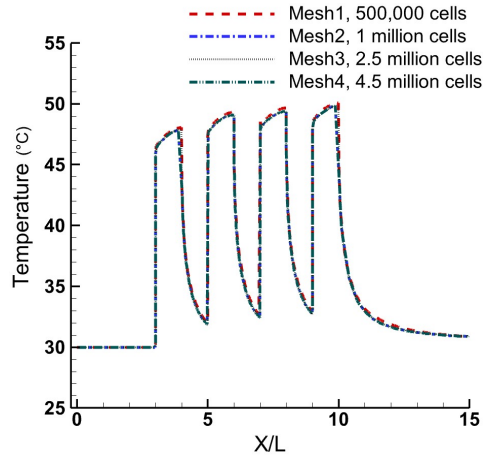


Fig. 5.3 Effect of grid size on the wall temperature distribution ($Re_L = 10^4$)

The temperature distribution on the wall with the hot blocks, for both water and FC-72, is shown in Fig. 5.4. The results show that the block number (i.e., their in-line position) does not have much effect on the wall temperature distribution, which is in good agreement with the results of Xu et al.²

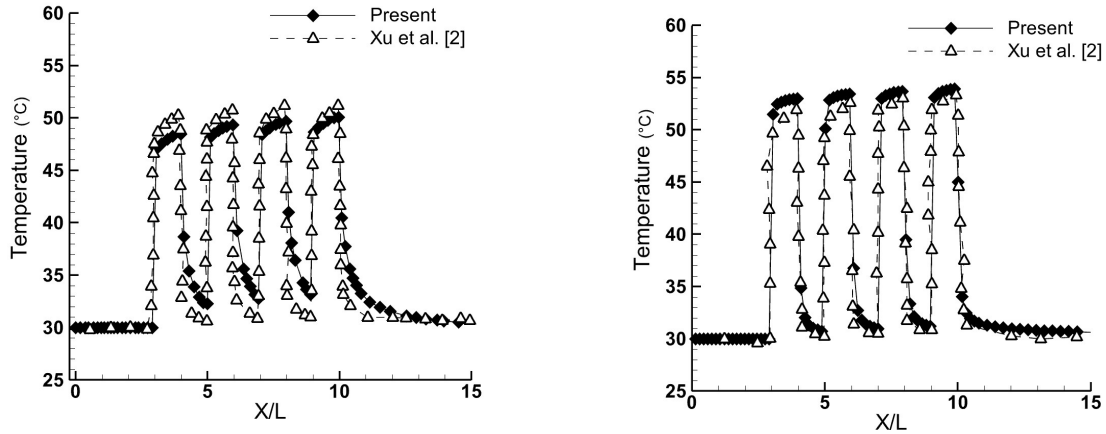


Fig. 5.4 Wall temperature distributions for four in-line heat sources: (a) water at $Re_L = 10^4$, b) FC-72 at $Re_L = 10^5$

As a means of further demonstrating validation, the numerical results using FC-72 as the coolant and the experimental results of Gersey and Mudawar¹⁸ are shown in Fig. 5.5. The wall temperature distributions for the four hot blocks over a range of Reynolds number of $10^4 - 10^5$ are shown in this figure. Gersey and Mudawar¹⁸ found that there was a single correlation for the heat transfer coefficient. The present results are in good agreement with that of Gersey and Mudawar¹⁸.

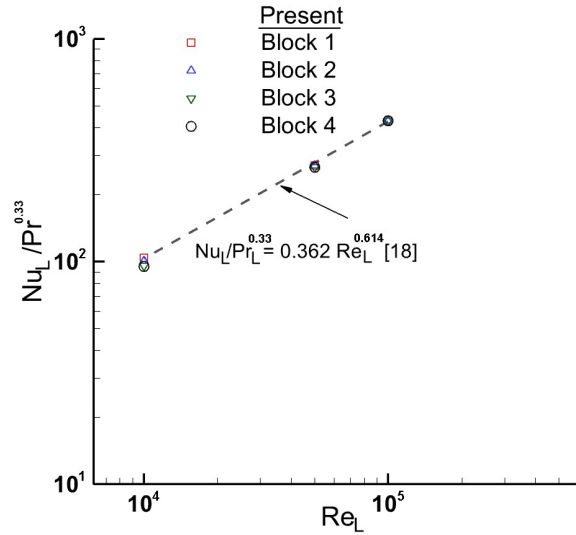


Fig. 5.5 Comparison of simulation and experimental heat transfer of the hot blocks

5.5 Results

In this section, the thermal features of flow in terms of temperature and Nusselt number are discussed. The results of the self-oscillating jet, the channel flow, and the wall jet simulations are compared for both vertical and horizontal arrangements of the heated elements. The time-averaged results are for 10 oscillation cycles after the oscillations have stabilized.

The comparison of the time-averaged temperature field of the four heated blocks are shown in Fig. 5.6 for the same mass flow rate of the fluid. The self-oscillating jet (Fig. 5.6(a)) provides a lower temperature on the hot blocks compared to the channel flow, albeit slightly higher than that in the case of the wall jet flow. It should be noted that the wall jet is 10 mm closer to the wall on which the blocks are located. Further, the wall jet is concentrated in the region of the heated blocks.

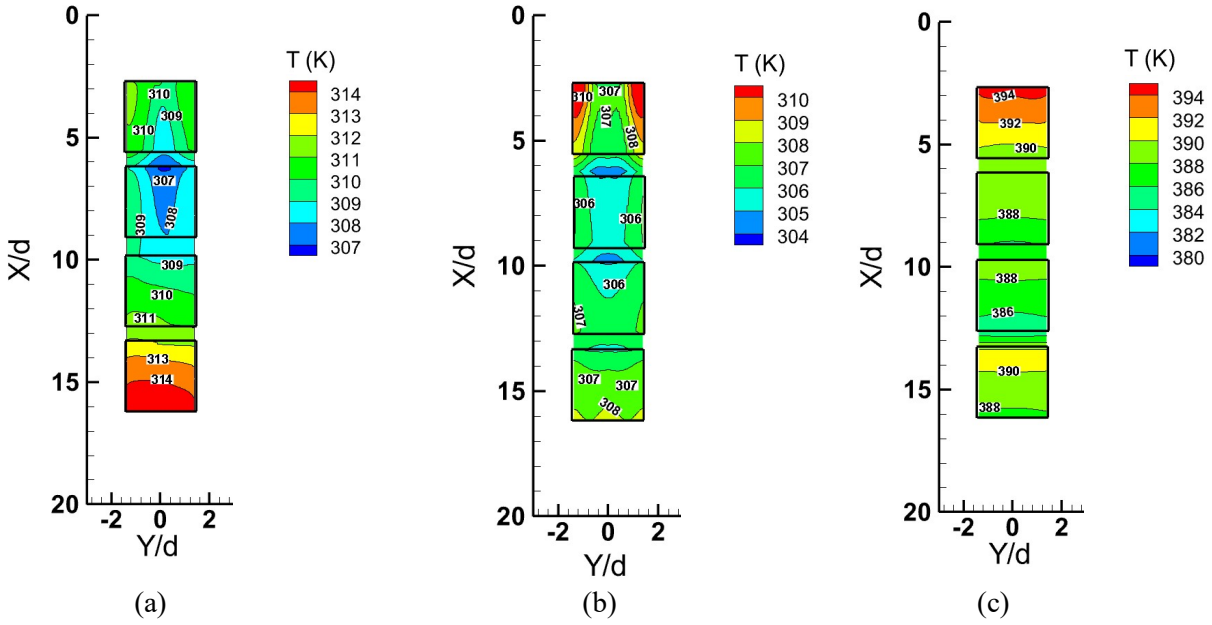
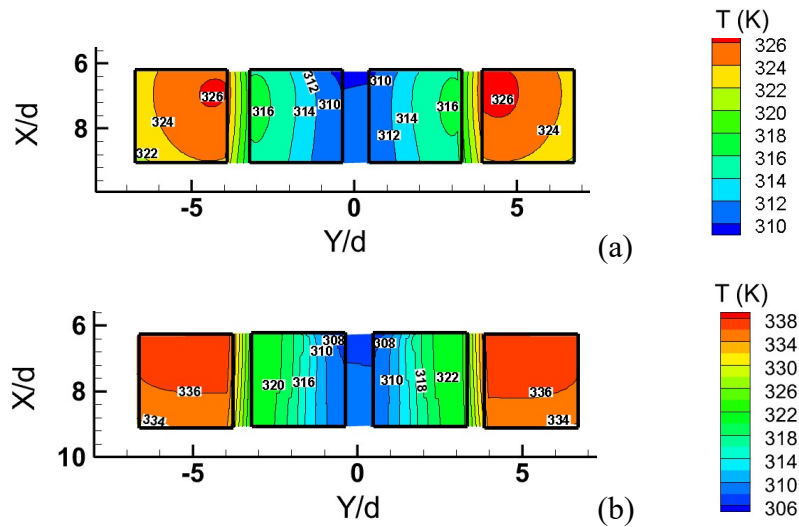


Fig. 5.6 Temperature distribution of hot blocks: (a) self-oscillating jet, (b) wall jet, (c) channel flow

The time-averaged temperature field of the four heated blocks in a horizontal configuration are shown in Fig. 5.7. From this figure it is clear that the self-oscillating jet provides for the least temperatures on all blocks and is marginally better than that seen in the wall jet flow even for the middle two blocks. Clearly, the performance of the self-oscillating jet is superior to that seen in the channel flow.



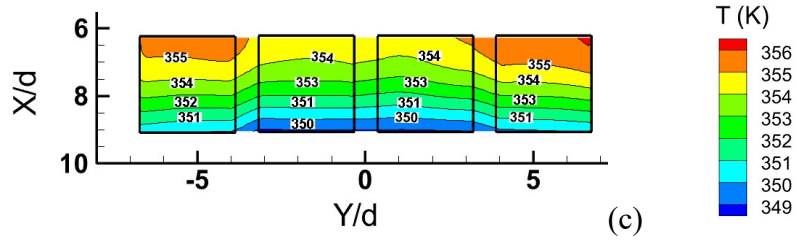


Fig. 5.7 Temperature field of hot blocks: (a) self-oscillating jet, (b) wall jet, (c) channel flow

The surface-averaged Nusselt number, which depends on the time, is calculated from

$$Nu_{av}(t) = (q''L)/[(T(t) - T_{inlet})K_f] \quad (7)$$

where $q'' = 10^5 \text{ W/m}^2$ is the heat flux, $L = 40 \text{ mm}$ is the length of each block, $T_{inlet} = 25^\circ\text{C}$ is the inlet temperature and K_f is the fluid thermal conductivity.

To examine the effect of jet location on the overall flow and heat transfer process, the instantaneous surface-averaged Nusselt number distribution on the hot blocks in a horizontal arrangement of heaters is shown in Fig. 5.8. This figure indicates that the surface-averaged Nusselt number of the wall jet and channel flow (Fig. 5.8(b,c)) does not change significantly over time while, for the self-oscillating jet, it varies at different locations. The instantaneous surface-averaged Nusselt number of the self-oscillating jet varies periodically with time. A maximum peak of Nu_{av} for the second hot block corresponds to a minimum value for the Nu_{av} for the third hot block and vice versa. Furthermore, the shape of the instantaneous signals are symmetrical due to the flapping motion of the jet.

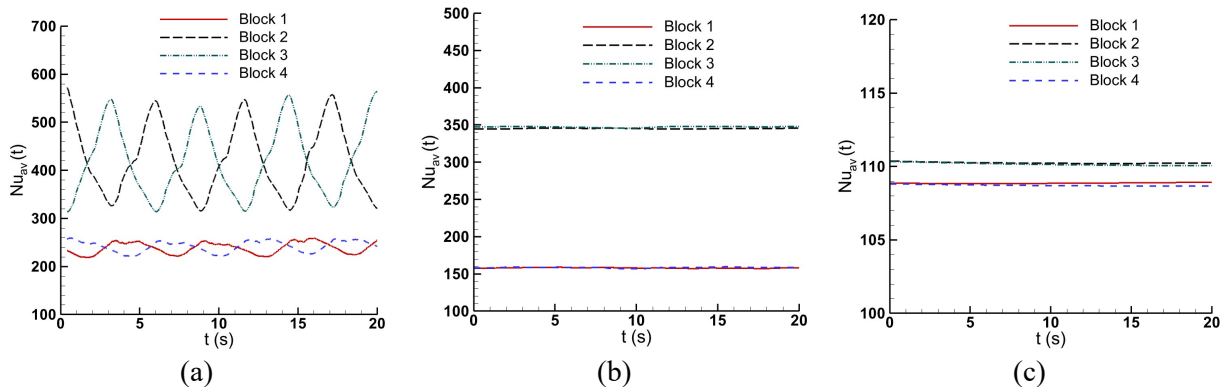


Fig. 5.8 The surface-averaged Nusselt number variation of hot blocks in horizontal arrangement of heaters: (a) self-oscillating jet, (b) wall jet, (c) channel flow

Figure 5.9 shows the double-averaged (i.e., space and time-averaged) Nusselt number (\overline{Nu}) for hot blocks. The channel flow shows a nearly constant Nusselt number for the horizontal and vertical arrangements. In the case of horizontal arrangement, the oscillating jet shows a higher Nusselt number, which illustrates the higher heat transfer due to the oscillation motion and mixing flow. However, in the case of vertical arrangement the wall jet shows a higher Nusselt number due to the higher momentum of flow. The above results clearly indicate the usefulness of self-oscillating jets for the cooling of hot blocks.

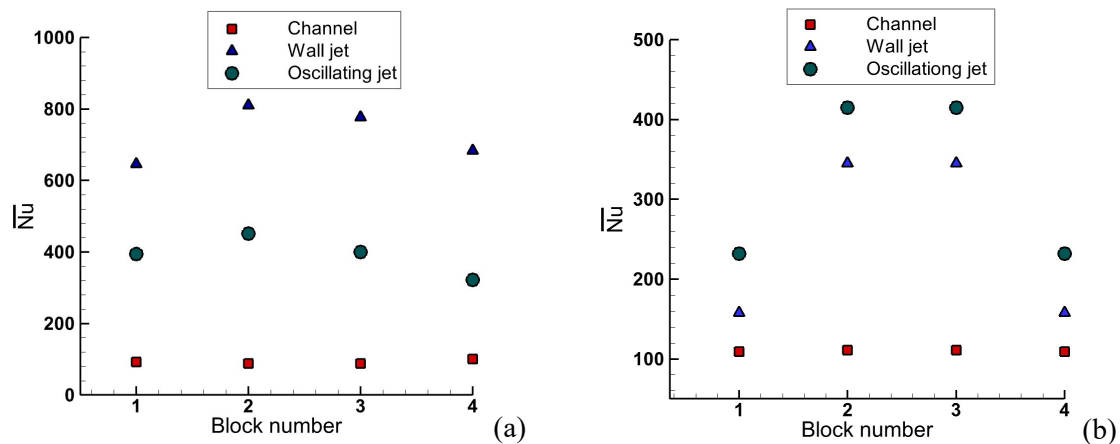


Fig. 5.9 Double-averaged Nusselt number of hot blocks: (a) vertical arrangement, (b) horizontal arrangement

5.6 Conclusions

In this chapter, an unsteady Reynolds stress turbulence model is used to investigate the cooling performance of self-oscillating jets at a Reynolds number of 54,000. The cooling performance of the self-oscillating jet is compared to the wall jet and channel flow in terms of Nusselt number for vertical and horizontal arrangements of hot devices (electronic chips). The results indicated that the channel flow has a lower Nusselt number due to the lower flow momentum. Furthermore, the wall jet showed a higher Nusselt number compared to the self-oscillating jet in the case where the initial jet axes are in-line with the arrangement of the blocks. For this arrangement, the wall jet is in closer proximity to the heated blocks than the self-oscillating jet. The self-oscillating jet increased heat transfer on a wider surface especially when the hot devices were located in a horizontal arrangement. Given the diverse nature of practical applications, detailed investigations need to be carried out for higher heat flux at the block surface and for other geometrical arrangements.

Nomenclature

d	Nozzle hydraulic diameter (m)
d_h	Channel hydraulic diameter (m)
h	Jet-to-wall spacing (m)
K_f	Fluid thermal conductivity (W/m.K)
L	Block length (m)
\dot{m}	Mass flow rate (g/s)
Nu_{av}	Surface-averaged Nusselt number
\overline{Nu}	Double-averaged Nusselt number
Pr	Prandtl number
q''	Heat flux (W/m ²)
Re_L	Reynolds number based on length of hot block ($= \rho UL/\mu$)
t	Time (s)
T	Temperature (K)
U	Streamwise mean velocity (m s ⁻¹)
U_e	Nozzle exit average velocity (m s ⁻¹)
u'	Velocity fluctuations (m s ⁻¹)
X, Y, Z	Cartesian coordinates
Y^+	Wall normal distance
α	Thermal diffusivity (m ² /s)
α_t	Turbulent thermal diffusivity (m ² /s)
δ_{ij}	Kronecker delta
ρ	Density (kg/m ³)
μ	Dynamic viscosity (kg/m.s)
μ_t	Turbulent viscosity (kg/m.s)
θ	Temperature fluctuation (K)
σ_t	Turbulent Prandtl number

References

1. J. Vimaldoss, R. Balachandar, R.M. Barron, N. Kar, M. Winter, G. Schilager and L.V. Iyer, "Impinging jet coldplate for power electronics with enhanced heat transfer," Patent, WO/2020/102371.

2. G.P. Xu, K.W. Tou and C.P. Tso, "Numerical modeling of turbulent heat transfer from discrete heat sources in a liquid-cooled channel," *Int. J. Heat Mass Transfer* 41, 1157-1166 (1998).
3. K.W. Tou, G.P. Xu and C.P. Tso, "Direct liquid cooling of electronic chips by single-phase forced convection of FC-72," *Exp. Heat Transfer* 11, 121-134 (1998).
4. C.P. Tso, G.P. Xu and K.W. Tou, "An experimental study on forced convection heat transfer from flush-mounted discrete heat sources," *J. Heat Transfer* 121, 326-332 (1999).
5. C.H. Amon, D. Majumdar, C.V. Herman, F. Myinger, B.B. Mikic and D.P. Sekulic, "Numerical, and experimental studies of self-sustained oscillatory flows in communicating channels," *Int. J. Heat Mass Transfer* 35, 3115–3129 (1992).
6. A. Valencia, "Heat transfer enhancement due to self-sustained oscillating transverse vortices in channels with periodically mounted rectangular bars," *Int. J. Heat Mass Transfer* 42, 2053–2062 (1999).
7. F. Iachachene, A. Mataoui and Y. Halouane, "Numerical investigations on heat transfer of self-sustained oscillation of a turbulent jet flow inside a cavity," *J. Heat Transfer* 137, 101702, 1-10 (2015).
8. R.C. Behera, P. Dutta and K. Srinivasan, "Numerical study of interrupted impinging jets for cooling of electronics," *IEEE Transactions on Components and Packaging Technologies* 30, 275-284 (2007).
9. J.W. Zhou, Y.G. Wang, G. Middelberg and H. Herwig, "Unsteady jet impingement: heat transfer on smooth and non-smooth surfaces," *Int. Commun. Heat Mass Transfer* 36, 103-110 (2009).
10. P. Xu, B. Yu, S. Qiu, H.J. Poh, and A.S. Mujumdar, "Turbulent impinging jet heat transfer enhancement due to intermittent pulsation," *Int. J. Therm. Sci.* 49, 1247–1252 (2010).
11. T. Park, K. Kara and K. Kim, "Flow structure and heat transfer of a sweeping jet impinging on a flat wall," *Int. J. Heat Mass Transfer* 124, 920–928 (2018).
12. M.A. Hossain, L. Agricola, A. Ameri, J.W. Gregory and J.P. Bons, "Effects of curvature on the performance of sweeping jet impingement heat transfer," 56th AIAA Aerospace Sciences Meeting, Florida (2018).

13. M.A. Hossain, L. Agricola, A. Ameri, J.W. Gregory and J. P. Bons, "Sweeping jet impingement heat transfer on a simulated turbine vane leading edge," Proceedings of GPPS Global Power and Propulsion Society, Montreal (2018).
14. M. Mosavati, R.M. Barron and R. Balachandar, "Characteristics of self-oscillating jets in a confined cavity," *Phys. Fluids* 32, 115103-1- 115103-17 (2020).
15. STAR-CCM+, User Guide, Version 13.06, Siemens, Munich, Germany (2018).
16. K. Hoffmann and S.T. Chiang, "Computational Fluid Dynamics," Vol. 3, 4th Edition, Engineering Education System, Wichita, Kansas, USA (2000).
17. B.E. Launder, G.J. Reece and W. Rodi, "Progress in the development of a Reynolds-stress turbulence closure," *J. Fluid Mech.* 68, 537–566 (1975).
18. C.O. Gersey and I. Mudawar, "Effects of orientation on critical heat flux from chip arrays during flow boiling," In *Advances in Electronic Packaging*, 1, 123-134 (1992).
19. AIAA, "Guide for the verification and validation of computational fluid dynamics simulations," AIAA Paper G-077-1998 (2002).
20. N.J. Lawson, "Self-sustained oscillation of a submerged jet in a thin rectangular cavity," *J. Fluids Struct.* 15, 59-81 (2001).
21. N. Bensider, A. Mataoui and M. Aksouh, "Control of self-sustained jet oscillations in a 3D thin rectangular cavity," *J. Chem. Eng. Res. Des.* 117, 533–541 (2017).

Chapter 6. Conclusions and recommendations

The overall objective of this study was to analyze the unsteady self-oscillatory jet flow in a cavity. The CFD simulations were conducted using the unsteady Reynolds-Averaged Navier-Stokes (URANS) equations with the Reynolds Stress Model (RSM) for turbulence. The study consisted of three sections:

- 1) Flow characteristics of single self-oscillating jet in a cavity using round and square nozzles
- 2) Twin self-oscillating jet characteristics
- 3) Cooling of hot devices using self-oscillating jets

6.1 Conclusions

A review of the literature revealed the lack of a comprehensive study on self-oscillatory jet flow field characteristics which can potentially contribute to the mixing and entrainment of fluid in a confined cavity. This study focused on the physics of the self-oscillatory jet to evaluate the flow characteristics which can be used for heat transfer enhancement. The effects of the oscillation on the behavior of flow properties were studied in terms of mean velocity, turbulence intensities and Reynolds shear stresses for both round and square self-oscillating confined jets and free jets. Identification of high turbulence intensity regions may be useful in applications to achieve higher heat transfer. Moreover, the unsteady Reynolds stress turbulence model was used to investigate the vortex ring deformation of confined oscillating round and square jets at a Reynolds number of 54,000. To this end, the vortex deformation in the jet was examined when the vortex ring impinges on the confinement walls. The results for the instantaneous vortex deformation showed that for the square jet, axis-switching occurred at approximately 0.7 diameters from the nozzle exit. Furthermore, it was shown that the deformed rings convert to two tornado-like vortices as they travel downstream. After creation of these tornado-like vortices, the vorticity direction changes from the confinement direction to the spanwise direction. A comparison of the oscillating round and square jets illustrated that nozzle geometry shape did not have a significant effect on the impingement point of the jet on the side walls, nor on the frequency of oscillation. The results demonstrated that the decay rate of the oscillating round jet was lower in the region $3 < X/d < 6$ and higher for $6 < X/d < 15$ compared to the square jet, where X is the streamwise distance from the nozzle exit and d is the nozzle hydraulic diameter. The streamwise turbulence intensity showed

two peaks in the near-field, which were converted to a single peak at $X/d \approx 7$. Moving downstream decreased the turbulence intensity and two peaks reappeared. The results showed that the oscillating square jet had a wider spread compared to the round jet. Furthermore, the self-oscillating jet had wider spread (40% higher) compared to the free jet, suggesting that the self-oscillating jet can be used to achieve more surface temperature uniformity in heat transfer applications.

The flow characteristics of twin self-oscillating jets were also studied. The majority of previous twin jet studies dealt with twin free jets, twin synthetic jets and twin sweeping jets. The present study investigated twin self-oscillating jets in a confined cavity when the jet oscillations are due to the Coanda effect. This study focused on the self-oscillatory flow field characteristics of twin jets for the region $1 < X/d < 15$, and the effects of nozzle spacing ($S/d = 2, 3, 4, 5$) on the frequency and other jet properties. URANS with RSM was used to investigate the flow of twin self-oscillating jets in a rectangular cavity for Reynolds number of 27,000. The effects of nozzle spacing on the jet mean velocity, turbulent characteristics and oscillation frequency were studied. The results showed that increasing the jet spacing did not significantly affect the frequency of the twin jets. However, after $S/d \approx 5$, the two jets did not merge, but oscillated between the sidewalls and center of the cavity, separately. When the nozzle spacing increases, the two jets are closer to the side walls and entrainment between the jets and sidewalls decreases. At higher nozzle spacing ($S/d \geq 5$), the two jets attach to the walls instead of merging and the two jets oscillate separately in opposite directions across half of the cavity width. The streamwise turbulence intensity of twin self-oscillating jets illustrated that at small S/d the turbulence intensity profiles showed four peaks in the vicinity of the shear layers. Moving downstream, the turbulence intensity at the center decayed and two mild peaks were observed. The turbulence intensity of twin jets was higher at the centerline of the cavity and around the centerline of each jet for $S/d < 5$ and for $S/d = 5$, respectively. Furthermore, the Reynolds shear stress profiles at $S/d = 5$ showed higher values compared to $S/d < 5$. These higher values are due to the lower entrainment of the inner shear layer when $S/d < 5$. The results showed that the spread and turbulence intensity over a wide region of twin self-oscillating jets are higher, resulting in the potential for a higher heat transfer.

Finally, the characteristics of self-oscillating jets have been investigated to assess their cooling performance. Horizontal and vertical arrangements of heated elements were considered. The

cooling performance in terms of Nusselt number were compared for self-oscillating jets, wall jets and channel flow. The results demonstrated that the channel flow had a lower Nusselt number for both vertical and horizontal arrangements of hot blocks. The wall jet produced a higher Nusselt number in a vertical arrangement compared to the oscillating jet due to the higher momentum and turbulence intensity of the wall jet. Furthermore, the self-oscillating jet increased heat transfer on a wider surface and is a viable option for the cooling of heated elements, especially when the electronic chips are located in a horizontal arrangement.

6.2 Recommendations

In this study, the URANS with RSM turbulence model was found to be accurate enough to capture the flow physics of the self-oscillatory jet flow. Although other turbulence models such as LES, DES and IDDES are expensive, these models can be used instead of the URANS models. In LES, DES and IDDES turbulent models, the influence of turbulence on the generation, transfer and breakdown of vortical structures can be captured with higher accuracy. These turbulent models should provide more information on vortex structures breakup in the oscillating flow, resulting in a better understanding of the flow characteristics. Furthermore, the λ_2 -criterion was used to capture the vortex dynamics. It could be informative to use other criteria to capture the vortex dynamics of the oscillatory jet flow.

From an applications perspective, the cooling of hot devices using twin self-oscillating jets could be investigated. The oscillating jets cover larger regions compared to free jets which potentially improves the cooling performance. Confined self-oscillating twin jet parameters such as nozzle size and location, nozzle spacing and flow rate can be optimized to yield maximum cooling efficiency.

Vita Auctoris

NAME: Maziar Mosavati

PLACE of BIRTH: IRAN

YEAR of BIRTH: 1984

EDUCATION:

Doctor of Philosophy

Mechanical Engineering

University of Windsor, Windsor, Ontario, Canada, 2020

Master of Applied Science

Mechanical Engineering

Islamic Azad University Science & Research Branch, Tehran, Iran, 2010

Bachelor of Engineering

Mechanical Engineering

Isfahan University of Technology, Isfahan, Iran, 2008